Neutron Scintillation Detectors Based on Polymers Containing Lithium-6 for Radiation Portal Monitor Applications

A Dissertation Presented for

the Doctor of Philosophy

Degree

The University of Tennessee, Knoxville

Andrew Neil Mabe

August 2013

Copyright © 2013 by Andrew Neil Mabe

All rights reserved.

Acknowledgements

I would like to acknowledge the others who have worked with me on this project Kyler Thomas, Daniel Henn, John Auxier II, Stephen Young, Matthew Urffer, Dr. Indraneel Sen, Dr. Mariya Zhuravleva, Dr. Rohit Uppal, Dr. Zheng Chang, Dr. Chuck Melcher, Dr. Dayakar Penumadu, and Dr. Larry Miller for their intellectual encouragement and positive attitudes throughout the course of my residency on this project. I believe that I could not have asked for a better group of scholars to work with and learn from. My fellow lab mates Jake Stewart, Brittany Miner, and Deborah Penchoff are appreciated for your camaraderie, as well as Dr. George Schweitzer for whom I am very grateful for his patience and guidance in helping me develop as a research scientist. A significant portion of this work has relied on computer-aided simulations. I would like to acknowledge specifically Matthew Urffer for running all the MCNPX and GEANT4 simulations, Stephen Young for all the microscopy data, John D. Auxier II for all the X-ray diffraction data, and Dr. Chuck Melcher for use of facilities used to characterize fluorescence responses presented in this work. Atlanta Microsystems, Inc., is acknowledged for conducting the elemental analysis described in this dissertation. I would also like to extend the utmost gratitude to my parents Heather Garrett and Britt Godwin and stepfather Jon Garrett without whom this contribution would not be possible and to my wife Rose and daughter Alina for your patience, constant encouragement, and unconditional love.

This material is based upon work supported, in part, by the National Science Foundation and the Domestic Nuclear Detection Office under Grants NSF ARI-0833492 and DNDO 003387891. Any opinions, findings, and conclusions or recommendations expressed in

this material are those of the author and do not necessarily reflect the views of the National Science Foundation or the U. S. Department of Homeland Security.

Abstract

The work presented herein describes an investigation of four main types of thin film polymer scintillators containing ^{6}Li [lithium-6] for neutron detection: polystyrene containing ^{6}LiF [lithium-6 fluoride] and a preblended fluor mixture comprising 2,5-diphenyloxazole and 1,4-bis(5-phenyloxazol-2-yl)benzene; poly(styrene-*co*-lithium maleate) containing salicylic acid; poly[styrene-*co*-lithium maleate-*co*-2-phenyl-5-(4-vinylphenyl)oxazole]; and poly(styrene-*co*-lithium 4-vinylbenzoate). A variety of chemical and physical characterizations as well as optical and scintillation characterizations were performed to guide the development of optimized compositions of each type of polymer film. The scintillation performances of optimized compositions of each type of polymer film were calibrated using GS20 lithium glass and evaluated against neutron detection and neutron/gamma-ray discrimination criteria established for radiation portal monitors.

Thin films were fabricated 2 inches in diameter over a variety of thicknesses using solution-casting methods. Investigation of polystyrene-based films by photoluminescence and scintillation indicated that the optimum concentration of fluor was 5.00%. Optimum neutron/gamma-ray discrimination was achieved for 50 micrometer thick films containing 10% ^{6}LiF [lithium-6 fluoride]. Two transparent lithium-containing polymers were successfully synthesized: poly(styrene-*co*-lithium maleate) containing salicylic acid and poly[styrene-*co*-lithium maleate-*co*-2-phenyl-5-(4-vinylphenyl)oxazole]. To the author's knowledge, the latter polymer represents the first polymer comprising the matrix, the thermal neutron capture nuclide ^{6}Li [lithium-6], and the fluor that has been synthesized for the purpose of thermal neutron detection. The polymer poly(styrene-*co*-lithium 4-vinylbenzoate) could not be solvated and decomposed below its melting temperature and was thus considered not useful for this

application. The polystyrene-based materials had the greatest light yields whereas the poly[styrene-*co*-lithium maleate-*co*-2-phenyl-5-(4-vinylphenyl)oxazole] material had the best neutron/gamma-ray discrimination properties. All three classes of materials can be used to satisfy the detection criteria in the current radiation portal monitor footprint by implementing a multilayer format.

Preface

It has been shown by Bethe and others that beryllium when bombarded by α-particles of polonium emits a radiation of great penetrating power, which has an absorption coefficient in lead of about 0.3 (cm.)$^{-1}$. Recently, Mme. Curie-Joliot and M. Joliot found, when measuring the ionisation produced by this beryllium radiation in a vessel with a thin window, that the ionisation increased when matter containing hydrogen was placed in front of the window. The effect appeared to be due to the ejection of protons with velocities up to a maximum of nearly 3 × 10^{9} cm. per sec. They suggested that the transference of energy to the proton was by a process similar to the Compton effect, and estimated that the beryllium radiation had a quantum energy of 50 × 10^{6} electron volts.

I have made some experiments using the valve counter to examine the properties of the radiation excited in beryllium. The valve counter consists of a small ionisation chamber connected to an amplifier and the sudden production of ions by the entry of a particle, such as a proton or an α-particle, is recorded by the deflexion of an oscillograph. These experiment have shown that radiation ejects particles from hydrogen, helium, lithium, beryllium, carbon, air, and argon. The particles ejected from hydrogen behave, as regards range and ionising power, like protons with speeds up to about 3.2 × 10^{9} cm. per sec. The particles from the other elements have a large ionizing power, and appear to be in each case recoil atoms of the elements.

If we ascribe the ejection of the proton to a Compton recoil from a quantum of 52 × 10^{6} electron volts, then the nitrogen recoil atom arising by a similar process should have an energy not greater than about 400,000 volts, should produce not more than about 10,000 ions and have a range in air at N.T.P. of about 1-3 mm. Actually, some of the recoil atoms in nitrogen produce

at least 30,000 ions. In collaboration, with Dr. Feather, I have observed the recoil atoms in an expansion chamber, and their range, estimated visually, was sometimes as much as 3 mm. at N.T.P.

These results, and others, I have obtained in the course of the work, are very difficult to explain on the assumption that the radiation from beryllium is a quantum radiation, if energy and momentum are to be conserved in the collisions. The difficulties disappear, however, if it be assumed that the radiation consists of particles of mass 1 and charge 0, or neutrons. The capture of the α-particle by the ^{9}Be nucleus may be supposed to results in the formation of a ^{12}C nucleus and the emission of the neutron. From the energy relations of the process the velocity of the neutron emitted in the forward direction may well be about 3×10^{9} cm. per sec. The collisions of the neutron with the atoms through which it passes give rise to the recoil atoms, and the observed energies of the recoil atoms are in fair agreement with this view. Moreover, I have observed that protons ejected from hydrogen by the radiation emitted in the opposite direction to that of the exciting α-particle appear to have a smaller range than those ejected by the forward radiation. This is a simple explanation on the neutron hypothesis.

If it be supposed that the radiation consists of quanta, then the capture of the α-particle by the ^{9}Be nucleus will form a ^{13}C nucleus. The mass defect of ^{13}C is known with sufficient accuracy to show that the energy of the quantum emitted in this process cannot be greater than about 14×10^{6} volts. It is difficult to make such a quantum responsible for the effects observed.

It is to be expected that many of the effects of a neutron in passing through matter should resemble those of a quantum of high energy, and it is not easy to reach the final decision

between the two hypotheses. Up to the present, all the evidence is in favour of the neutron if the conservation of energy and momentum be relinquished at some point.

J. Chadwick

Cavendish Laboratory,

Cambridge, Feb. 17, 1932 [1]

Table of Contents

CHAPTER 1: INTRODUCTION 1

CHAPTER 2: RADIATION INTERACTIONS WITH MATTER 7

2.1. Heavy Charged Particles 8

2.2. Beta Particles 10

2.3. Gamma-Rays 11

2.4. Neutrons 14

CHAPTER 3: CURRENT MATERIALS FOR THERMAL NEUTRON DETECTION 17

3.1. Thermal Neutron Detection 17

3.2. Current Neutron Detection Materials 19

3.3. Scintillators 21

3.3.1. Introduction 21

3.3.2. Inorganic Scintillators 23

3.3.3. Organic Scintillators 23

3.4. Polymer Scintillators 25

3.4.1. General Remarks 25

3.4.2. Photophysics of Organic Compounds 25

3.4.3. Generation of Excited States by Radiation 31

3.4.4. Polymer Scintillators as Thermal Neutron Detectors 37

CHAPTER 4: EXPERIMENTAL DESIGN AND INSTRUMENTAL METHODS 40

4.1. Analysis and Purification of ^{6}LiOH 40

4.2. Synthesis of Lithium Salts 41

4.3. Composite Approach 42
4.4. Homogeneous Approach 46
4.4.1. Poly(styrene-*co*-lithium maleate) 47
4.4.2. Poly[styrene-*co*-lithium maleate-*co*-2-phenyl-5-(4-vinylphenyl)oxazole] 50
4.4.3. Poly(styrene-*co*-lithium 4-vinylbenzoate) 57
4.5. Characterization Methods 59
4.5.1. Particle Distribution and Morphology 59
4.5.2. Optical Properties 59
4.5.3. Electronics Used in Scintillation Characterizations 60
4.5.4. Calculation of Light Yields 60
4.5.5. Radiation Sources 63
4.5.6. Neutron Irradiator 64
4.5.7. Gamma-Ray Irradiator 69
4.5.8. Quantification of Radiation Exposure to Detectors 72
4.5.9. Calculation of the Ranges of Heavy Ions 73
4.5.10. Detection Efficiency Calculations 75
CHAPTER 5: RESULTS AND DISCUSSION 79
5.1. Analysis and Purification of ^{6}LiOH 79
5.2. Justification of Experimental Design 80
5.2.1. Comparison of Lithium Salts 80
5.2.2. Repeatability of Fabrication and Scintillation Measurement Protocols 80
5.3. Polystyrene-Based Detectors 84
5.3.1. Effects of ^{6}LiF on Optical Clarity 84

5.3.2. Fluorescence 87
5.3.3. Scintillation 96
5.4. Poly(styrene-*co*-lithium maleate) 111
5.4.1. Motivation 111
5.4.2. Synthesis and Chemical Characterizations 112
5.4.3. Optical Transmission and Fluorescence 123
5.4.4. Scintillation 129
5.5. Poly[styrene-*co*-lithium maleate-*co*-2-phenyl-5-(4-vinylphenyl)oxazole] 132
5.5.1. Synthesis and Chemical Characterizations 132
5.5.2. Fluorescence 141
5.5.3. Scintillation 144
5.7. Poly(styrene-*co*-lithium 4-vinylbenzoate) 148
5.7.1. Synthesis and Chemical Characterizations 148
CHAPTER 6: CONCLUSIONS AND FUTURE WORK 150
6.1. Summary and Important Conclusions 150
6.2. Recommendations for Future Work 153
LIST OF REFERENCES 156
VITA 166

List of Tables

Table 1. Detection Criteria for Radiation Portal Monitor Neutron Detectors 4

Table 2. Thermal Neutron Capture Nuclides 16

Table 3. Detection Systems Evaluated at PNNL 20

Table 4. List of Representative Thermal Neutron Detection Systems 21

Table 5. Properties of Selected Lithium-6 Salts. 43

Table 6. Radiation Sources Used for Scintillation Characterizations 64

Table 7. Fraction of Emitted Neutrons that are Incident on a Detector 74

Table 8. Fraction of Emitted Gamma-Rays that are Incident on a Detector 74

Table 9. Repeatability of Neutron Count Rate Measurements 83

Table 10. Effects of Substrate on Scintillation Responses 83

Table 11. ^{241}Am Alpha Spectral Features of 15 - 150 μm PS-Based Films 98

Table 12. Ranges of Heavy Ions in PS and ^{6}LiF 99

Table 13. Light Yields of PS-Based Films for Gamma-Rays and Neutrons 100

Table 14. Neutron Count Rates Above Gamma-Ray MLLD for PS Films 104

Table 15. Average Fraction of Energy Deposited in PS-Based Films of Various Thicknesses . 104

Table 16. Scaling up PS Films to Simultaneously Satisfy DHS $\varepsilon_{int\,\gamma}$ and $\varepsilon_{abs\,n}$ Criteria 110

Table 17. Light Yields and Neutron/Gamma-Ray Discrimination of PS and PS-*co*-PLiMAn Films 134

Table 18. Elemental Analysis of PS-*co*-PMAn-*co*-PVPPO 136

Table 19. Possible Compositions of PS-*co*-PMAn-*co*-PVPPO 137

Table 20. Composition of PS-*co*-PMAn-*co*-PVPPO 141

Table 21. Light Yields and Neutron/Gamma-Ray Discrimination of Films Based on PS, PS-*co*-PLiMAn, and PS-*co*-PLiMAn-*co*-PVPPO..... 147

List of Figures

Figure 1. Gamma-Ray Interactions as Functions of Gamma-Ray Energy. 12

Figure 2. Schematic Illustrating the Different Methods by which Thermal Neutrons Can Be Detected. 18

Figure 3. Jablonski Diagram Illustrating Mechanisms by which Electronic Excitations Can Relax. 28

Figure 4. Synthesis of PS-*co*-PMAn and PS-*co*-PLiMAn. 48

Figure 5. Synthesis of VPPO. 51

Figure 6. Synthesis of PS-*co*-PMAn-*co*-PVPPO and PS-*co*-PLiMAn-*co*-PVPPO. 53

Figure 7. Synthesis of Li4VB and PS-*co*-PLi4VB. 58

Figure 8. Schematic of Instrumentation Used to Measure Scintillation Responses. 61

Figure 9. Illustration of the Neutron Irradiator. 65

Figure 10. MCNPX Simulation of the Neutron Fluence in the Neutron Irradiator. 67

Figure 11. Neutron Fluences Through the Lead and Cadmium Tubes and the Resulting Subtracted Spectrum (Pb – Cd)..... 68

Figure 12. Attenuation of Gamma-Rays Through 1.6 mm Thick Sheets of Lead and Cadmium as a Function of Gamma-Ray Energy. 70

Figure 13. Images of the Gamma-Ray Irradiator. 71

Figure 14. Simulated Geometry of PS Containing 10% ^{6}LiF Using the TRIM Code. 76

Figure 15. Powder X-Ray Diffraction Patterns of LiOH, LiOH · H_2O, and Li_2CO_3..... 81

Figure 16. Representative Images of PS Composite Films Containing ^{6}LiF and PPO/POPOP… 85

Figure 17. Bright-Field CLSM Image of ^{6}LiF Particles Distributed in a PS Matrix. 86

Figure 18. Normalized Fluorescence Spectra of PS and of PS Containing PPO/POPOP. 89

Figure 19. Fluorescence Emission Spectra of PS Films Containing Various Concentrations of PPO/POPOP..... 91

Figure 20. PS and POPOP Emission for 150 μm PS Samples as a Function of Wt% PPO/POPOP. 92

Figure 21. Emission Spectra of 150 μm Thick PS Films Containing 10% PPO/POPOP at Various Loadings of ^{6}LiF. 95

Figure 22. Alpha Responses for PS Samples Containing 10% ^{6}LiF and 5% PPO/POPOP over the Thickness Range 15 – 150 μm. 97

Figure 23. Gamma-Ray Intrinsic Efficiency as a Function of MLLD for Film Thicknesses over the Range 15 – 601 μm. 101

Figure 24. Gamma-Ray Intrinsic Efficiency and Thermal Neutron Count Rate Spectrum for a PS Film 50 μm Thick Containing 10% ^{6}LiF and 5% PPO/POPOP. 102

Figure 25. Fraction of Energy Deposited in PS-Based Films by Thermal Neutron Capture and Compton-Scattered Electrons from Gamma-Rays..... 105

Figure 26. P-XRD Pattern of Transparent PS-*co*-PLiMAn (82.5% Lithiation). 119

Figure 27. P-XRD Pattern of Cloudy PS-*co*-PLiMAn (90% Lithiation). 120

Figure 28. Thermogravimetric Analysis of PS-*co*-PLiMAn Containing 11.6% HSal. 122

Figure 29. Transparent PS-*co*-PLiMAn Film Containing 11.6% HSal by Mass. 124

Figure 30. Transmission Spectrum of a PS-*co*-PLiMAn Film Containing 11.6% HSal. 125

Figure 31. Photoluminescence Spectra of PS and PS-*co*-PLiMAn Containing 11.6 wt% HSal. 126

Figure 32. Integrated Fluorescence Emission Intensity as a Function of Wt% HSal. 128

Figure 33. ^{241}Am Alpha Response for PS-*co*-PLiMAn Containing 11.6 Wt% HSal. 130

Figure 34. ^{36}Cl Beta Response for PS-*co*-PLiMAn Containing 11.6 wt% HSal. 131

Figure 35. ^{252}Cf Thermal Neutron Count Rate Spectrum and Gamma-Ray Intrinsic Efficiency versus MLLD for PS-*co*-PLiMAn Containing 11.6 Wt% HSal. 133

Figure 36. Thermogravimetric Analysis of PS-*co*-PLiMAn-*co*-PVPPO..... 138

Figure 37. Thermogravimetric Analysis of PS-*co*-PLiMAn-*co*-PVPPO Expanded over the Temperature Range 35 – 290°C..... 140

Figure 38. Image of PS-*co*-PLiMAn-*co*-PVPPO Film Mounted on an Acrylic Disk. 142

Figure 39. Percent Transmission Spectrum of PS-*co*-PLiMAn-*co*-PVPPO Mounted on an Acrylic Disk. 143

Figure 40. Photoluminescence Spectra of PS and PS-*co*-PLiMAn-*co*-PVPPO. 145

Figure 41. Gamma-Ray Intrinsic Efficiency and Thermal Neutron Count Rate versus MLLD of PS-*co*-PLiMAn-*co*-PVPPO..... 146

List of Abbreviations and Symbols

SNM	Special Nuclear Material
NNSA	National Nuclear Security Administration
DHS	Department of Homeland Security
DNDO	Domestic Nuclear Detection Office
NSF	National Science Foundation
γ	Gamma-Ray
HDPE	High Density Polyethylene
eV	Electron Volt
RPM	Radiation Portal Monitor
SAIC	Science Applications International Corporation
$\varepsilon_{abs\ n}$	Absolute Neutron Detection Efficiency
$\varepsilon_{int\ \gamma,n}$	Intrinsic Gamma-Neutron Detection Efficiency
GARRn	Gamma Absolute Rejection Ratio for Neutrons
cps	Counts Per Second
ng	Nanogram
mR	Milli-Roentgen
hr	Hour
β^-	Negative Beta Particle
S_c	Collisional Stopping Power
dT	Incremental Change in Energy
dx	Incremental Path Length

r_0	Electron Radius
m_e	Electron Rest Mass
c	Speed of light in vacuum
q	Instantaneous Charge on a Heavy Ion
N_A	Avogadro's Number
ρ	Mass Density
Z	Atomic Number
M_m	Molar Mass of Target Material
T	Kinetic Energy
M	Mass of Heavy Charged Particle
IP	Average Ionization Potential of Target Material
υ'	Antineutrino
τ	Photoelectric Effect Probability for Gamma-Rays
σ	Compton Scattering Probability for Gamma-Rays
κ	Pair Production Probability for Gamma-Rays
hυ	Photon Energy
θ	Photon Scattering Angle
T_C	Compton Electron Energy
min	Minute
n	Neutron
K	Kelvin
b	Barn (10^{-24} cm^2)
p^+	Proton

α	Alpha Particle
s	Second
PMT	Photomultiplier Tube
PNNL	Pacific Northwest National Laboratory
λ	Wavelength
LY	Light yield
ph	Photon
ph/MeV	Photons per Megaelectron Volt of Energy Deposited
LiSal	Lithium Salicylate
FWHM	Full Width at Half Max
PS	Polystyrene
PVT	Poly(vinyl toluene)
UV	Ultraviolet
ϵ	Molar Extinction Coefficient
l	Path Length
[M]	Concentration of Species M
ISC	Intersystem Crossing
S_i	Singlet State i
T_i	Triplet State i
ϕ_i	Quantum Yield of Process i
k_i	Rate Constant of Process i
R_{mn}	Probability of Transition Between Two Electronic States m and n
φ_i	Wavefunction of Orbital i

$\hat{R}$	Transition Dipole Operator
ζ	Nuclear Wavefunction
I_i	Spin of Electron in Orbital i
A_{mn}	Absorption Intensity from State m to State n
FRET	Förster Resonance Energy Transfer
E	Efficiency of FRET
FR_{DA}	Distance between Donor and Acceptor
FR_0	Förster Distance
ϕ_D	Quantum Yield of Donor Fluorescence
Λ	Orientation Factor
RI	Refractive Index
$\bar{\upsilon}$	Frequency
$\sigma^{D}_{fluor}(\bar{\upsilon})$	Donor Fluorescence Spectrum as a Function of Frequency
$\varepsilon_A(\bar{\upsilon})$	Acceptor Absorbance Spectrum as a Function of Frequency
PMMA	Poly(methyl methacrylate)
PPO	2,5-Diphenyloxazole
PTP	*p*-Terphenyl
POPOP	1,4-Bis(5-phenyloxazol-2-yl)benzene
TPB	1,1',4,4'-Tetraphenylbutadiene
9MA	9-Methylanthracene
TMPI	1,1,3-Trimethyl-3-phenylindan
P2VN	Poly(2-vinyl naphthalene)
PEN	Poly(ethylene naphthalate)

Q	Reaction Energy
LC/MS	Liquid Chromatography/Mass Spectrometry
p-XRD	Powder X-ray Diffraction
ICP-OES	Inductively Coupled Plasma–Optical Emission Spectroscopy
AIBN	2,2'-Azobisisobutyronitrile
MMA	Methyl Methacrylate
THF	Tetrahydrofuran
BHT	Butylated Hydroxytoluene
^{1}H NMR	Proton Nuclear Magnetic Resonance
UVT	Ultraviolet Transmission
MAn	Maleic Anhydride
PS-*co*-PMAn	Poly(styrene-*co*-maleic anhydride)
HSal	Salicylic Acid
PS-co-PLiMAn	Poly(styrene-*co*-lithium maleate)
VPPO	2-Phenyl-5-(4-vinylphenyl)oxazole
PS-*co*-PMAn-*co*-PVPPO	Poly[styrene-*co*-maleic anhydride-*co*-2-phenyl-5-(4-vinylphenyl)oxazole]
PS-*co*-PLiMAn-*co*-PVPPO	Poly[styrene-*co*-lithium maleate-*co*-2-phenyl-5-(4-vinylphenyl)oxazole]
DMF	N,N-Dimethylformamide
PS-*co*-PLi4VB	Poly(styrene-*co*-lithium 4-vinylbenzoate)
4VBA	4-Vinylbenzoic acid
Li4VB	Lithium 4-vinylbenzoate

χ_i	Mole Fraction of Component i
CLSM	Confocal Laser Microscopy
V	Volt
MCB	Multichannel Buffer
ADC	Analog-to-Digital Converter
LLD	Lower Level Discriminator
<x>	Spectral Average
x	Channel
f(x)	Count Rate Spectrum
Ci	Curie
MCNPX	Monte Carlo for Neutrons and Photons Transport Code
I	Photon Intensity
μ	Attenuation Coefficient
t	Thickness
N_c	Number of Counts Recorded by a Detector
N_i	Number of Particles Incident on a Detector
Ω	Fraction of Emitted Particles that are Incident on a Detector
A	Source Activity
TRIM	Transport of Ions in Matter Code
ICRU	International Committee on Radiation Units
CR	Count Rate
MLLD	Mathematical Lower Level Discriminator
$\gamma(x)$	Gamma-Ray Count Rate Spectrum

$CR_{n>MLLD}$	Neutron Count Rate above MLLD
$\varepsilon_{int,n>MLLD}$	Neutron Intrinsic Efficiency above MLLD
$\varepsilon_{abs,n>MLLD}$	Absolute Neutron Efficiency above MLLD
A_n	Source Neutron Emission Rate
GEANT	Geometry and Tracking Code
THF-d_4	Deuterated Tetrahydrofuran
DMSO-d_6	Deuterated Dimethylsulfoxide

Chapter 1: Introduction

The development of effective thermal neutron detectors is relevant to the fields of nuclear physics, nuclear power generation, neutron imaging, well logging, and homeland security. Currently, ^{3}He is implemented in international portal monitors to detect illicit smuggling of special nuclear materials (SNM) into the United States as well as in medical diagnostics and in basic scientific research.[2] The primary production of ^{3}He occurs at the National Nuclear Security Administration's (NNSA) Savannah River Site in South Carolina from the decay of tritium used in nuclear weapons.[3] Since the infraction on national security on September 11, 2001, there has been an increase in the deployment of radiation portal monitors containing ^{3}He. The expanded demand has reduced the stockpile of ^{3}He, creating a shortage of the material. In response to this shortage, the Department of Homeland Security (DHS), the Domestic Nuclear Detection Office (DNDO), and the National Science Foundation (NSF) have organized and funded scientific research programs to develop replacement technologies to be implemented for national security purposes.

Fuel rods used in nuclear reactors typically contain the fissionable nuclei ^{235}U or ^{238}Pu, which can also be used as fuel for a nuclear weapon. After a period of time in a reactor, these rods become "spent," indicating that the fraction of ^{235}U or ^{238}Pu has decreased below optimal operation concentrations. Even so, these fuel rods still contain several percent of ^{235}U or ^{238}Pu, along with their highly radioactive daughter nuclei. These "spent" rods are placed in storage for a period of time, during which it is possible for people with maligned intentions to take possession of the fissionable materials. Since the time that isotopic enrichment strategies of these isotopes were elucidated, there has not been an adequate amount of fissionable materials lost from the various storage sites to construct a nuclear weapon.[4] However, it is possible that smaller quantities of these radioactive materials can be placed in proximity with a regular explosive device and detonated, spreading radioactive materials over a large area and into the air. It is thus of interest to national security that any special nuclear or radiological materials smuggled into the United States be detected and interdicted.

Approximately 64,000 containers and 1.1 million people are screened by DHS at international borders every day.[5] Radiation detectors deployed for national security purposes must have a very low incidence of false alarms which means that the detector must be able to unambiguously detect the presence of SNM. Many radioactive nuclides such as ^{235}U and ^{238}Pu have highly characteristic gamma-ray (γ) emission signatures that can be used to identify them almost unambiguously in controlled laboratory conditions with proper equipment. However, it is likely that one seeking to tacitly move SNM would use common materials such as steel or lead to shield the gamma-ray emissions. The resulting energy spectrum of the gamma-rays exiting the shielding materials would be distorted from the original signature spectrum and no longer useful for unambiguous identification. Also, due to the presence of nonthreatening gamma-ray sources

such as spurious changes in background radiation, radioactive components in building materials, and radiopharmaceuticals, a detector designed to detect gamma-rays for the purpose of nuclear nonproliferation would be subject to false alarms on a frequent basis.

In addition to gamma-rays, fissionable materials also spontaneously fission and produce characteristic neutron emission spectra. These neutrons can be shielded and the resulting energy spectrum distorted; however, it is very difficult to shield all the neutrons. High density polyethylene (HDPE) is a common shielding material for neutrons due to its high density of hydrogen atoms which are effective momentum absorbers for neutrons. Large thicknesses of HDPE can effectively reduce the energy of neutrons to energies corresponding to ambient temperatures, or approximately 0.025 eV. Neutrons in this energy region are commonly called thermal neutrons and interact primarily by absorption by a suitable nuclide. A thermal neutron absorber such as boron carbide can be placed around the HDPE to reduce the fluence of neutrons; however, it will not prevent all neutrons from exiting the shielding materials. Free neutrons have a characteristic half-life of 10.6 minutes,[6] so the vast majority of free neutrons that are generated by cosmic events decay before reaching Earth and are thus not commonly present in background radiation. Neutrons are also not commonly emitted by either construction materials or radiopharmaceuticals. Thus, the determination of the presence of neutrons is the best method by which the presence of shielded SNM can be detected.

The quantitative detection requirements that have been established for detectors that are to be implemented in radiation portal monitors (RPMs) are listed in Table 1 in the RPM8 SAIC (Science Applications International Corporation) footprint.[7,8] Absolute neutron detection efficiency ($\varepsilon_{abs\ n}$), intrinsic gamma-neutron detection efficiency ($\varepsilon_{int\ \gamma,n}$), and gamma absolute rejection ratio for neutrons (GARRn) are defined in Equations 1, 2, and 3, respectively. The

Table 1. Detection Criteria for Radiation Portal Monitor Neutron Detectors

Parameter	*Requirement*
Absolute neutron detection efficiency	$\varepsilon_{abs\ n} \geq 1.2 \times 10^{-3}$ (2.5 cps/ng of ^{252}Cf in a specified test configuration)†
Intrinsic gamma-neutron detection efficiency	$\varepsilon_{int\ \gamma,n} \leq 10^{-6}$ at 10 mR/hr
Gamma absolute rejection ratio for neutrons (GARRn)	$0.9 \leq$ GARRn ≤ 1.1 at 10 mR/hr
Cost	$30,000 per system

†The specified test configuration is ^{252}Cf encased in 0.5 cm of lead and 2.5 cm high-density polyethylene placed at a distance of 2 m (meters) perpendicular to the center face of the detector.

absolute neutron detection efficiency is the fraction of neutrons emitted from a neutron source that are detected by the detector. This criterion is set at a value of 2.5 cps/ng (counts per second per nanogram) of ^{252}Cf. The intrinsic gamma–neutron detection efficiency is the fraction of gamma-rays impinging on the detector surface that are misclassified as neutrons. This criterion is set at a value of 10^{-6} at a gamma-ray exposure of 10 mR/hr (milli-Roentgen per hour). The GARRn (gamma-ray absolute rejection ratio for neutrons) is the absolute neutron detection efficiency in the presence of a 10 mR/hr field divided by the absolute neutron detection efficiency without the gamma-ray present and must not change by more than 10% in the presence of the gamma-ray source.

$$\varepsilon_{abs\,n} = \frac{Number\ of\ \ pulses\ recorded}{Number\ of\ \ neutrons\ emitted\ \ from\ source} \tag{1}$$

$$\varepsilon_{int\,\gamma,n} = Number\ of\ \ gamma-rays\ misclassified\ as\ neutrons \tag{2}$$

$$GARRn = \frac{\varepsilon_{abs\,\gamma,n}}{\varepsilon_{abs\,n}} \tag{3}$$

The specific approach addressed in this work is to investigate thin film polymer scintillators containing ^{6}Li for the detection of thermal neutrons for RPM applications. The specific goals of this project are:

- to develop protocols for fabricating ^{6}Li-containing polymer scintillation films,

- to investigate neutron/gamma-ray discrimination in polymer scintillators,
- to develop a systematic technique by which transparent ^{6}Li-containing polymers can be synthesized, and
- to evaluate the developed polymer scintillators against the quantitative detection and discrimination criteria that are established for RPM applications.

In accordance with the specific goals of this project, this dissertation is organized as follows. Chapter 2 outlines the relevant theories regarding radiation interactions with matter. Chapter 3 outlines some of the most important recent advances in thermal neutron detection technology and provides a brief description of the phenomenon of scintillation in organic materials. Chapter 4 outlines the experimental design used to develop materials, relevant synthetic protocols, detector fabrication protocols, instrumentation used for characterization, and relevant calculation methods. Chapter 5 highlights important results and provides discussions of the importance of the results and satisfaction (or lack thereof) of detection and discrimination criteria. Chapter 6 includes a summary of the research, important conclusions, and recommendations for future effort.

Chapter 2: Radiation Interactions with Matter

Radiation interactions in matter are dependent on both the type and the energy of the impinging radiation as well as the identity and state of the target material. Radiation interactions are described herein as energy transferred from the impinging radiation (energy loss) to the target material (energy deposition). In this context, there are two different types of radiations: directly interacting and indirectly interacting. Directly interacting radiations are charged and generate ionizations and excitations directly by means of particle-to-particle Coulomb interactions. Indirectly interacting radiations are uncharged and can generate ionizations and excitations only by liberating secondary charged particles. The directly interacting radiations discussed here include heavy charged particles and negative beta particles (β^-). The indirectly interacting radiations discussed here include gamma-rays (γ) and neutrons (n). The theories presented in this chapter can be found in most classic textbooks on the subject.[9-12]

2.1. Heavy Charged Particles

A heavy charged particle is defined as any particulate radiation whose rest mass is equal to or greater than that of a proton, has a nonzero charge, and has a positive kinetic energy. These particles are created either by ejection from a larger nucleus which results in heavy charged particles with discrete energies, or by spallation which results in heavy charged particles with a range of energies. Heavy charged particles interact with matter primarily by Coulomb interactions with bound electrons. Heavy charged particles do interact with atomic nuclei, but these interactions are relatively rare and are generally not useful for generating signals inside radiation detectors. A useful description of the energy loss by charged particles due to Coulomb interactions with bound electrons is the collisional stopping power, S_c. This quantity describes the incremental loss of kinetic energy by the charged particle (dT) per unit path length (dx), as shown in Equation 4.

$$S_c = -\frac{dT}{dx} \tag{4}$$

The collisional stopping power is related to the properties of the impinging radiation and the target material as shown in Equation 5,

$$S_c = 4\pi r_0^2 m_e c^2 q^2 N_A \rho \frac{Z}{M_m} \frac{(T+Mc^2)^2}{T(T+2Mc^2)} \ln\left[\frac{2m_e c^2 T(T+2Mc^2)}{IP(T+Mc^2)^2}\right], \tag{5}$$

where r_0 is the radius of an electron, m_e is the rest mass of an electron, c is the speed of light, q is

the instantaneous net charge of the heavy charged particle, N_A is Avogadro's number, ρ is the mass density of the target material, Z is average atomic number of the target material, M_m is average atomic molar mass of the target material, T is the kinetic energy of the heavy charged particle, M is the mass of the heavy charged particle, and IP is the average ionization potential of the target material. Equation 5 demonstrates that the collisional stopping power is dependent on several aspects of the impinging ion and the target material. The collisional stopping power increases with increasing charge and mass of the ion and decreases with increasing kinetic energy of the ion. The collisional stopping power increases with increasing Z and increasing mass density of the target material and decreases with increasing average ionization potential of the target material. It should be noted that this expression for collisional stopping power of heavy ions treats all the electrons in a target material as being attached only to one element. While this is in error due to the existence of covalent bonds, the details of these corrections are adequately described elsewhere[13] and are beyond the scope of this discussion.

Because the mass of a heavy charged particle is so much greater than that of the electron with which it interacts, the acceleration of the charged particle is negligible relative to that of the electron with which it interacts as result of the Coulomb interaction. This implies that the velocity vector of a heavy charged particle is not appreciably altered by any single interaction with an electron. Rather, many interactions are required to attenuate the kinetic energy of a heavy charged particle and its track is relatively straight until it reaches the end of its path. However, the local density of ionization and excitation generated inside a target material by an impinging heavy ion is much greater than that generated by other radiations of comparable energies.

2.2. Beta Particles

Beta particles are electrons that are emitted from a nucleus as a result of a shift in nuclear stability caused by the transformation of a nuclear neutron into a nuclear proton. Both positive and negative beta particles exist; however, a discussion of positive beta particles is beyond the scope of this discussion. The emission of a negative beta particle (β^-) is always accompanied by the simultaneous emission of an antineutrino (υ'), as shown in Equation 6, for which the example is the beta decay of ^{3}H. As a result of energy conservation between the beta particle and the antineutrino, beta particles are emitted over a range of energies rather than as discrete energies.

$$ {}_1^3H \rightarrow {}_2^3He + \beta^- + \nu' \qquad (6) $$

The primary mechanism by which beta particles interact with matter is direct scattering from bound electrons. Both the incident beta particle and the bound electron are charged; hence, this mechanism is mediated by the Coulomb force. As a result, an expression for collisional stopping power for electrons similar to that for heavy charged particles can be derived and the dependence of the collisional stopping power follows similar trends as that for heavy ions. More importantly, due to conservation of momentum, the maximum kinetic energy that can be transferred from an incident beta particle to a bound electron is equal to one-half the value of the kinetic energy of the incident beta particle. This corresponds to a scattering angle of 180°, or a backscatter. A transfer of this relative magnitude of energy implies that the path of a beta particle can be significantly altered by a single interaction. Hence, the path of an electron is erratic rather than straight as is the case for heavy charged particles. The average distance between interactions is much greater for beta particles than for heavy charged particles of comparable energies. This

implies that beta particles have longer ranges in materials than heavy charged particles of comparable energies.

2.3. Gamma-Rays

Gamma-rays are photons that are emitted from a nucleus that correspond to transitions between nuclear energy levels. Gamma-rays are uncharged so they are generally not subject to Coulomb interactions, except in the case of pair production (discussed below). Rather, gamma-rays are subject to three interaction mechanisms: the photoelectric effect, Compton scattering, and pair production. The dominant interaction mechanism depends on both the energy of the incident gamma-ray and the average Z number of the target material. A plot of the average Z number against gamma-ray energy and the dominant interaction mechanisms in each region is shown in Figure 1.

At low gamma-ray energies, the photoelectric effect is the dominant interaction mechanism. In this mechanism, a bound electron absorbs an impinging photon and the total kinetic energy of the impinging photon is transferred to the absorbing electron. If the resulting energy of the electron is greater than the binding energy, the electron is ejected from the atom to which it is bound with kinetic energy equal to the difference between the energy of the impinging photon and the binding energy of the electron. At gamma-ray energies greater than 1.022 MeV, pair production becomes an important mechanism. This mechanism occurs when an impinging photon passes close to an atomic nucleus, particularly those with large atomic number. The positive charge on the nucleus polarizes the electric field of the photon and turns the photon into an electron and a positron. Both the electron and the positron behave as described in the preceding discussion on beta particles; however, at the end of its path the positron

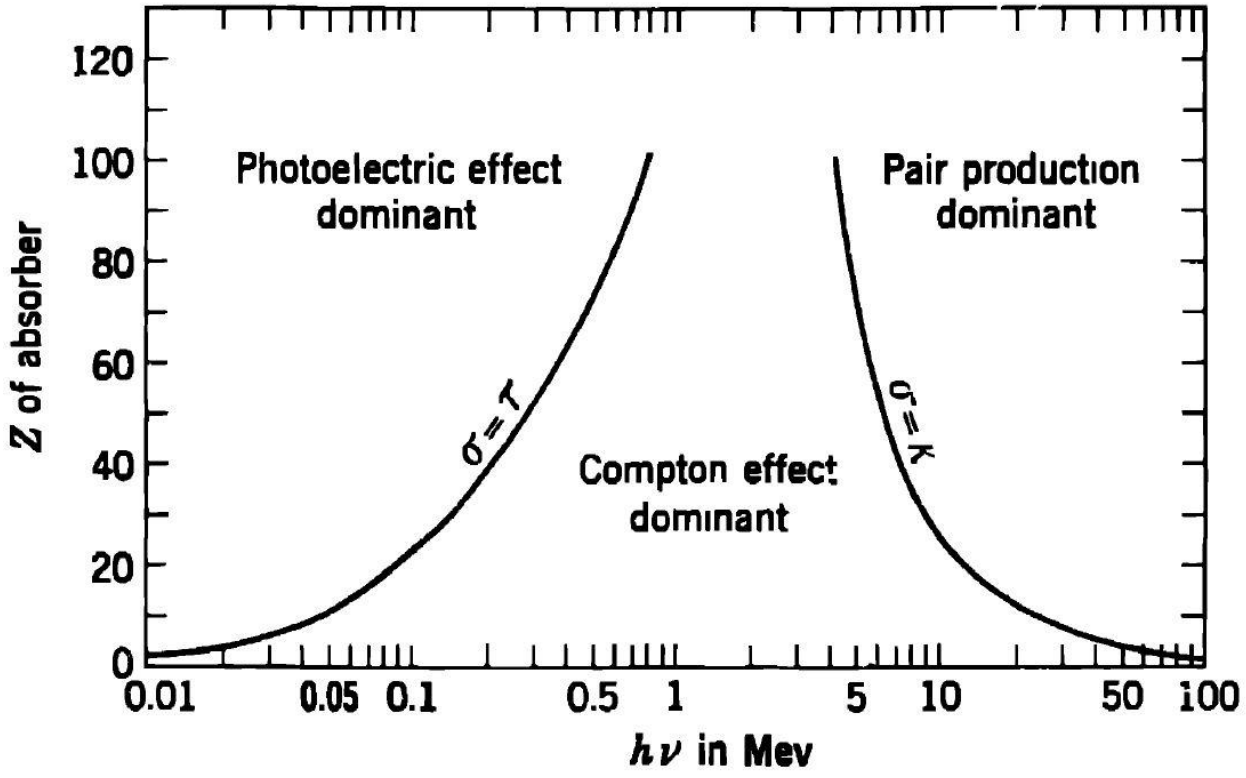


Figure 1. Gamma-Ray Interactions as Functions of Gamma-Ray Energy.

Image obtained from Evans.[14] τ is the probability that the photoelectric will occur, σ is the probability that the Compton effect will occur, and κ is the probability that pair production will occur.

undergoes annihilation with a bound electron, two 0.511 MeV photons are emitted 180° relative to each other. The probabilities of both the photoelectric effect and pair production increase relative to Compton scattering with increasing Z in the relevant energy ranges.

At intermediate energies, Compton scattering is the dominant interaction mechanism. In Compton scattering, an incident gamma-ray undergoes scattering from a bound electron. Kinetic energy is transferred from the incident gamma-ray to the electron and the angle of trajectory of the gamma-ray is altered, except in the extreme case of forward scattering. If the magnitude of the kinetic energy transferred to the electron exceeds the electron binding energy, then the electron will be liberated from the atom or molecule to which it is bound, resulting in a Compton electron. This liberated electron can then undergo the same interactions described above for beta particles. The energy of the scattered gamma-ray is reduced from the initial value and the direction of propagation is changed as described by Equation 7

$$h\nu' = \frac{h\nu}{1 + \frac{h\nu}{m_e c^2}(1 - \cos\theta)} \tag{7}$$

where $h\upsilon$ is the energy of the incident gamma-ray, $h\upsilon'$ is the energy of the scattered gamma-ray, m_e is the rest mass of an electron, c is the speed of light, and θ is the angle at which the gamma-ray is scattered. The number of Compton electrons has a peak at the energy described in Equation 8

$$T_C = \frac{2(h\upsilon)^2}{m_e c^2 + 2h\upsilon} \tag{8}$$

where T_C is the energy of the Compton electron. This peak in the frequency of the number of electrons gives rise to the Compton edge. The probability that a gamma-ray will interact with a material increases with increasing Z number and mass density of the target material.

2.4. Neutrons

Free neutrons can be produced by a variety of reactions such as spontaneous fission; (α,n) reactions; (γ,n) reactions; and deuterium/deuterium or deuterium/tritium fusion reactions.[11] The existence of the neutron as a single particle was confirmed in a report by James Chadwick in 1932 as quoted in the Preface.[1] Neutrons are uncharged particles so they do not interact with the electric or magnetic fields of matter. When a neutron enters matter, it interacts primarily by scattering from atomic nuclei, by spallation, or by absorption. High-energy neutrons (fast neutrons) undergo scattering with atomic nuclei and possess enough kinetic energy to break covalent bonds. A common neutron scattering event is that from hydrogen atoms in a target material. On collision, momentum is transferred from the incident neutron to the hydrogen atom such that the bond holding it in place is broken. The resulting released hydrogen atom usually has sufficient kinetic energy to dislodge its bound electron during a subsequent collision, resulting in a free proton. Because this free proton is charged and can interact with the local electric field in the target material, it creates ionizations and excitations in the surrounding target material. Fast neutrons can also cause spallation, a phenomenon in which a target nucleus is broken into multiple fragments. Lower energy neutrons that do not possess adequate energy to fracture covalent bonds cannot undergo these types of interactions. Rather, the dominant interaction mechanisms are elastic scattering and absorption. Absorption results when a target nucleus captures a neutron. On capture of a neutron, the absorbing nucleus is usually left in an

excited state. The excited nucleus can relax by fission, emission of a photon, reemission of a neutron, emission of a charged particle, or a combination of these mechanisms.

Thermal neutrons are neutrons whose kinetic energies are equal to thermal energy at 273 K, corresponding to approximately 0.025 eV. Thermal neutrons do not possess sufficient kinetic energy to cause spallation or to fracture covalent bonds. Because the energy of a thermal neutron is equivalent thermal energy at ambient temperature, vibrations created in materials as a result of thermal neutron scattering are relatively inconsequential. The primary interaction mechanism that thermal neutrons undergo that can be used for detection purposes is absorption by appropriate nuclides. Some common neutron capture nuclides, the corresponding thermal neutron capture reactions, absorption cross sections in b (barns, 1 b = 10^{-24} cm^2), and reaction energies are shown in Table 2.[11,15,16-18] After neutron capture, these nuclides emit secondary ionizing radiations that deposit energy in the surrounding matter by the relevant mechanisms described above.

Table 2. Thermal Neutron Capture Nuclides

Nuclide	*Reaction*		*Absorption Cross Section*[16]	*Reaction Energy*
^{3}He	$^{3}He(n,p^{+})\alpha^{2+}$		5333 b	0.764 MeV
^{6}Li	$^{6}Li(n,\alpha^{2+})^{3}H^{+}$		940 b	4.78 MeV
^{10}B	$^{10}B(n,^{7}Li^{*})\alpha^{2+}$	(94%)†	3835 b	2.792 MeV
	$^{10}B(n,^{7}Li)\alpha^{2+}$	(6%)	3835 b	2.310 MeV
^{113}Cd	$^{113}Cd(n,\gamma)^{114}Cd$		20,600 b	Various††
^{115}In	$^{115}In(n,\gamma)^{116}In$		202 b	Various††
^{157}Gd	$^{157}Gd(n,\gamma)^{158}Gd$		259,000 b	7.94 MeV†††

†$^{7}Li^{*}$ emits a 0.48 MeV γ about 10^{-13}seconds (s) after it is formed. This energy is not incorporated in the value shown for the reaction energy.

††Gamma-rays over a range of energies are emitted in these reactions.

†††This reaction produces a series of gamma-rays and internal conversion electrons.

Chapter 3: Current Materials for Thermal Neutron Detection

3.1. Thermal Neutron Detection

Thermal neutron detectors are evaluated for performance based on the neutron detection efficiency, neutron/gamma-ray discrimination capability, and the gamma absolute rejection ratio for neutrons, as described in Chapter 1. Other important characteristics are optical transparency, atmospheric stability, low average atomic number (for neutron/gamma-ray discrimination), low cost, moldability, fast response times, and the ability to be fabricated in large areas. Materials designed to detect thermal neutrons can be in gas, liquid, or solid form.[11,19-21] There are two general methods by which these materials can be employed to detect thermal neutrons which are shown schematically in Figure 2. In both methods, a thermal neutron is captured by a suitable nuclide, such as one listed in Table 2, which subsequently emits ionizing radiation. This ionizing radiation creates ionizations and excitations in the surrounding matter which are then detected by suitable means. The first method exploits the resulting ionizations to detect thermal neutrons. In

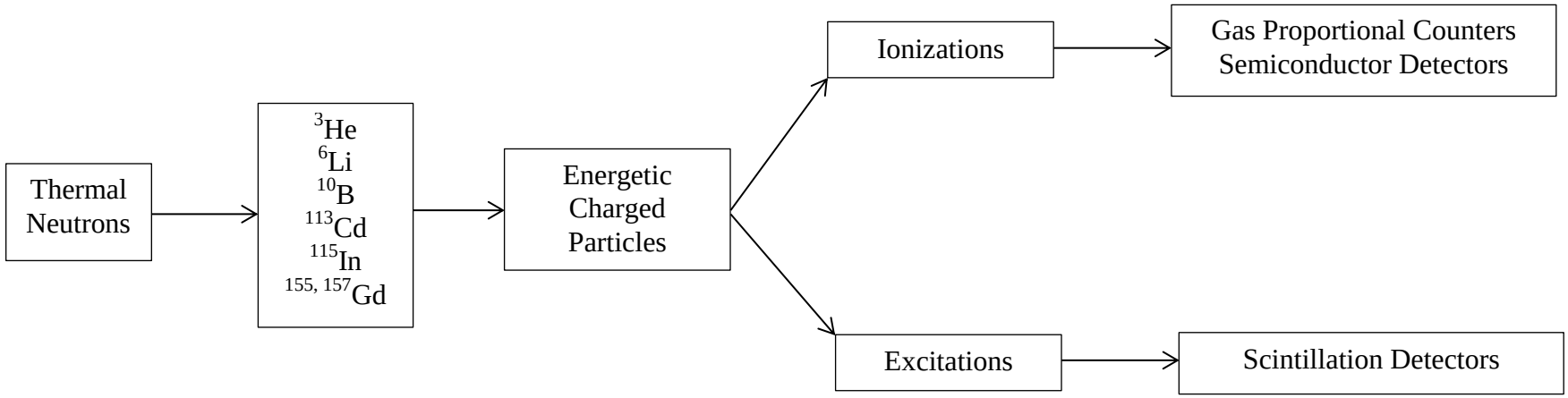


Figure 2. Schematic Illustrating the Different Methods by which Thermal Neutrons Can Be Detected.

this method, a voltage is applied across the detection material. Neutron capture and subsequent emission of energetic charged particles liberates secondary electrons from the surrounding material, creating positive and negative charges which migrate in opposite directions to electrodes. When the ions reach the electrodes, a count is registered. This method employs either gases (proportional counters) or solids (semiconductors). Gas proportional counters are relatively insensitive to gamma-ray interactions as compared to solids and liquids due to the low average density of gases. Solid-state semiconductors have much higher densities than gases and are therefore more susceptible to gamma-ray interactions. Further discussion of solid semiconductors for the purpose of thermal neutron detection is outside the scope of this discussion. The second method to detect thermal neutrons exploits the electronic excitations that result from thermal neutron capture and subsequent emission of energetic charged particles. The liberated electrons created from ionization can also generate further excitations in the material. In this method, visible light is emitted on relaxation of electronic excitations. This visible light is collected by a light collection device such as a photomultiplier tube (PMT) or avalanche photodiode and is registered as a count. In this work, a PMT is used as the light collection device. Scintillators are primarily made from liquids or solids and are thus more susceptible to gamma-ray interactions as compared to gases.

3.2. Current Neutron Detection Materials

Pacific Northwest National Laboratory (PNNL) has evaluated several thermal neutron detection systems for performance against the DHS criteria. Several of the evaluated detection systems and their performance against the criteria are listed in Table 3.[22-28] The first four listed

Table 3. Detection Systems Evaluated at PNNL

System	$\varepsilon_{abs,n}$	$\varepsilon_{int\,\gamma,n}$	*GARRn*
^{3}He Proportional Counter	3.0 cps/ng	8×10^{-8}	1.00
^{10}B-Lined Proportional Counter	3.0 cps/ng	6×10^{-9}	1.02
$^{10}BF_3$-Filled Proportional Counter	3.7 cps/ng	6×10^{-9}	---[†]
^{10}B-Lined Straw Tubes	4.2 cps/ng	1.5×10^{-9}	1.00
^{6}Li Glass Fibers	1.7 cps/ng	1×10^{-8}	1.07
^{6}Li/ZnS:Ag-Coated Scintillating Plastic[††]	4.0 cps/ng	1.6×10^{-8}	1.05
^{6}Li/ZnS:Ag-Coated Nonscintillating Plastic Fibers	2.4 cps/ng	5.8×10^{-7}	1.71

[†]Not reported.

[††]The value listed for $\varepsilon_{abs,n}$ for this material is estimated by scaling up the tested configuration to fit inside the current ^{3}He-based system.

are gas proportional counters and the last three are scintillators. All four proportional counters either meet or exceed the requirements whereas none of the scintillators meets the requirements. A representative list of other thermal neutron detectors that are either commonly used or well-known along with the material type, mode of operation, and thermal neutron capture nuclide are listed in Table 4.[2,7,11,15,19,21,22,28-40] Of the detectors listed, the ^{6}Li foil proportional counter is the only one that operates in proportional mode. The remaining detectors are scintillators except for indium lead phosphate glass, which on thermal neutron capture creates high energy electrons that produce Cerenkov photons. Inorganic scintillators are classified as either intrinsic or extrinsic scintillators. Intrinsic scintillators are materials that scintillate as the pure material without any added dopants whereas extrinsic scintillators require a purposely-added dopant in order to scintillate. The nomenclature convention followed for inorganic scintillators is matrix:dopant. Of the scintillators listed in Table 4, lithium glass doped with cerium is the most relevant to this

Table 4. List of Representative Thermal Neutron Detection Systems

Detector	*Type*	*Mode*	*Capture Nuclide(s)*
^{6}Li Foil Proportional Counter	Solid/Gas	Proportional	^{6}Li
Lithium Glass (Ce^{3+})	Inorganic Glass	Scintillation	^{6}Li
$^{6}LiI:Eu^{2+}$	Inorganic Crystal	Scintillation	^{6}Li
$^{6}Li_6Gd(BO_3)_3:Ce^{3+}$	Inorganic Crystal	Scintillation	^{6}Li, ^{155,157}Gd
Lithium Borate Glass (Ce^{3+})	Inorganic Glass	Scintillation	^{6}Li, ^{10}B
$^{6}LiF/ZnS:Ag^{+}$	Inorganic Composite	Scintillation	^{6}Li
$Cs_2{}^{6}LiYCl_6:Ce^{3+}$	Inorganic Crystal	Scintillation	^{6}Li (thermal) ^{35}Cl (fast)
$^{6}LiF/CaF_2:Eu^{2+}$	Inorganic Composite	Scintillation	^{6}Li
Indium Lead Phosphate Glass	Inorganic Glass	Cerenkov	^{115}In
^{6}Lithium Salicylate	Organic Crystal	Scintillation	^{6}Li

work. The composition used herein is referred to GS20 which is 57% SiO_2, 17% $^{6}Li_2O$ (enriched to 95% ^{6}Li), 18% Al_2O_3, 4% MgO, and 4% Ce_2O_3.[37]

3.3. Scintillators

3.3.1. Introduction

Scintillators are materials that emit photons in the ultraviolet or visible wavelength (λ) range by electronic de-excitation in response to absorption of energy from ionizing radiation. A scintillator must be mounted on the face of a PMT which generates an electronic signal in response to the photons that are emitted by the scintillator. The signal generated by the PMT is amplified electronically to give a digitized response. Further discussion of the associated electronics is given in section 4.5.3. Scintillators can be in gas, liquid, or solid form. Gaseous scintillators are outside the scope of this discussion. Liquid and solid scintillators can be made from either inorganic or organic materials or from hybrid inorganic/organic materials. Inorganic

scintillators can be either amorphous or crystalline materials. Organic scintillators are primarily liquid, solid crystalline, or solid amorphous materials. Thermal neutron detectors based on solid amorphous polymers are the focus of this work and will be discussed in detail.

Two important quantities related to the description of scintillator properties that need to be defined at this point in the discussion are light yield and resolution. Light yield, *LY*, is defined in Equation 9 as the number of photons emitted by a scintillator in response to 1 MeV of energy deposited by impinging radiation (ph/MeV). Energy deposition by heavy charged particles produce fewer photons in a scintillator relative to that by beta particles of comparable energies; thus, light yield is commonly reported as the number of photons emitted by the scintillator in response to deposition of 1 MeV of energy from an impinging beta particle. Light yield can also be reported as the number of photons emitted per impinging particle or the number of photons emitted at a relevant spectral feature. All three formalities will be used in this dissertation and clarification will be given regarding which definition is used at the relevant points. If no clarification is given, then it is to be assumed that *LY* is reported in ph/MeV for beta particles.

$$LY = \frac{Photons\,emitted}{1 MeV\,deposited} \tag{9}$$

Resolution is the energy spread in the light yield signal. It is defined as shown in Equation 10 as the position of the peak divided by the width of the peak at one-half the maximum value (*FWHM*, full width at half max).

$$Resolution = \frac{Peak\ Position}{FWHM} \tag{10}$$

3.3.2. Inorganic Scintillators

One of the most common and well-researched areas of solid state scintillation detection materials is in the form of crystalline and amorphous inorganic solids. A practical problem with solid crystalline scintillators is that many are hygroscopic and must be synthesized, handled, and operated under anhydrous conditions. Further, synthesis of these materials usually requires specialized equipment, high processing temperatures, and stringent purity of starting materials, all of which result in a higher cost of the final scintillator. Current synthetic methodology also makes many single crystals very difficult to grow in large sizes and they cannot be readily molded. Amorphous inorganic scintillators generally have lower light yields than single crystals; however, they are easier to synthesize and compositions are not as restrictive as single crystals. Moreover, many inorganic glasses are not hygroscopic and can be readily molded into various shapes and sizes.

3.3.3. Organic Scintillators

3.3.3.1. Liquid Scintillators

Liquid scintillators that are designed to detect thermal neutrons generally comprise three components: an aromatic solvent, a light-emitting molecule (fluor), and a compound containing a nuclide capable of capturing neutrons. Common aromatic solvents are benzene, toluene, xylene, and pseudocumene. These solvents are used because they are intrinsically fluorescent due to the aromatic nature of the π-electrons. The wavelengths of fluorescence emission of these solvents are in the range 275 – 320 nm.[41,42] The region of maximum quantum efficiency for common PMTs is in the range 390 – 450 nm; thus, a fluor must be added to absorb the excitation energy from the solvent and reemit photons at longer wavelengths. It is sometimes necessary to use

multiple fluors to move the emission wavelength to the appropriate region. The third component is a suitable compound containing a nuclide capable of releasing charged particles after absorption of a thermal neutron. Ionic or nonionic surfactants can be added to these solutions to improve compatibility with water and water-soluble components.

3.3.3.3. Single Crystals

Lithium-6 salicylate (^{6}LiSal) has been grown as a single crystal scintillator for thermal neutron detection.[36] This material exhibits pulse-shape discrimination properties between thermal neutrons and gamma-rays. This material is fluorescent in the region of sensitivity of common PMTs so it does not require additional fluors.

3.3.3.4. Organic/Inorganic Hybrid Materials

Silicon-based scintillators derived from sol-gel methodology containing both inorganic and organic components connected by covalent bonds have been developed to detect thermal neutrons.[43,44] Reports of these materials demonstrate that they can scintillate in the presence of thermal neutrons and are transparent at low loadings of ^{6}LiCl and ^{6}LiSal, but no reports of light yields have been given. The materials demonstrate some separation of gamma-ray and neutron responses but no indication of detection efficiencies have been reported. Moreover, these materials are very brittle and are subject to mechanical failure, even during the course of careful handling.

3.4. Polymer Scintillators

3.4.1. General Remarks

Polymer scintillators are the primary topic of this dissertation. The use of organic polymers as scintillators has many advantages over many other scintillating materials such as hygroscopic single crystals and inorganic glasses in that selected polymers are air-stable, do not require high processing temperatures, are relatively inexpensive, are easy to fabricate in large areas in a wide range of geometries, and have fast response times.[45] Common commercially available polymer scintillators are generally based on aryl vinyl polymers such as polystyrene (PS) and poly(vinyl toluene) (PVT). Scintillation in aryl vinyl polymers occurs according to principles similar to liquid scintillators.

3.4.2. Photophysics of Organic Compounds

Aryl vinyl polymers comprise an aromatic ring covalently bonded to a hydrocarbon backbone and are the primary class of polymers of interest in this work. The emission spectra of aryl vinyl polymers under both ultraviolet- (UV) and X-ray-induced excitation are nearly identical, indicating that the final emissive states are the same.[46,47] Thus, a theoretical discussion of the photophysics of aromatic compounds under UV-induced excitation provides an adequate framework by which the photon emission processes in scintillation can be understood and is given in detail below. The mechanisms of excitation, however, are very different: UV- induced excitation involves absorption of a photon to generate excited electronic states whereas X-ray-induced excitation generates excited states by the liberation of energetic electrons. Thus, the theoretical framework of the generation of excited states by UV light only peripherally applies to generation of excited states by ionizing radiation and a separate discussion is given below.

Photon absorbance by molecules is commonly described in terms of the Beer–Lambert law which is shown in Equation 11,

$$Absorbance = \epsilon l [M], \tag{11}$$

where ϵ is the molar extinction coefficient, l is the path length the photon must travel through the medium, and [M] is the concentration of the absorbing species.[48] The molar extinction coefficient is specific to each substance, is wavelength-dependent, has peak values at the wavelengths corresponding to the energy differences between the ground state and the relevant excited states. On electronic excitation by UV light at an appropriate wavelength, a π electron on an aromatic ring of an aryl vinyl polymer in the singlet ground state (S_0) can be promoted to a particular vibrational level in an excited singlet state (S_1). Before any electronic processes occur, vibrational relaxation to the lowest vibrational level of the S_1 state occurs on the order of 10^{-12} seconds.[49] The energy in the S_1 state can then undergo any of the following electronic processes:

- migrate along the pendant groups (energy migration),
- transfer to a purposely added impurity (energy transfer),
- relax to the S_0 state by photon emission (fluorescence),
- relax to the S_0 state without photon emission (internal conversion, IC),
- transfer to an adventitious impurity or structural defect (impurity quenching), or
- dissipate by a change in electron spin to generate an excited triplet state, T_1 (intersystem crossing, ISC).

It should be noted that the term “quenching” is used in this context as any process that converts the excitation energy into a form not usable for photon emission. The aforementioned processes are shown schematically in the Jablonski diagram in Figure 3.

The relative probability that a state will undergo a particular photophysical process is given by the respective rate constant of the process divided by the sum of the rate constants of all the other possible processes that the state can undergo. This probability is called the quantum yield and is shown in Equation 12

$$\phi_i = \frac{k_i}{\sum_j k_j} \tag{12}$$

where ϕ_i is the quantum yield of process i, k_i is the rate constant of process i, and $\Sigma_j k_j$ represents the sum of the rate constants of all other possible photophysical processes the state can undergo.

The first photophysical process described above for S_1 states is migration of electronic excitations along the pendant groups. This phenomenon has been extensively investigated by many researchers[50-59] and the mechanism by which it occurs can be described by the following discussion. A electronic transition between two states m and n that is induced by absorption of a photon can be described by Equation 13 in Dirac bracket notation

$$R_{mn} \approx < \varphi_m | \hat{R} | \varphi_n > < \zeta_m | \zeta_n > < I_m | I_n > \tag{13}$$

where φ_i is the orbital wavefunction, $\hat{R}$ is the transition dipole operator, ζ_i is the nuclear wavefunction, and I_i is the electron spin. The intensity of photon absorption that results in a

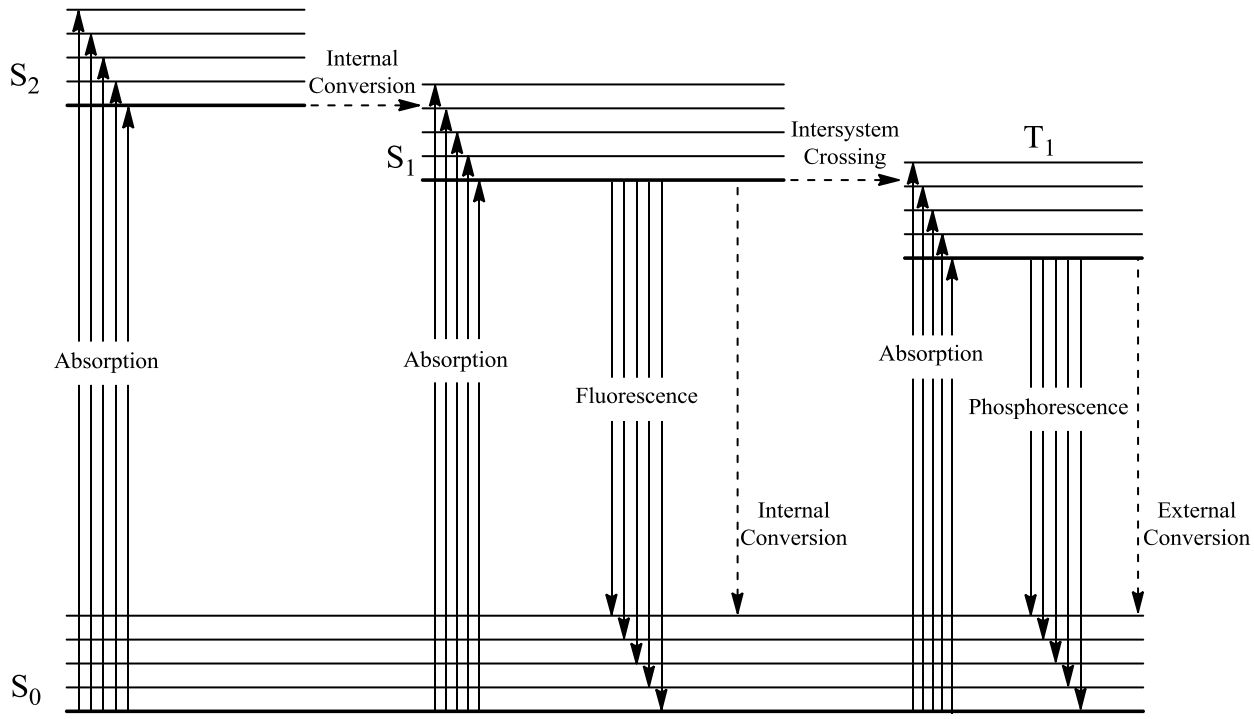


Figure 3. Jablonski Diagram Illustrating Mechanisms by which Electronic Excitations Can Relax.

Image adapted from Skoog.[48] The singlet ground state is labeled S_0, the first excited singlet state is labeled S_1, the second excited state is labeled as S_2, and the first triplet state is labeled T_1. The thick horizontal lines are the vibrational ground states in each electronic state and the thin horizontal lines are excited vibrational levels of each electronic state. Vibrational relaxation is omitted for clarity. Dotted arrows indicate processes that occur without emission of a photon.

transition from state m to state n (A_{mn}) is given by Equation 14.

$$A_{mn} = \left| R_{mn} \right|^2 \tag{14}$$

Within the Born–Oppenheimer approximation, the nuclear terms χ_i in Equation 13 are negligible. Thus, one can see that for an $S_0 \rightarrow S_1$ transition, the intensity of photon absorption is related to the degree of spin conservation in the process as well as the difference in dipole moments between the two states. An increase in the change in dipole moment between the two states increases the probability that the transition will occur. In aryl vinyl polymers, an S_1 state that is in proximity to the S_0 state on an adjacent pendant can polarize the neighboring S_0 state toward its S_1 state by virtue of the dipole moment. The excitation can then "hop," or migrate, from the initially excited pendant group to the adjacent pendant group due to resonance of the dipole vectors between the S_0 and S_1 states of the two pendant groups. Energy migration is a nonradiative process because it is not mediated by a photon and occurs without the dissipation of any of the excitation energy.

The second process described above is energy transfer which involves the transfer of the excitation energy from the polymer (donor) to a purposefully added impurity such as a fluor (acceptor). Energy transfer can occur if the donor emission spectrum overlaps the acceptor excitation spectrum. If the donor and acceptor are in adequate proximity, this process can occur by direct radiationless transfer as a result of dipolar resonance. This particular mechanism of energy transfer is called Förster resonance energy transfer (FRET) and was first elucidated by Förster in 1948.[60] The efficiency of FRET (E) is given by Equation 15

$$E = \frac{1}{1+\left(\frac{FR_{DA}}{FR_0}\right)^6} \tag{15}$$

where FR_{DA} represents the distance between donor and acceptor and FR_0 is the Förster distance which is defined for the solid state as the distance at which the probability of transfer is 50%. The value of FR_0 can be calculated using Equation 16

$$FR_0^6 = \frac{9000\ln(10)\phi_D\Lambda^2}{128\pi^5 RI^4 N_A}\int_0^\infty \sigma_{fluor}^D(\lambda)\epsilon_A(\lambda)\lambda^4 d\lambda \tag{16}$$

where ϕ_D is the quantum yield of fluorescence of the donor, Λ is an orientation factor (2/3 for random orientation), RI is the refractive index of the medium, N_A is Avogadro's number, λ is wavelength, $\sigma_{fluor}^D(\lambda)$ is the fluorescence spectrum of the donor normalized to an integrated area of 1, and $\epsilon_A(\lambda)$ is the extinction coefficient of the acceptor as a function of wavelength.

The third process described above is fluorescence. In this process, relaxation of the S_1 state to the S_0 state is accompanied by photon emission. This phenomenon occurs on the timescale of 10^{-9} seconds for most organic compounds. The fourth process, internal conversion (IC), describes a radiationless transition from the S_1 to the S_0 state that dissipates the energy by vibrations rather than by photon emission. The fifth process is a quenching phenomenon and results in dissipation of the excitation energy by adventitious impurities or structural defects and does not result in emission of a photon.

The sixth process described above is intersystem crossing (ISC) and involves the population of a triplet state by a singlet state. This process involves a change in electron spin

which is a forbidden process according to Equation 13. However, due to spin-orbit coupling and other possible distortions in the orbital wavefunctions, ISC does have a finite rate constant in most organic compounds. The rate of ISC can be increased by incorporating a heavy or electronegative atom such as bromine onto the chromophore. Hund's rule of maximum multiplicity indicates that the state with the maximum number of parallel spins is of the lowest energy. Thus, the T_1 state is lower in energy than the S_1 state and during ISC the excess energy is dissipated as heat. The resulting energy in the T_1 state can:

- migrate along the polymer chain (energy migration),
- relax to the S_0 state by photon emission (phosphorescence),
- relax to the S_0 state without photon emission (external conversion),
- transition back to the S_1 state by thermal energy (external conversion), or
- undergo annihilation with another T_1 state to produce an S_1 and an S_0 state. This S_1 state can then undergo any of the photophysical processes described above for S_1 states. Fluorescence resulting from this S_1 state is called delayed fluorescence because it occurs on a timescale that is longer than normal fluorescence.

These processes are generally not useful for generating signals inside scintillators and will not be discussed in detail.

3.4.3. Generation of Excited States by Radiation

The emission processes in scintillation are not much unlike those described for UV-induced fluorescence. The primary difference between scintillation and UV-induced fluorescence

is the mechanism by which the excited states are generated. In scintillation, ionizing radiation undergoes electrostatic interactions with bound electrons, generating ionizations and excitations in the surrounding matter. It should be noted that the following discussion omits the effects of strong local electrical fields due to the presence of free ions, the damage resulting from ionization, and displacements due to nuclear collisions on the fluorescence emission properties of organic scintillators. These processes do occur and result in a decrease in the quantum yield of emission from the S_1 state, but a sufficiently accurate discussion of the scintillation mechanism in organic materials can be given by ignoring these complications. In this context, an electron with which ionizing radiation interacts can undergo any of the following processes:

- it can be liberated to form a positive and negative ion,
- it can be promoted to generate the first excited states (S_1 or T_1), or
- it can be promoted to a higher excited state.

The first process involves the transition of an electron directly from the S_0 state to either the S_1 or T_1 states. These excited states can then undergo any of the relevant processes described above. This process is rare as compared to either ionization or promotion to higher excited states.

If an electron is liberated, it can produce additional excitations and ionizations along its path. If the liberated electron does not possess much kinetic energy and remains in the vicinity of the positively charged molecule to which it was initially bound, it can recombine to regenerate a neutral molecule. This recombination process usually results in the direct formation of excited states.[61,62] Electron spin statistics for organic molecules predicts that because the initial identity of the electron spin is not retained once the electron is ejected into the continuum, spin selection

rules do not apply and 25% of the states that are generated as a result of recombination are singlets whereas the other 75% are triplets.[63]

The third process involves the excitation of an electron to a higher excited state and is the most relevant to this discussion. Kasha's rule states that all the optical photons of appreciable intensity that are emitted by aromatic molecules are from the lowest excited states of each multiplicity (S_1 or T_1).[49] Thus, if an electron is promoted to a higher excited state, photon emission is preceded by relaxation of the higher excited state to the S_1 or T_1 state by internal or external conversion. The probability that ionizing radiation will generate a particular excited state has been estimated by the optical approximation model as the ratio of the oscillator strength to the energy of the excited state.[64] Measurements of the populations of the excited singlet states that are generated in response to irradiation by beta particles in various laboratories indicate that this approximation works remarkably well for aromatic compounds.[65,66] Approximately 0.3% of the excited states generated in benzene and its hydrocarbon-substituted analogs from irradiation by beta particles are S_1 states and the remainder are higher excited states. Nearly all of these states relax by internal conversion to the S_1 (or T_1) states. Thus, due to the spin-forbidden nature of phosphorescence, the vast majority of the photons that are emitted from aromatic organic compounds in response to ionizing radiation are due to the relaxation of the S_1 state to the S_0 state.

As described in section 2.1., the local density of ionization created by heavy ions is much greater than that created by beta particles or Compton-scattered electrons generated by gamma-rays. Additionally, the secondary electrons generated by heavy ions have on average much lower energies and consequently much shorter ranges relative to those generated by beta particles or gamma-rays. This implies that a greater probability that secondary electrons generated by heavy

ions will undergo ion recombination due to the proximity of the positive and negative ions generated in the ionization column. This implies that a larger fraction of the excited states resulting from heavy ions are generated in accordance with spin statistics rather than selection rules. Spin statistics predicts that 25% of the recombinations will be singlets whereas 75% will be triplets; selection rules for electronic excitation requires spin conservation and assuming that the molecule is initially in the S_0 state dictates that nearly all excitations are singlets. Thus, a significantly greater quantity of triplet states are generated by heavy ions as compared to beta particles or Compton-scattered electrons of comparable energies. Because the relaxation of the T_1 state to the S_0 by photon emission is a spin-forbidden process, much of the excitation energy resulting from energy deposition from heavy ions is converted into vibrations rather than into photons. As a result, the number of photons generated by a scintillator in response to beta particles or gamma-rays is significantly greater than the number generated by heavy ions of comparable energy. This phenomenon gives rise to what is known as the pulse height deficit, which is the ratio of the number of photons emitted in response to a heavy ion to the number of photons emitted in response to a beta particle with both quantities normalized to a particle energy of 1 MeV.[11] The larger number of triplet states generated over a smaller volume also results in a higher rate of triplet–triplet annihilation for heavy ions. As stated previously, triplet–triplet annihilation results in an S_1 state and an S_0 state. Thus, the resulting time distribution of fluorescence resulting from triplet–triplet annihilation is longer than that resulting from direct generation of the S_1 state and subsequent fluorescence. Due to the presence of delayed fluorescence, the scintillation light generated by heavy ions tends to be emitted over a longer period of time. The difference in the emission times of the pulses generated by heavy ions and

those generated by beta particles or gamma-rays can be exploited by proper electronics to differentiate between the events and is known as pulse shape discrimination.

The physics and chemistry of polymer scintillators have been studied extensively since the 1950s. The most commonly studied polymers for scintillation applications are PS, PVT, and poly(methyl methacrylate) (PMMA). PS and PVT fluoresce in the wavelength range 275 – 350 nm. Common commercially-available PMTs are most sensitive in the wavelength range 390 – 440 nm. Thus, these polymers must be doped with small quantities of appropriate fluors to shift the wavelength of emission to the region of maximum sensitivity of the PMT. It has been shown that in order for fluors to function efficiently in a polymer matrix, the excitation spectrum of the fluor must overlap with the emission spectrum of the polymer matrix, as required by FRET. It was first postulated that the phenomenon of scintillation involved photon emission from the polymer matrix and subsequent reabsorption of the photon by the added fluor; however, it was shown that the fluorescence lifetime decreased on addition of the fluor.[46] This demonstrated that the transfer of energy from the polymer to the fluor cannot be mediated by a photon and must instead be a radiationless process.[67,68]

Generally, fabrication of polymer scintillators involves the dissolving a fluor in a liquid monomer then polymerizing the solution by bulk thermal polymerization. Neilson studied the effects of different fluors at low concentrations on the polymerization of vinyl toluene.[54,55] It was shown that 2,5-diphenyloxazole (PPO), *p*-terphenyl (PTP), 1,4-bis(5-phenyloxazol-2-yl)benzene (POPOP), and 1,1',4,4'-tetraphenylbutadiene (TPB) do not affect the polymerization rate, indicating that chain transfer reactions to these molecules is negligible.[69,70] The fluor 9-methylanthracene (9MA), however, does undergo chain transfer reactions and the scintillation efficiency decreases as the polymerization proceeds toward completion.[70]

Birks showed that an excited polymer segment can transfer energy to residual monomer or solute, or form an excimer or multimer which subsequently emits a photon.[71] The transfer to residual monomer and excimer or multimer emission act as energy traps. However, energy localized at traps can still transfer to solute molecules via either photon emission and reabsorption or by long-range dipolar resonance interactions.[72]

Inagaki studied scintillators based on PMMA doped with various fluors.[73] Because PMMA does not comprise aromatic structures, it was necessary to add naphthalene as a primary fluor along with two additional fluors to shift the wavelength of emission to the region of PMT sensitivity. The most comprehensive study of PMMA-based polymer scintillators is given by Salimgareeva.[74,75] The study demonstrated that incorporation of 1,1,3-trimethyl-3-phenylindan (TMPI) as a single fluor improved both the light output and the radiation sensitivity relative to all the other fluors and fluor combinations studied. The use of polymerizable fluors copolymerized with either methyl methacrylate or styrene has also been studied. It was determined that incorporation of the polymerizable fluor increased the scintillation efficiency relative to the solid solution of the fluor in the polymer matrix.[76,77]

Gunder studied the effect of monomer structure on scintillation efficiencies of alkyl-substituted polystyrenes.[78] In this work, it was postulated that the light yield is greater for polymers in which the electron density is greater on the carbon atom of the aromatic ring that is bonded to the polymer backbone. This theory provides the proper correlation in the scope of the polymers studied in their work; however, it does not apply to all aryl vinyl polymers that have been studied as scintillators. Though ignored by Gunder, the most formative work that was located by the author regarding the correlations between molecular structure and scintillation efficiency is given by Sangster and Irvin.[79] They were able to observe several trends in the

relationship between structure and scintillation efficiency such as structural rigidity and diamagnetic anisotropy; however, no quantitative theory permitting the prediction of scintillation efficiency from first principles has been developed for organic scintillators to date.

3.4.4. Polymer Scintillators as Thermal Neutron Detectors

Polymer scintillators designed to detect thermal neutrons require the presence of three components: a neutron capture nuclide such as those listed in Table 2,[32] a polymer that both contains aromatic groups that can facilitate scintillation and is mechanically robust, and one or more fluors to collect the excitations from the polymer and emit photons in the wavelength region of spectral sensitivity of the light collection device. Materials that contain all these components are usually fabricated as polymer/salt or polymer/crystal composites. Scintillation light is generated inside the material and must escape the surface in order to be detected; hence, the ideal scintillation detector is completely transparent to its own scintillation light.[80] It is a common issue that incorporation of inorganic salts into organic polymers usually results in phase-separation which generally gives brittle and opaque materials. Phases that have different indices of refraction as compared to the surrounding matrix can act as scattering sites for optical photons. Various optical photon scattering models have been proposed for different variations of particle sizes and shapes, wavelengths of incident light, and refractive indices of the particles and accompanying matrices.[81,82] In all the models, three properties of the composite can be modified in order to fabricate a transparent composite. The first is to match the refractive index of the particles with that of the polymer matrix, which occurs only for a very few select composites. The second is to reduce the number of particles to approximately zero. This is not practical in all applications. The third is to reduce the size of the particles to tens of nanometers or less. The resulting nanoparticles often agglomerate, increasing the average size of the phase and

subsequently resulting in a reduction in transparency. These problems have hampered the development of polymer scintillators containing ^{6}Li for thermal neutron detection applications. The problem of reduced optical transparency in polymers containing ^{6}Li is one of the focuses of the work presented in this dissertation.

3.4.4.1. PVT Containing *o*-Carborane

One of the most common polymer scintillators for thermal neutron detection is PVT containing *o*-carborane which is a polyhedral molecule with composition $C_2H_{12}B_{10}$.[83] *O*-carborane is soluble in PVT at low concentrations (< 10%) and forms transparent composites. However, the larger pulse height deficit associated with the fission products of ^{10}B compared to that of ^{6}Li results in fewer photons that can be generated by ^{10}B relative to ^{6}Li. This decreases the probability that ^{10}B-loaded materials can facilitate pulse height discrimination to differentiate between neutron and gamma events. This composite with proprietary fluors is commercially available from Eljen Technologies under the trade names EJ-254 and EJ-339A.

3.4.4.2. Poly(2-Vinyl Naphthalene) Containing ^{6}Lithium Salicylate

Poly(2-vinyl naphthalene) (P2VN) films containing ^{6}LiSal and polyfluorene dyes have recently been reported as thermal neutron detectors, work to which the author has contributed.[84,85] This polymer is relatively expensive and the resulting composite films are brittle and hygroscopic due to the presence of ^{6}LiSal. Also, they are not transparent due to phase separation and crystallization of the lithium salicylate in the polymer matrix. Even so, scintillators based on this polymer have light yields exceeding comparable scintillators made from PS or PVT.

3.4.4.3. PVT Containing Gadolinium Isopropoxide

PVT containing gadolinium isopropoxide and appropriate fluors has been developed as a polymer scintillator capable of detecting thermal neutrons.[86] This material exploits the gadolinium neutron capture reaction to detect thermal neutrons. The composite is transparent and can be loaded with gadolinium such that the intrinsic neutron detection efficiency can be as high as 46% An issue associated with this material is that the gadolinium capture reaction produces gamma-rays, precluding the ability of this material to be used for neutron/gamma-ray discrimination applications.

3.4.4.4. Polyethylene Naphthalate Containing ^{6}LiF

Polyethylene naphthalate (PEN) films containing ^{6}LiF have been developed as polymer composite thermal neutron scintillation detectors, work to which the author has contributed.[87] These composites are mechanically robust and not hygroscopic; however, they are not transparent. The wavelength of emission of this polymer is in the range of sensitivity of common PMTs so additional fluors are not necessary but can be added to improve the light yield. The light yield of neat scintillators based on this polymer are approximately 2,500 photons per thermal neutron.

3.4.4.5. Polymer Composite Fibers

Polymer scintillators containing various ^{6}Li compounds have been fabricated in fiber form by melt- and electrospinning techniques.[88] Difficulties with light collection from the fibers results in low reported light yields. I have contributed to developing methods by which the light collection efficiency can be improved but a discussion of this work is not included in this dissertation.

Chapter 4: Experimental Design and Instrumental Methods

In this study, ^{6}Li was selected as the thermal neutron capture nuclide because of its large capture cross section (940 b) and large reaction energy (Q = 4.78 MeV). On absorption of a thermal neutron, ^{6}Li fissions into an alpha particle (2.05 MeV) and a triton (2.73 MeV).[11] These charged particles deposit their kinetic energy in the matrix primarily by electrostatic interactions with bound electrons to form ionizations and excitations. This energy is then collected by appropriate fluors and shifted to wavelengths suitable to be collected by a PMT.

4.1. Analysis and Purification of ^{6}LiOH

Lithium hydroxide monohydrate enriched in ^{6}Li was obtained from Y-12 at Oak Ridge National Laboratory. The degree of enrichment of ^{6}Li was determined by dissolving the material in water at a concentration of 5 mg/mL, filtering with a 450 nm Nylon filter, and analyzing by QSTAR tandem liquid chromatography/mass spectrometry (LC/MS). The degree of enrichment

was determined by integrating the area under the peak corresponding to $^{6}LiOH \cdot H_2O$ (H^+) relative to that corresponding to $^{7}LiOH \cdot H_2O$ (H^+).

The stock $^{6}LiOH$ was purified by dissolving in methanol at a concentration of 13 g/L at room temperature and filtered using a 1 μm filter. The filtrate was collected and the methanol was evaporated from the filtrate at 140°C under a nitrogen atmosphere. The resulting material analyzed for purity by powder X-ray diffraction (p-XRD) and inductively-coupled plasma–optical emission spectroscopy (ICP-OES) using analysis for Li at 670.781 nm in axial mode. The purified material was stored in a polypropylene bottle sealed with parafilm under an inert atmosphere. LiOH in the presence of atmospheric conditions has the tendency to form a monohydrate and a carbonate, according to Equations 17 and 18. It has been determined that under normal atmospheric conditions, anhydrous LiOH first forms a monohydrate, then the monohydrate forms lithium carbonate.[89] It is thus possible to determine the integrity over time of purified LiOH by monitoring for hydrate and carbonate formation.

$$LiOH + H_2O \rightarrow LiOH \cdot H_2O \quad (17)$$

$$2\,LiOH \cdot H_2O + CO_2 \rightarrow Li_2CO_3 + 3\,H_2O \quad (18)$$

4.2. Synthesis of Lithium Salts

The primary protocol for the synthesis of lithium salts was titration. Purified $^{6}LiOH$ was dissolved in water and the corresponding acid was dissolved in water in a separate container. The two solutions were mixed by adding the lithium solution dropwise to the acid solution with magnetic stirring at room temperature. The solution was maintained slightly acidic (pH ≈ 6) to

ensure complete consumption of the ^{6}LiOH and to reduce the tendency of the organic salts to decompose.[36] Acids that were insoluble in water were dissolved in a 2:1 solution of acetone and water. For lithium salts that were soluble in the reaction medium, the salt was collected by evaporating the solvent, then dehydrating the salt at reduced pressure over P_2O_5. For salts that were insoluble in the reaction medium, the precipitated salt was collected by vacuum filtration and washed with acetone, then residual solvents were removed at reduced pressure over P_2O_5.

Table 5 contains a complete list of all lithium salts synthesized and some relevant properties of each. The density and weight percent of ^{6}Li in the salt is important because higher values for these properties give a greater atom density of ^{6}Li which means that a smaller volume of salt is required to achieve a desired number of lithium atoms. Hygroscopicity is indicated because incorporation of hygroscopic salts into hydrophobic polymer matrices results in brittle composites and migration of the salt to the polymer/air interface over time. Inspection of the compounds in Table 5 for salts that are not hygroscopic and have high atom densities of ^{6}Li reveals that ^{6}LiF is the most appropriate selection for this particular application, with $^{6}Li_3PO_4$ as the second most appropriate. ^{6}LiSal is a special case because it exhibits fluorescence emission at a wavelength suitable to be detected by common PMTs. The use of these three lithium salts are explored in this dissertation.

4.3. Composite Approach

Two approaches were used for fabricating polymer scintillation films: the composite approach and the homogeneous approach. The composite approach involved the fabrication of composite films comprising phase-separated polymer/lithium salt mixtures by solution-casting methods. Films were fabricated by mixing an appropriate polymer, lithium salt, and fluor(s) with

Table 5. Properties of Selected Lithium-6 Salts.

Salt	*Molar Mass (g/mol)*[a]	*Density (g/cm^3)*[a]	*wt% ^6Li*[a]	*Atom Density ^6Li ($atoms/cm^3$)*[a]	*Hygroscopic?*	*Thermally stable?*[b]
Li_2CO_3	72.074	2.058	8.376	3.439×10^{22}	No	Yes
$LiNO_3$	68.044	2.349	8.872	2.079×10^{22}	Yes	Yes
Li_2O	28.074	1.891	43.008	4.057×10^{22}	Decomp	Yes
LiF	25.035	2.543	24.114	6.117×10^{22}	No	Yes
LiCl	41.49	2.024	14.550	2.938×10^{22}	Yes	Yes
Li_3PO_4	113.09	2.478	16.015	3.958×10^{22}	No	Yes
$Li_2B_4O_7$	167.32	2.375	7.216	1.709×10^{22}	No	Yes
Lithium phenylboronate	144.98	---[c]	4.164	---[c]	No	No
Lithium benzoate	121.12	1.18	4.984	5.867×10^{21}	Yes	No
LiSal	138.12	0.500	4.371	2.180×10^{21}	Yes	Yes
Lithium 4-methyl salicylate	159.20	---[c]	3.792	---[c]	Yes	No
$LiClO_4$	105.49	2.399	5.723	1.370×10^{22}	Yes	Yes
LiI	132.94	4.048	4.541	1.834×10^{22}	Yes	Yes
$LiBF_4$	92.84	0.844	6.503	5.473×10^{21}	Yes	Yes

[a]These values have been adjusted to reflect 97.6% enrichment in ^6Li.

[b]Thermal stability indicates that the neat salt will not decompose when heated in air to 120°C.

[c]Areas without entries are values that were not located in the literature and were not measured.

Acknowledgement: Dr. Indraneel Sen for partial compilation of this data.

a common solvent then pipetting the resulting solution onto a suitable substrate, 2” in diameter, on a level surface. The cast solution was covered with an inverted beaker and the solvent was evaporated overnight to form a film which was then baked to constant mass under nitrogen at a temperature below both the boiling point of the solvent and the decomposition temperatures of the components. There is an inherent error in this solution casting method in that a small amount of the polymer solution remains in the original container and does not become incorporated into the final film. This systematic error did not affect the compositions of the final films; however, it did result in small errors in the calculated thicknesses due to a reduced quantity of material in the final film. It was not possible to eliminate this source of error by weighing the final film because many polymers retain a small amount of residual solvent in the resulting film even after baking to constant weight. In order to simplify the casting procedure and to improve reproducibility, all solutions were cast as 5% by mass of film components to solvent, the film thicknesses were calculated from the algebraic sum of the individual volumes of each of the components assuming that the material transfer was quantitative, and residual solvent and free-volume effects were ignored.

The primary polymer used in the composite approach was polystyrene (PS). This polymer was chosen because it is air-stable, it has robust mechanical integrity, the photophysics have been extensively investigated by other researchers, and it is relatively simple to synthesize. PS was synthesized by conventional bulk free radical polymerization. Though this synthesis technique introduces additional structural defects as compared to solution polymerization, it was selected because it is the most common method by which polymer scintillators are fabricated. Free radical initiator 2,2’-azobisisobutyronitrile (AIBN) was purified by recrystallization from methanol. Styrene was purified by passing the monomer through a column containing basic

alumina immediately before use.[90] Purified AIBN was dissolved in the purified monomer (6 mg AIBN per 1 mL monomer) in a 25 mL glass vial. The vial was sealed with a cap containing a septum, then the solution was degassed by three freeze-pump-thaw cycles and finally refilled to ambient pressure with argon.

For samples thinner than 1 mm, the degassed solution was suspended in a preheated oil bath at 60°C and polymerized for 48 hours. The resulting polymer was purified by dissolving in tetrahydrofuran (THF) at 15 mL/g and precipitating into a six-fold excess of methanol. All THF and diethyl ether solvents used in this project were purified by fractional distillation from anhydrous calcium chloride to remove water and butylated hydroxytoluene (BHT) stabilizer, the presence of both of which were determined to have deleterious effects on scintillation responses. The resulting purified PS was collected by vacuum filtration, washed with fresh methanol, and dried in a vacuum oven at 100 Torr, 95°C, over P_2O_5, and in a nitrogen atmosphere to a constant mass. Purification was repeated until the ^{1}H NMR (nuclear magnetic resonance) resonances corresponding to the vinyl groups of residual styrene were eliminated. The molecular weight of the resulting polymer was determined by gel permeation chromatography against PS standards. To fabricate films, an appropriate mass of polymer, lithium salt, and fluor were dissolved in purified THF to make a 5% by mass solution, then cast onto a 2" diameter ultraviolet transmission (UVT) grade crosslinked acrylic disk obtained from Eljen Technologies (industrially labeled as UVT Acrylic). The cast solution was covered with a beaker to increase the vapor pressure of THF above the film surface to promote uniform drying, to prevent crazing of the film due to drafts in the laboratory, and to reduce dust contamination. The THF was evaporated for 24 hours under ambient conditions, then the resulting films were dried to constant mass at 60°C over P_2O_5 with continuously flowing nitrogen to reduce the amount of residual

solvent remaining in the film. Films were characterized without removal from the acrylic disks to prevent crazing from removal from the substrate, to improve the mechanical integrity of the resulting film, to facilitate optical coupling with the PMT, and to prevent direct contact of the polymer film with the optical grease used for PMT coupling. [91]

Two fluors were used simultaneously in the PS-based films. The primary fluor was selected to be PPO because its excitation spectrum overlaps well with the emission spectrum from polystyrene which results in efficient transfer of excitation energy and because it has a quantum yield for fluorescence of 100%.[41] The fluorescence emission spectrum of PPO is in the region 340 – 390 nm which is not in the optimum PMT spectral sensitivity region. Thus, a secondary wavelength shifting fluor, POPOP, was used to shift the wavelength of emission to match the PMT spectral sensitivity region. POPOP was selected as the wavelength shifter because it can be implemented at relatively high temperatures without decomposition, its excitation spectrum overlaps well with the emission spectrum from PPO, and it has a quantum yield for fluorescence of 93%.[41] To eliminate variations in the relative amounts of PPO and POPOP among films, a preblended fluor mixture comprising 97.13% PPO and 2.87% POPOP, referred to herein as PPO/POPOP, obtained from Curtiss Laboratories was used. More details regarding this fluor mixture will be given in section 5.3.2. of this work.

4.4. Homogeneous Approach

A drawback of scintillation films that are fabricated by the composite approach is that many organic polymer/lithium salt composites undergo phase-separation and do not result in homogeneous composites. This results in a decrease in the optical transparency of the final material. Scintillation light generated inside a film must be able to escape the film in order to be

detected. Transparent materials have improved optical transmission as compared to opaque materials, so the fabrication of transparent lithiated polymer scintillation films was pursued in this work. This was accomplished by providing bonds between lithium ions and the polymer chains to result in optically homogeneous materials. This strategy is referred to herein as the homogeneous approach. Three principal polymers were synthesized for this purpose and the synthesis of each is discussed in the following sections.

4.4.1. Poly(styrene-*co*-lithium maleate)

The first lithiated polymer that was investigated was poly(styrene-*co*-lithium maleate), abbreviated as PS-*co*-PLiMAn. Styrene was selected because it is relatively inexpensive, it is easy to purify and polymerize, and it contains aromatic pendant groups which facilitate scintillation. It has been demonstrated that in free-radical-initiated solution polymerization, the copolymerization of styrene and maleic anhydride results in an alternating copolymer.[92,93] The maleic anhydride groups can be hydrolyzed to generate two acid groups per monomer unit, each of which can be titrated to form a dilithium salt of each repeat unit. This permits a maximum loading of ^{6}Li of 5.24% by mass if all the hydrolyzed anhydride groups are neutralized. The alternating nature of this copolymer ensures that the sizes of the phases are approximately of molecular size and will therefore cause negligible scattering of scintillation light. PS-*co*-PLiMAn is insoluble in common organic solvents which precludes its use with common fluors used in polymer scintillators. It is however soluble in water, permitting the use of salicylic acid (HSal) as a fluor.[94]

The protocol used to synthesize PS-*co*-PMAn is illustrated in Figure 4 in which the copolymer is labeled as compound **1a**. Styrene and AIBN were purified as previously described. Maleic anhydride (MAn) was used as received. MAn (4.168 g, 42.5 mmol), 35 mL anhydrous

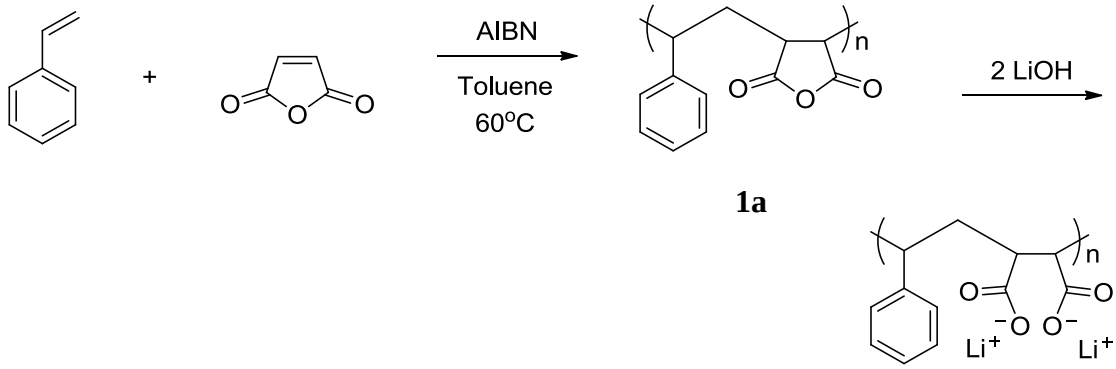


Figure 4. Synthesis of PS-*co*-PMAn and PS-*co*-PLiMAn.

Styrene and maleic anhydride were copolymerized to form PS-*co*-PMAn, then the maleic anhydride groups were hydrolyzed and titrated with ^{6}LiOH to form the lithiated copolymer.

toluene, 5 mL anhydrous diethyl ether, and a magnetic stir bar were added to a flame-dried round bottom flask and sealed with a rubber septum. When the MAn dissolved, the diethyl ether was removed by vacuum then styrene (4.426 g, 42.5 mmol) and purified AIBN (36.6 mg, 0.223 mmol) were added. The solution was degassed by three freeze-pump-thaw cycles to remove dissolved oxygen, then the flask was suspended in an oil bath at 60°C with magnetic stirring. The polymerization was carried out for 45 minutes, during which time the copolymer precipitated from the solution. The white precipitate was collected by filtration and washed with toluene and diethyl ether, then dissolved in THF and precipitated by dropwise addition into diethyl ether to remove unreacted monomers, initiator, and homopolymers. The amount of byproducts removed by the purification was monitored by evaporating the diethyl ether filtrate and measuring the mass of the remaining residue. The purification process was repeated until the amount of byproducts removed by additional purification steps became negligible. The resulting copolymer was collected by vacuum filtration and dried to a constant weight at 100 Torr, 95°C, over P_2O_5 in a nitrogen atmosphere.

To lithiate the copolymer, a mass of 409.6 mg PS-*co*-PMAn was dissolved in 8 mL THF. In a separate container, an appropriate mass of ^{6}LiOH was dissolved in 13 mL H_2O and heated to 90°C with stirring. The copolymer solution was added to the ^{6}LiOH solution dropwise. The solution was stirred at 90°C for one hour to permit completion of the hydrolysis reaction and evaporation of the THF. The solution was then cooled to 40°C, then an appropriate mass of salicylic acid (HSal) was added to function as the fluor. This solution was stirred for one hour at 40°C to ensure complete dissolution of the HSal. The clear viscous solution was pipetted onto a suitable substrate, covered with an inverted beaker, then dried to a constant mass.

4.4.2. Poly[styrene-*co*-lithium maleate-*co*-2-phenyl-5-(4-vinylphenyl)oxazole]

The polymer PS-*co*-PLiMAn is insoluble in common organic solvents, precluding its use with common fluors used for scintillation. Additionally, the quantum efficiency of salicylic acid is not optimum for scintillation, resulting in low overall light yields. To circumvent these issues, it was thought to synthesize a polymerizable analog of a fluor and copolymerize it with styrene and MAn. It was first hypothesized that a methacrylate-functionalized fluor could be synthesized fairly easily using methacryloyl chloride and a hydroxyl-functionalized fluor. However, preliminary experiments attempting to copolymerize styrene, maleic anhydride, and methyl methacrylate produced only PS-*co*-PMAn. It was suspected that the very fast reaction of styrene with maleic anhydride and the polar nature of maleic anhydride and the methacrylate unit precluded the propensity for methyl methacrylate to be incorporated into the backbone. Reports in the literature indicate that the terpolymerization should be possible;[95,96] however, the results could not be replicated. It was then hypothesized that a better option would be to implement a vinyl-substituted form of a fluor. In order to directly compare results to PS films, a vinyl-substituted form of PPO, 2-phenyl-5-(4-vinylphenyl)oxazole (VPPO), was chosen as the polymerizable fluor. VPPO is not commercially available and had to be synthesized in the laboratory. The synthetic strategy is illustrated in Figure 5. Several independent reports of this synthesis were located in the literature; however, it was not possible to complete the synthesis using any single report. Rather, the synthesis was conducted by testing all the reaction conditions in each report until the reproducible results were obtained. NMR data for the intermediates were not present in the literature so the identity and purity of the product obtained after each step was determined by measuring the melting point and comparing to multiple literature values. The exact protocol used to synthesize VPPO is detailed in the following discussion. The synthetic

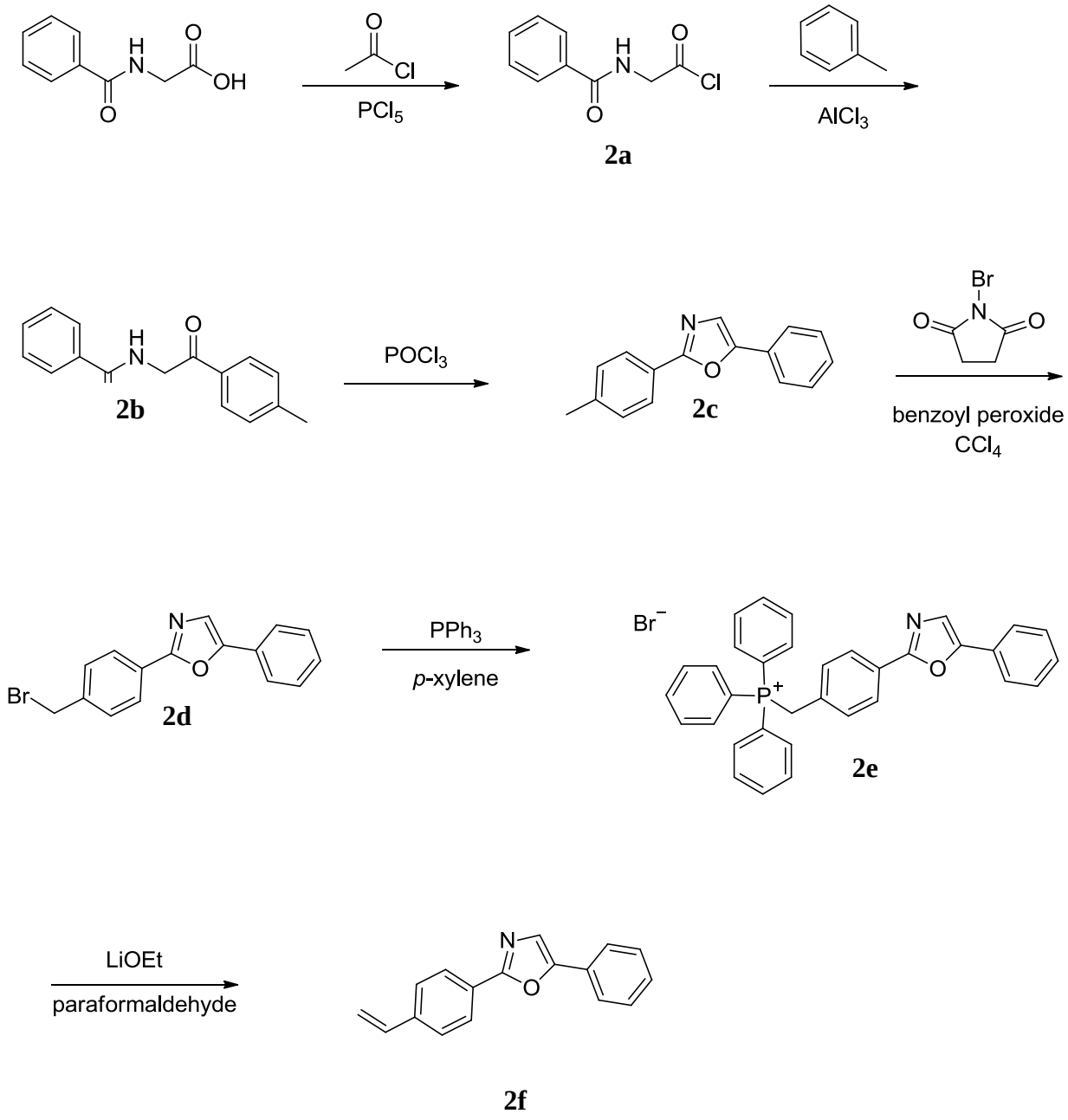


Figure 5. Synthesis of VPPO.

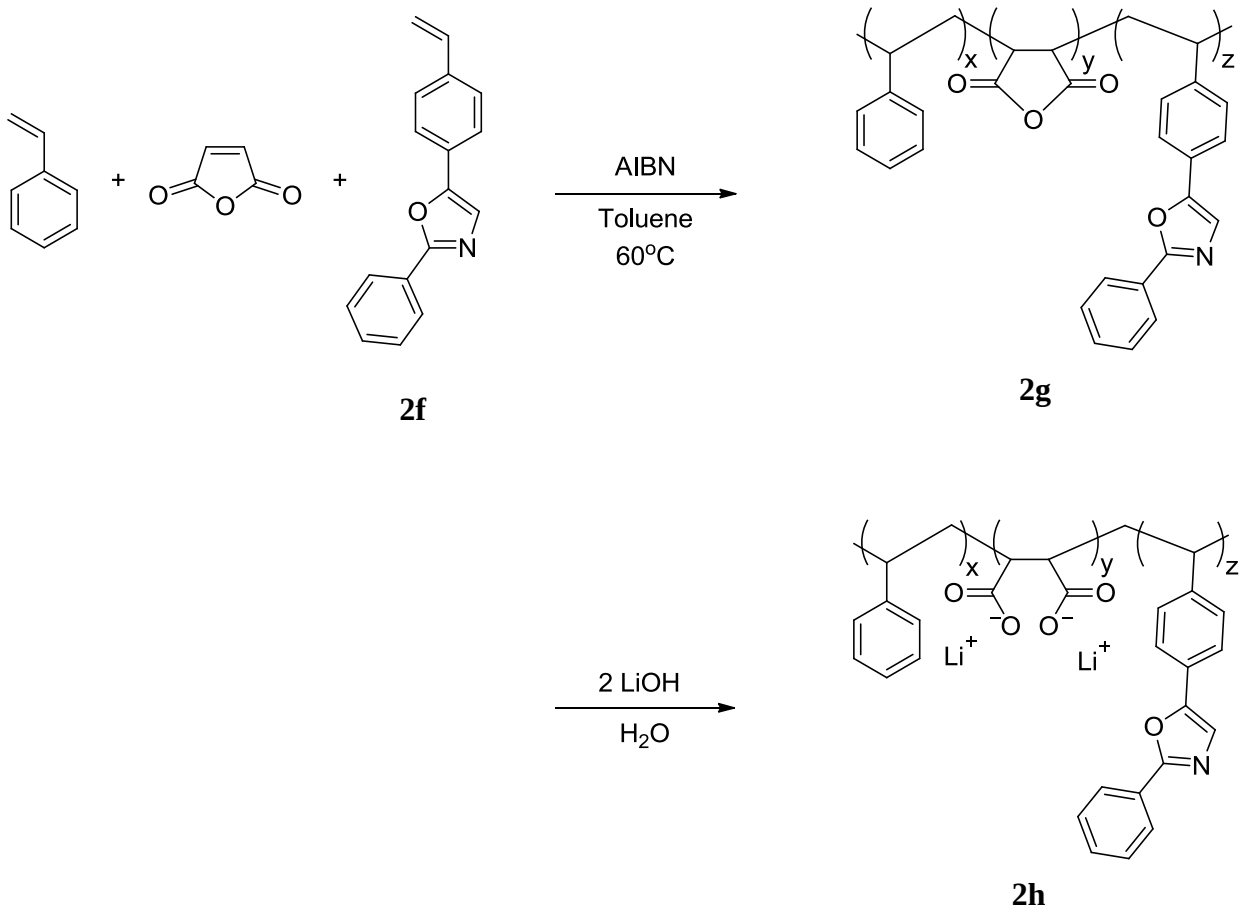
strategy implemented for the terpolymer was similar to that for PS-*co*-PLiMAn. It was intended to synthesize VPPO (**2f**) copolymerize it with styrene and MAn to form poly[styrene-*co*-maleic anhydride-*co*-2-phenyl-5-(4-vinylphenyl)oxazole] (labeled as PS-*co*-PMAn-*co*-PVPPO, **2g**), then to hydrolyze the maleic anhydride groups and titrate with ^{6}LiOH to form poly[styrene-*co*-lithium maleate-*co*-2-phenyl-5-(4-vinylphenyl)oxazole] (labeled as PS-*co*-PLiMAn-*co*-PVPPO, **2h**), as shown in Figure 6.

Synthesis of hippuryl chloride (**2a**)[72,97]

To a 500 mL flame-dried Erlenmeyer flask containing a magnetic stir bar, the following contents were added in this order: 250 mL (3.51 mol) acetyl chloride, 35.3 g (169.5 mmol) crushed phosphorus pentachloride, and 25.0679 g (139.9 mmol) hippuric acid. The mixture was covered with a rubber stopper and stirred for 30 minutes, periodically removing the stopper to release evolved HCl. After 30 minutes, a yellow precipitate formed which was collected by vacuum filtration, washed with acetyl chloride then anhydrous diethyl ether, and dried in a vacuum over P_2O_5 for 1 hour. The resulting product had a single melting point at 124°C with decomposition (lit. 125°C) indicating adequate purity for further use. A mass of 12.7156 g of **2a** was collected to give a 46.0% recovery.

Step 2: Synthesis of benzoyl aminomethyl *p*-tolyl ketone (**2b**)[72,97-99]

To a flame-dried 250 mL round bottom flask containing a magnetic stir bar, the following materials were added: 12.7156 g (64.3 mmol) **2a**, 125 mL (1.18 mol) dry toluene, 19.12 g (143.4 mmol) crushed anhydrous $AlCl_3$. The flask was quickly stoppered and purged with argon. The



2f **2g** **2h**

Figure 6. Synthesis of PS-*co*-PMAn-*co*-PVPPO and PS-*co*-PLiMAn-*co*-PVPPO.

The notations x, y, and z are the molar ratios of styrene, MAn, and VPPO in the terpolymer, respectively.

solution was heated to 60°C for 4 hours with stirring. After approximately 30 minutes, the solution became black. After 4 hours, the flask was cooled to room temperature, then the contents were poured into an HCl-ice bath and stirred for 30 minutes to quench the reaction. The product was then collected by vacuum filtration, washed with warm water and *n*-hexane, then dried in a vacuum overnight over P_2O_5. Recrystallization from absolute ethanol gave benzoyl aminomethyl-*p*-tolyl ketone. The identity of the product was confirmed by ^{1}H NMR analysis. The product had a single melting point at 116 – 118°C (lit. 114 – 116°C). A mass of 4.3687 g (17.2 mmol) of **2b** was collected for a 26.8% recovery.

Step 3: Synthesis of 2-phenyl-5-(*p*-tolyl)oxazole (**2c**)[72,97-99]

A 100 mL round bottom flask was flame-dried, then a stir bar was added and the flask was placed in the drying oven at 110°C overnight. The flask was removed and cooled, then 4.3687 g (17.2 mmol) **2b** was added, followed by 50 mL (536 mmol) phosphoryl chloride. The flask was flushed with argon and a reflux condenser was attached. The flask was suspended in an oil bath at 140°C and refluxed for 5 hours. The reaction was then cooled to room temperature, the contents poured into ice water, and the precipitate collected by vacuum filtration. The precipitate was dissolved in ethanol and reprecipitated into water and the white product was collected by vacuum filtration and dried overnight in a vacuum. The identity of the product was confirmed by ^{1}H NMR analysis. The melting point was 75°C (lit. 81 – 82°C). The lower value obtained for the melting point was attributed to the presence of side products. However, the supposed side products could not be found using thin layer chromatography and attempts to remove the side products by column chromatography did not result in a change in the melting

point. It was thus decided to continue to the next step with the impurities in the product. A mass of 3.7238 g (15.8 mmol) of **2c** was collected for a 91.8% recovery.

Step 4: Synthesis of 2-(4-(bromomethyl)phenyl)-5-phenyloxazole (**2d**)[97,100]

To a flame-dried 100 mL round bottom flask, the following materials were added: 3.7238 g (15.8 mmol) **2c**, 2.8677 g (16.1 mmol) N-bromosuccinimide, 102.4 mg (0.423 mmol) benzoyl peroxide, and 52 ml CCl_4. A reflux condenser was attached and flushed with argon. The flask was suspended in an oil bath and refluxed for 15 minutes. The solution was filtered to remove succinimide, then the filtrate was extracted two times with 20 mL water to remove bromine and peroxides. The organic layer was collected and dried over anhydrous sodium sulfate and filtered. The filtrate was collected and the solvent was removed under reduced pressure. The mass of **2d** collected indicated quantitative yield; however, the product was immediately subjected to the next reaction without collection or characterization to prevent decomposition.

Step 5: Synthesis of triphenyl(4-(5-phenyloxazol-2-yl)-benzyl) phosphonium bromide (**2e**)[72,97,100]

In the same round bottom flask containing **2d**, 5.1864 g (19.8 mmol) triphenylphosphine and 80 mL anhydrous DMF (N,N-dimethylformamide) were added. A reflux condenser was attached and flushed with argon, then the flask was submerged in an oil bath at 170°C. The reaction proceeded for 3 hours, then was removed from heat. The DMF was removed under reduced pressure, then the crude product was dissolved in ethanol and precipitated into anhydrous diethyl ether. The precipitate was collected by centrifugation, then recrystallized from boiling water. The crystalline product was collected by vacuum filtration and dried overnight in a

vacuum oven over P_2O_5. The product had a single melting point of 292°C (lit. 284 – 286°C). A mass of 3.4947 g (6.06 mmol) of **2e** was collected for a 38.4% recovery.

Step 6: Synthesis of 5-phenyl-2-(4-vinylphenyl)oxazole (VPPO) (**2f**)[72,97]

To a flame-dried round bottom flask, 3.4947 g (6.06 mmol) triphenyl(4-(5-phenyloxazol-2-yl)-benzyl)phosphonium bromide, 218.3 mg (6.06 mmol) *p*-formaldehyde, 315.4 mg (6.06 mmol) lithium ethoxide, and 30 mL dry ethanol were added. The reaction vessel was sealed and the solution was stirred at room temperature for 1 hour. The solution was then poured into 50 mL cold water and stirred for 40 minutes. The crude product was collected by vacuum filtration, then purified by column chromatography on Al_2O_3 using toluene as the eluent. The toluene was then removed under reduced pressure at room temperature to give the pure polymerizable monomer, VPPO. The melting point of the product was 64 – 65°C (lit. 65 – 66°C), indicating the correct product was obtained from the chromatography purification. A mass of 0.587 g (2.37 mmol) of **2f** was collected for a 39.1% recovery. The entire synthesis of **2f** occurred with a 1.70% recovery.

To synthesize PS-*co*-PMAn-*co*-PVPPO (**2g**) , a mass of 1.0577 g (10.8 mmol) MAn was dissolved in 28 mL anhydrous toluene and 5 mL anhydrous diethyl ether in a flame-dried round bottom flask containing a magnetic stir bar. After dissolution, the diethyl ether was removed with a vacuum. A mass of 0.67 g (6.43 mmol) styrene, 0.294 g (1.19 mmol) VPPO, and 6.7 mg (0.041 mmol) AIBN were added to the solution and the flask was sealed with a rubber stopper. The flask was degassed by three freeze-pump-thaw cycles, then suspended in an oil bath at 60°C to polymerize. After 1 hour, the reaction was stopped and the precipitated polymer was collected by

vacuum filtration, washed with toluene and diethyl ether, and dried to constant weight. A mass of 1.6531 g of the terpolymer was collected.

To synthesize PS-*co*-PLiMAn-*co*-PVPPO (**2h**), the neat terpolymer PS-*co*-PMAn-*co*-PVPPO was dissolved in DMF. In a separate container an appropriate mass of ^{6}LiOH was dissolved in water and heated to 90°C. The lithium solution was added to the polymer solution dropwise. After much of the water had evaporated , the polymer solution was pipetted onto a suitable substrate and covered with a beaker. The solvent was evaporated at 75°C overnight, then the film was dried to constant weight.

4.4.3. Poly(styrene-*co*-lithium 4-vinylbenzoate)

The strategy used to synthesize poly(styrene-*co*-lithium 4-vinylbenzoate), labeled as PS-*co*-PLi4VB), is illustrated in Figure 7 where it is labeled as compound **3b**. Precursor 4-vinylbenzoic acid (4VBA) was purified by recrystallizing from water. An aqueous solution of purified 4-vinylbenzoic acid (4VBA) was titrated with ^{6}LiOH at room temperature in a round bottom flask, then the water was quantitatively removed under reduced pressure at 35°C to synthesize lithium 4-vinylbenzoate (Li4VB, **3a**). The Li4VB was dissolved in DMF, then appropriate masses of styrene and AIBN were added. The flask was sealed with a rubber stopper and the solution was degassed by three freeze-pump-thaw cycles. The monomer solution was then suspended in an oil bath at 80°C to polymerize. The copolymer was collected by vacuum filtration and dried to a constant weight.

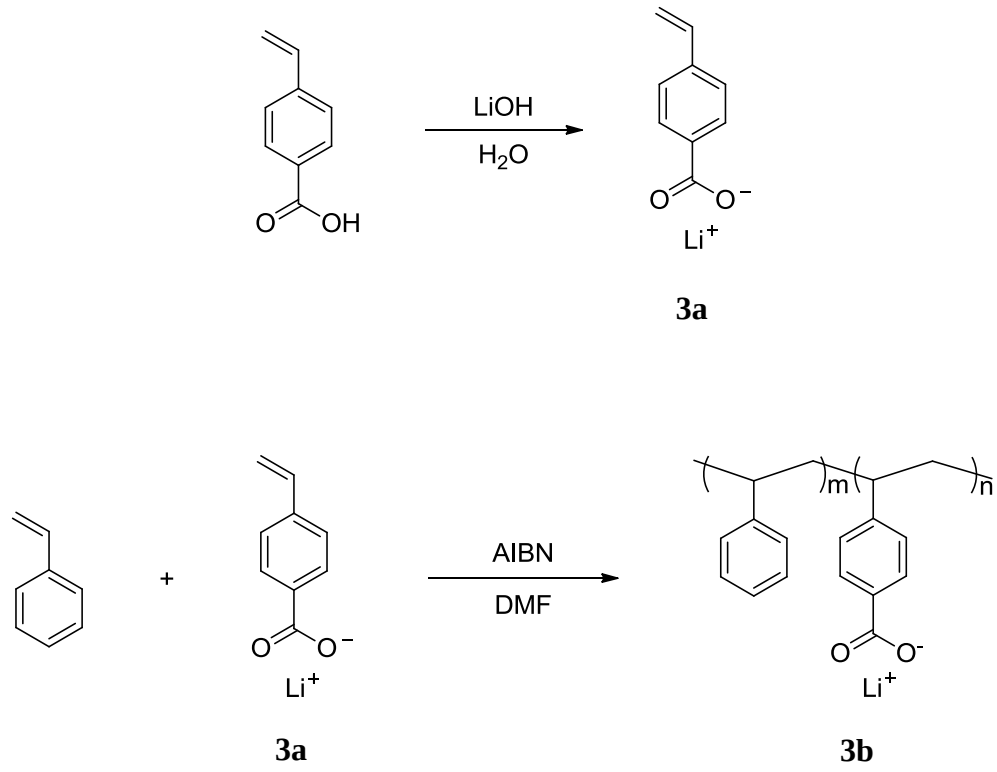


Figure 7. Synthesis of Li4VB and PS-*co*-PLi4VB.

Subscripts *m* and *n* represent the mole fractions of styrene and Li4VB in the copolymer, respectively.

4.5. Characterization Methods

4.5.1. Particle Distribution and Morphology

The particle distributions and morphologies in the interior volume of the composite films were examined by confocal laser-scanning microscope (CLSM) equipped with a 488 nm argon ion laser.

4.5.2. Optical Properties

The optical clarity of each of the films was measured using UV-visible spectroscopy. The instrument response was corrected for the wavelength variation in lamp intensity and detector quantum efficiency. The optical transmission was measured and the wavelength at which the transmission abruptly drops to zero (cutoff wavelength) was determined.

Fluorescence measurements were conducted in reflectance mode. Corrections were made for the wavelength variation in lamp intensity and detector quantum efficiency. The excitation and emission spectra were measured first for the neat polymer, then for the polymer containing various amounts of added fluors. Common PMTs used in scintillation counting have a very low sensitivity in the wavelength region of fluorescence emission of common aryl vinyl polymers such as PS. [91] Thus, any photons that are emitted by the polymer matrix are not detected. To ensure that no light was lost as photon emission from the polymer matrix, excitation spectra were measured with the emission detector held at the wavelength of maximum emission of the neat polymer, then for the polymer containing various amounts of fluors and lithium. The integrated area of the resulting excitation spectra should be proportional to the number of photons emitted by the polymer matrix. The fluor concentration was increased until the number of photons emitted in the region of polymer emission in response to excitation of the polymer became

negligible. The total fluorescence emission yields were then determined by exciting the polymer matrix and measuring the emission from the fluor. Relative emission responses were obtained by integrating over the wavelength range of fluor emission. The concentration of the fluor was increased until no further increase in emission intensity occurred. The concentration at which no emission from the polymer occurred and the concentration at which the fluorescence output from the fluor was at a maximum were compared.

4.5.3. Electronics Used in Scintillation Characterizations

The light pulses from the samples were converted into electrical pulses using the instrumentation shown in Figure 8. Samples cast on acrylic disks were coupled with Saint Gobain BC-630 optical grease to a Philips XP2202B 10-stage PMT mounted on a Canberra 2007P base (preamplifier). The voltage across the PMT was supplied by an Ortec 556 high-voltage power supply and was maintained at 1200 V (volts). The signal from the preamplifier was fed into an Ortec 572A amplifier with a 2 μs shaping time. The amplified signal was digitalized using an ORTEC 926 multichannel buffer (MCB) with an 8192 channel analog-to-digital converter (ADC). The digitalized output was then saved using the MAESTRO-32 software from ORTEC.[101] Electronic noise was reduced by setting a lower level discriminator (LLD). Pulses that occur below the LLD are not registered by the electronics.[101]

4.5.4. Calculation of Light Yields

Energetic charged particles are completely stopped in condensed matter in a timescale on the order of picoseconds[10] whereas the timescale for fluorescence by organic molecules occurs by exponential decay and is on the order of nanoseconds.[41] All the excitations that are to be generated by a charged particle are generated in a time frame much shorter than the characteristic

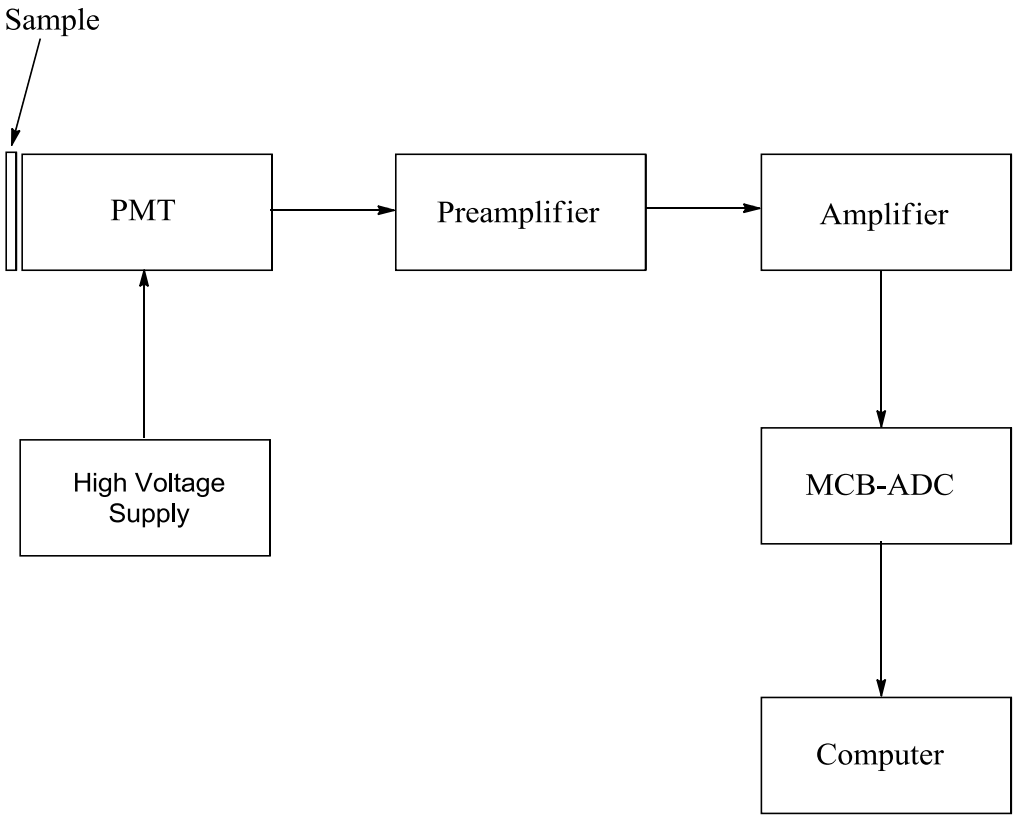


Figure 8. Schematic of Instrumentation Used to Measure Scintillation Responses.

Adapted from Urffer.[102]

spread in the time distribution for fluorescence emission. Thus, the time required for scintillation to occur is very similar to the fluorescence decay time and all the scintillation photons generated in response to a single charged particle occur as a single flash of light. Some of the photons in this light flash are incident on the cathode of the PMT which generates an electrical pulse with an amplitude proportional to the number of photons striking the cathode. The electronics group the pulses into bins, called channels, based on pulse amplitude. Thus, the channel at which a pulse, or count, occurs is linearly related to the number of photons that strike the cathode of the PMT per scintillation event (with proper settings). This permits calibration of the light yields by measuring a reference scintillator with a known light yield and determining the channel corresponding to a specific spectral feature. [91] Determination of light yields for different types of impinging radiations required the determination of three spectral features. Spectral peaks were calculated by finding the channel at which the largest count rate occurred on a plot of count rate against channel. Spectral averages were calculated using Equation 19,

$$\langle x \rangle = \frac{\int_0^\infty x f(x)\,dx}{\int_0^\infty f(x)\,dx}, \tag{19}$$

where $<x>$ is the channel average of the spectrum, x is channels, and $f(x)$ is the count rate spectrum.

Scintillation light yields were calibrated by using the responses from GS20 lithiated glass which emits an average of approximately 6,250 photons per thermal neutron capture event.[11,102,103] A calibration factor was obtained by dividing the light yield by the average value of the neutron response spectrum (Equation 19), as shown in Equation 20 in which the units are

listed in parentheses. The calibration factor can be used to convert each channel to the number of photons the scintillator emitted to register a count at that channel. Due to variations in the instrumentation over time, this calibration was performed each time a sample was measured. It should be noted that no attempt was made to correct the calculated light yields for the relative spectral sensitivities of the PMT for GS20 emission and sample emission. It is estimated that this would result in a change in the calculated light yields of less than 5% for the materials measured.

$$Calibration\ factor\left(\frac{photons}{channel}\right) = \frac{GS20\,LY\left(\frac{photons}{neutron}\right)}{GS20\,neutron\ peak\ channel\left(\frac{channels}{neutron}\right)} \tag{20}$$

4.5.5. Radiation Sources

The radiation sources used to characterize the scintillation responses are listed in Table 6. Activities are listed in units of Curies (Ci) where 1 Ci = 3.7×10^{10} disintegrations/second. The alpha responses were measured with a 0.1 μCi ^{241}Am source and the beta responses were measured with a 0.1 μCi ^{36}Cl source. Thermal neutron characterizations were performed using a ^{252}Cf source contained within a custom-built irradiator, which is described in further detail in the following section. For gamma-ray characterizations, several 1μCi ^{60}Co button sources were used as well as a 95.79 μCi ^{60}Co source housed in a custom built gamma-ray irradiator, which is described in further detail in section 4.5.7. Two gamma-ray energies are listed for ^{60}Co because it emits two photons per disintegration.

Table 6. Radiation Sources Used for Scintillation Characterizations

Source	*Type*	*Energy*	*Half Life*	*Initial Date*[101]	*Initial Activity*
^{241}Am	Alpha	5.484 MeV	432.6 yr	April 1, 1993	0.1 μCi
^{36}Cl	Beta	0.710 MeV	3.08 x 10^5 yr	July 1, 2010	0.1062 μCi
^{60}Co	Gamma-ray	1.17, 1.33 MeV	5.27 yr	January 1, 2012	95.79 μCi
^{60}Co	Gamma-ray	1.17, 1.33 MeV	5.27 yr	Various	1 μCi
^{252}Cf	Neutron	*	2.64 yr	July 2, 2009	2.314×10^6 n/(μg · s)**

*Neutrons are emitted over a range of energies from spontaneous fission of ^{252}Cf.

**Rate of neutron emission per μg ^{252}Cf. The initial mass of the ^{252}Cf was 0.59 μg.

4.5.6. Neutron Irradiator

Characterization of scintillation responses to thermal neutrons was accomplished using a custom-build neutron irradiator containing 0.59 μg of ^{252}Cf (as of July 2, 2009), shown in Figure 9. ^{252}Cf decays by both alpha particle emission (96.9% branching ratio) and by spontaneous fission (3.09% branching ratio). Spontaneous fission of ^{252}Cf releases approximately 3.76 neutrons per fission event with the most probable neutron energy being 0.7 MeV and the average neutron energy being 2.1 MeV.[104] A spectrum of gamma-rays accompanies the radioactive decay of ^{252}Cf. The energies of the gamma-rays extend up to approximately 3.88 MeV[104] with the average energy being about 0.87 MeV.[105] ^{252}Cf emits 2.314×10^6 neutrons/(μg · s) and 4.9×10^6 gamma-rays/(μg · s).

The ^{252}Cf source is encased within 0.5 cm of stainless steel and surrounded by 1.25 cm of lead to attenuate some of the gamma-rays. The neutrons are thermalized by 5 cm of high density polyethylene (HDPE). The detectors are measured inside two wells. One well is 1.6 mm acrylic

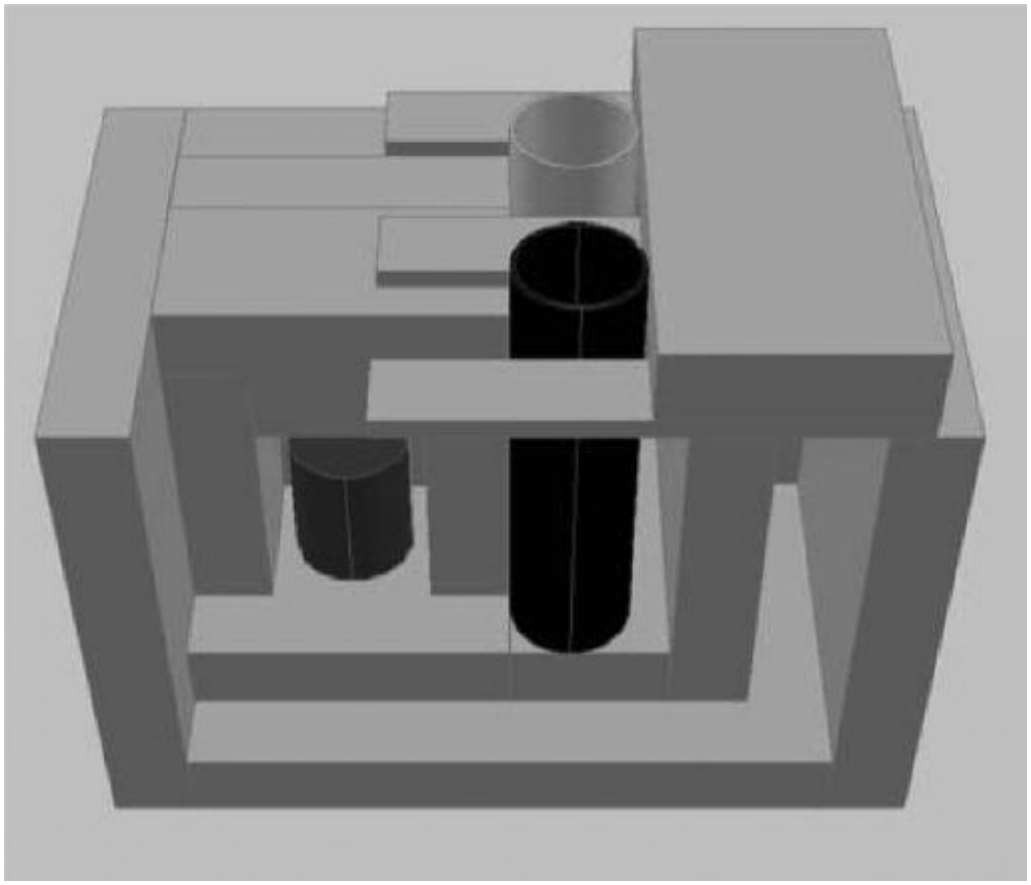


Figure 9. Illustration of the Neutron Irradiator.

The small cylinder on the left represents a 0.59 μg ^{252}Cf source surrounded by 0.5 cm of stainless steel and 1.25 cm of lead. The neutrons are moderated by 5 cm of HDPE. The black cylinder located in the right front represents an acrylic tube 1.6 mm thick wrapped with a 1.6 mm thick sheet of cadmium. The lighter cylinder in the right rear represents an acrylic tube 1.6 mm thick wrapped with 1.6 mm thick sheet of lead. The entire irradiator is housed in 5 cm of HDPE. The front side of the irradiator has been removed in the image for clarity.[102]

surrounded by 1.6 mm cadmium to shield thermal neutrons. The other well is 1.6 mm acrylic surrounded by 1.6 mm lead. First, the detector was measured inside the lead well to obtain the scintillation response to gamma-rays and neutrons of all energies. The detector was then measured inside the cadmium well, which shielded the thermal neutrons. If it is assumed that the number of gamma-rays shielded by the lead and cadmium tubes is similar, then subtracting the response in the cadmium tube from the response in the lead tube results in the thermal neutron response. The neutron fluence in the irradiator was simulated using MCNPX (Monte Carlo for Neutrons and Photons Transport Code) and is shown pictorially in Figure 10.[101] An illustration of the neutron energy spectra through the lead and cadmium tubes as well as the subtracted spectrum is shown in Figure 11.[102]

There is some error associated with the thermal neutron measurement. First, there is a small deviation in the neutron fluence based on the precise location of the detector inside the wells. The other deviation arises due to gamma-rays. Additional gamma-rays are generated in the cadmium tube due to the $^{113}Cd(n,\gamma)^{114}Cd$ capture reaction (reaction probability = 20,600 b). Also, the attenuation of gamma-rays from ^{252}Cf through the lead and cadmium tubes is not identical. The attenuation of energetic photons through a material can be calculated using Equation 21 where I_0 is the initial intensity, I is the attenuated intensity, μ is the attenuation coefficient, and Γ is the thickness.

$$\frac{I}{I_0} = e^{-\mu\Gamma} \tag{21}$$

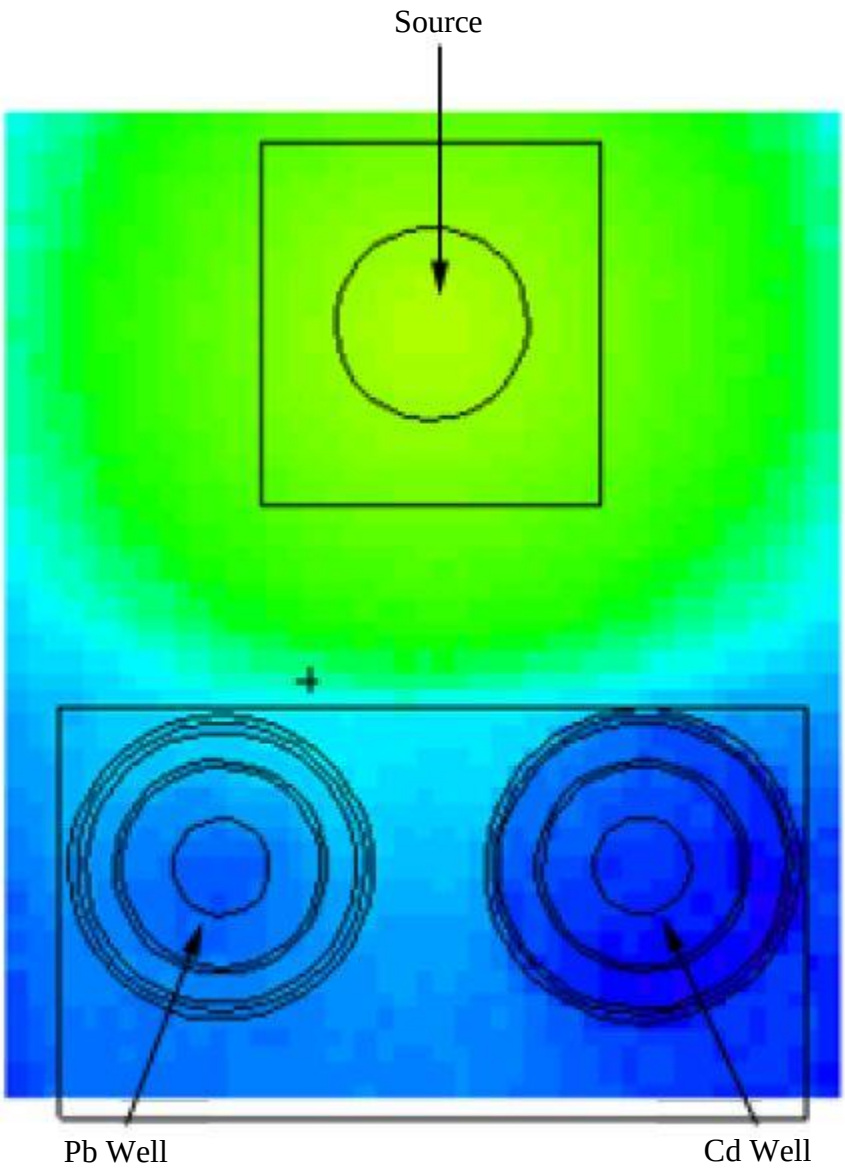


Figure 10. MCNPX Simulation of the Neutron Fluence in the Neutron Irradiator.

Lighter colors (green) indicate higher neutron fluence whereas darker colors (blue) indicate decreased neutron fluence. It can be seen that the neutron fluence is depressed in the cadmium well relative to the lead well. Acknowledgement: Matthew J. Urffer.

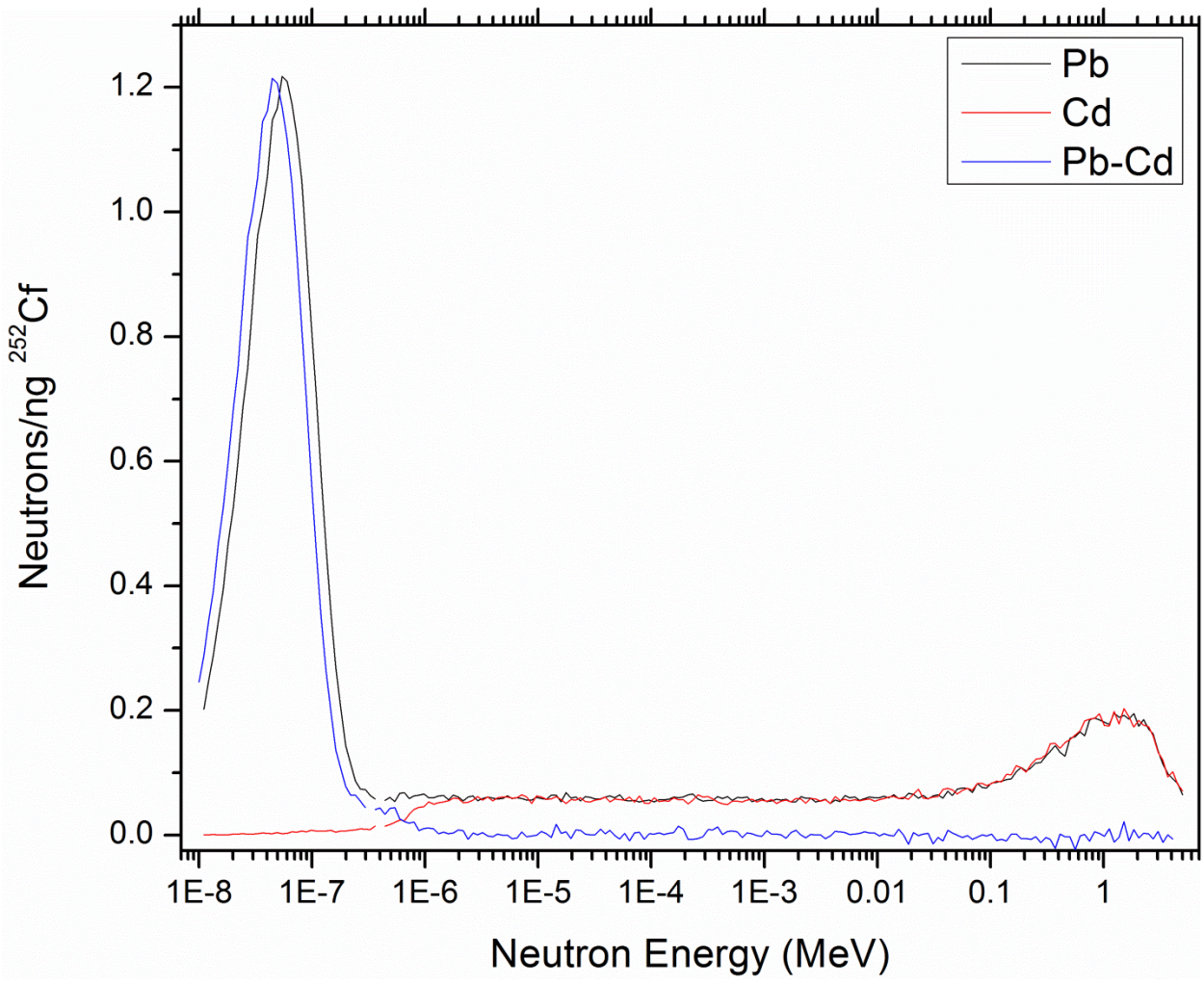


Figure 11. Neutron Fluences Through the Lead and Cadmium Tubes and the Resulting Subtracted Spectrum (Pb – Cd).

These results are from MCNPX simulations of a 1" diameter 2 mm thick GS20 detector.[102] The fraction of neutrons that are less than 1 eV are 67.8% in the Pb tube and 99.9% for the Pb – Cd subtraction. Acknowledgement: Matthew J. Urffer for performing the experiment and calculating the spectrum.

Attenuation coefficients were retrieved from standard reference data sets.[106] These data were used to generate plots to illustrate the difference in gamma-ray attenuation through the lead and cadmium tubes. The plots shown in Figure 12 clearly demonstrate that a greater number of gamma-rays are attenuated by the lead tube than by the cadmium tube.

By considering both the difference between the gamma-ray attenuation through the lead and cadmium tubes and the additional gamma-rays generated from the ^{113}Cd neutron capture reaction, it is evident that the subtraction procedure for obtaining net thermal neutron responses generates error in the data. This error results in neutron count rates that are slightly lower than the actual values. Thus, all values associated with the thermal neutron count rates reported in this dissertation that were generated by the subtraction procedure represent lower limits to the actual thermal neutron detection efficiencies of the detectors described herein.

4.5.7. Gamma-Ray Irradiator

The 95.79 μCi ^{60}Co gamma-ray source is housed inside a custom-built irradiator which is shown in Figure 13. The source is located at the bottom of the irradiator and is encased in 2" steel with a 0.125" thick steel cap. The detector well is a 14" long cylinder that is 0.25" thick with a 4" outer diameter, which is suitable for inserting a detector mounted on a PMT. The detector well is surrounded by lead blocks encased in a steel outer box. A 7 cm thick spacer displaces the detector from the source a total of 10.2 cm such that the exposure at the detector face is 10 mR/hr.[91,101]

The gamma-ray irradiator creates a beam-like geometry of the gamma-rays in the detector well. Gamma-rays incident on the detector surface can either travel directly to the detector surface or can scatter from the walls of the detector well before becoming incident on the detector surface. Scattering results in a decrease in the energy of the gamma-ray. It has been

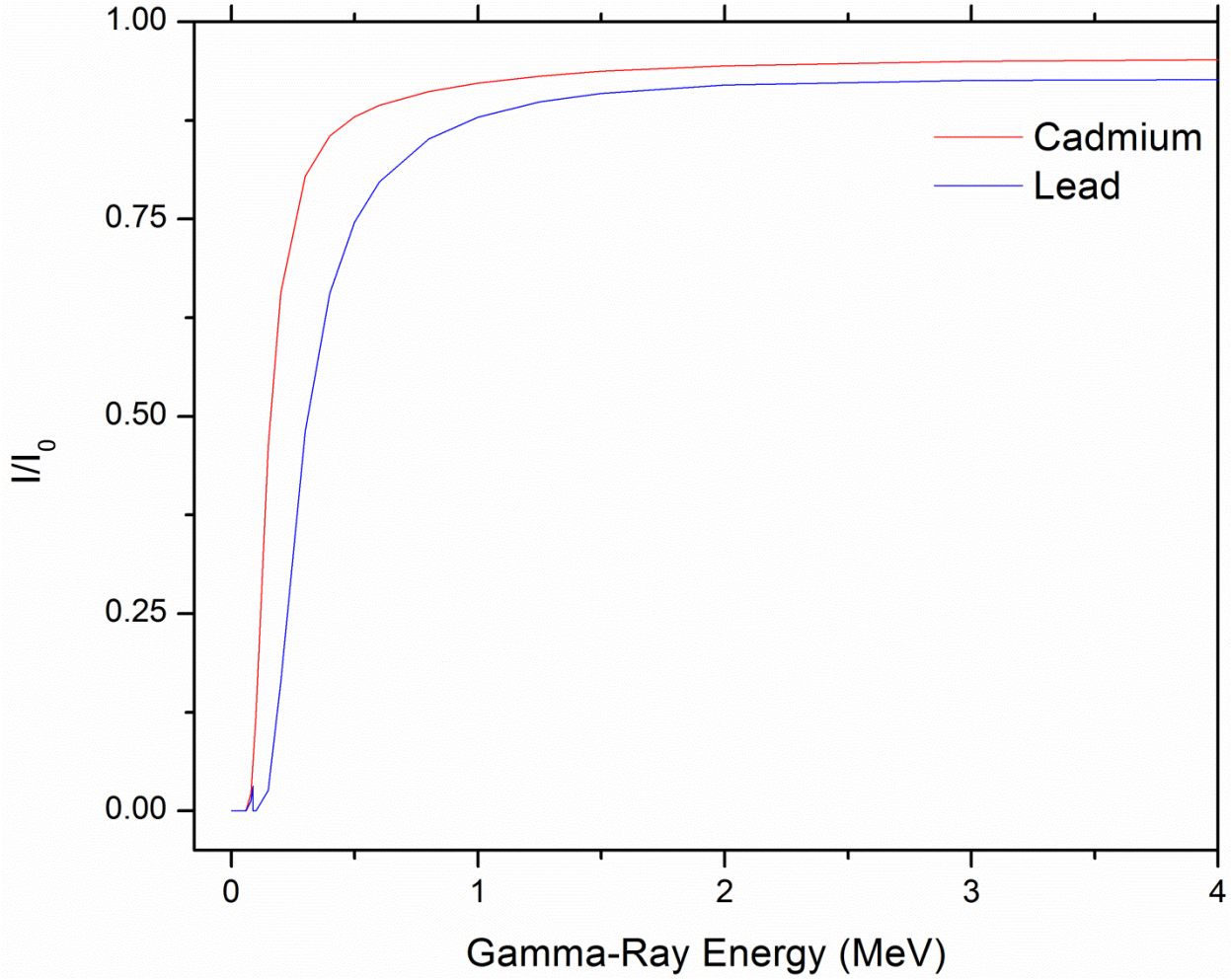


Figure 12. Attenuation of Gamma-Rays Through 1.6 mm Thick Sheets of Lead and Cadmium as a Function of Gamma-Ray Energy.

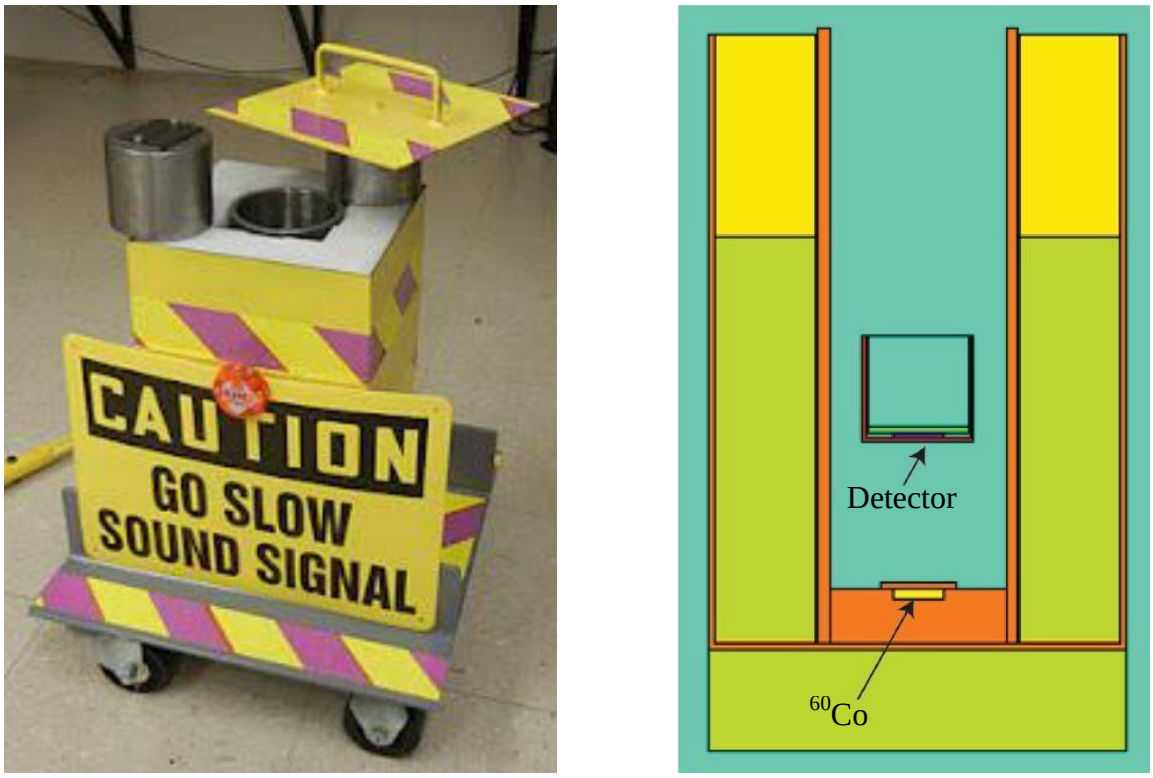


Figure 13. Images of the Gamma-Ray Irradiator.

Left: Image of the gamma-ray irradiator. Right: MCNPX rendering of the gamma-ray irradiator.

Acknowledgement: Matthew J. Urffer.[102]

determined by appropriate modeling that the majority of the gamma-rays that are incident on the detector surface are directly from the source and only a small fraction of the total number of gamma-rays incident on the detector surface have been scattered from the inside of the detector well.[101]

4.5.8. Quantification of Radiation Exposure to Detectors

The intrinsic efficiency (ε_{int}) of a detector can be described qualitatively as a measure of how efficient a detector is at detecting a particular type of radiation. It is more precisely defined as the fraction of particles incident on the detector that result in a count. This relationship is quantified in Equation 22

$$\varepsilon_{int} = \frac{N_c}{N_i} \tag{22}$$

where N_c is the number of counts recorded by the detector and N_i is the number of particles incident on the detector surface. The value for N_c can be determined by counting the detector. The number of particles incident on the detector surface is a function of the source activity (A) and the fraction of emitted particles that are incident on the detector surface (Ω) as described in Equation 23

$$N_i = \Omega A. \tag{23}$$

Radioactive materials decay in a first-order irreversible time-dependent process. After an elapsed time, the activity of a radioactive material is diminished because the amount of material

remaining is decreased. If the source half-life ($t_{1/2}$) is known and the activity (A_0) at some initial time t_0 is known, then the activity (A) after an elapsed time (t) can be calculated using Equation 24

$$A = A_0 e^{-ln2\left(\frac{t}{t_{1/2}}\right)}. \quad (24)$$

The fraction of emitted particles (Ω) that are incident on a detector over a range of thicknesses was modeled using MCNPX. Table 7 shows Ω values in the neutron irradiator for the Pb and Cd tubes as well as for the Pb – Cd subtraction. Table 8 shows Ω values in the gamma-ray irradiator for detectors over the thickness range 25 – 2000 μm. These values for Ω can be used in combination with the source activities to determine the number of particles incident on a detector surface using Equation 23. Values for Ω are given for detectors with radii of 2.54 cm.[101]

4.5.9. Calculation of the Ranges of Heavy Ions

The ranges of alpha particles from ^{241}Am and the ^{6}Li fission products were calculated using the TRIM code (Transport of Ions in Matter) for pure PS, pure ^{6}LiF, and a PS film containing 10% ^{6}LiF.[107] Library definitions for PS (ICRU-226) and LiF (ICRU-185) were implemented with proper adjustments of the LiF data file to account for the 97.6% isotopic enrichment of ^{6}Li. A composite was modeled as a series of alternating PS and ^{6}LiF layers. The thickness of each layer was estimated from the relative volume fractions of PS (V_{PS}) and ^{6}LiF (V_{LiF}) in the composite, which were calculated to be V_{PS} = 0.9474 and V_{LiF} = 0.0526 for a composite containing 10% ^{6}LiF. The layer thicknesses were estimated by multiplying the volume

Table 7. Fraction of Emitted Neutrons that are Incident on a Detector

Detector Thickness (μm)	*Ω (Pb Tube)*	*Ω (Cd Tube)*	*Ω (Pb–Cd)*
25	0.0193826	0.00822766	0.01115494
50	0.0199469	0.00823738	0.01170952
100	0.0198918	0.00823480	0.01165700
150	0.0198313	0.00823681	0.01159449
300	0.0197319	0.00824120	0.01149070
1000	0.0193826	0.00822766	0.01115494
2000	0.0191066	0.00821181	0.01089479

Table 8. Fraction of Emitted Gamma-Rays that are Incident on a Detector

Detector Thickness (μm)	*Ω*
25	0.0357
50	0.0357
100	0.0357
150	0.0357
300	0.0357
1000	0.0358
2000	0.0360

Acknowledgement: Matthew J. Urffer.

fractions by an arbitrary scaling factor of 2 μm to approximate the actual ^{6}LiF particle distribution, resulting in the values of 1.8928 μm for the PS layers and 0.1052 μm for the ^{6}LiF layers. This arrangement is shown pictorially in Figure 14. The incident ions were set to have a 0° angle of incidence on the plane of the layers. Though the ranges converged after simulating approximately 300 ions, the values reported are the average ranges resulting from simulation of 5000 impinging ions in order to converge the energy straggling values. An adequate number of layers were modeled such that every incident ion was stopped by the material.

4.5.10. Detection Efficiency Calculations

The scintillation counting instrumentation outputs raw data as number of counts versus channel number. The number of counts at each channel can be divided by the total count time to obtain a plot of count rate versus channel number, or a count rate spectrum. The total count rate (CR_{total}) is found by integrating the count rate spectrum, $f(x)$, from the LLD to infinity as shown in Equation 25

$$CR_{total} = \int_{LLD}^{\infty} f(x)\,dx\,. \tag{25}$$

The intrinsic efficiency, ε_{int}, is calculated by dividing the total count rate by the number of particles passing through the detector per unit time (N_i) as shown in Equation 26

$$\varepsilon_{int} = \frac{\int_{LLD}^{\infty} f(x)\,dx}{N_i}\,. \tag{26}$$

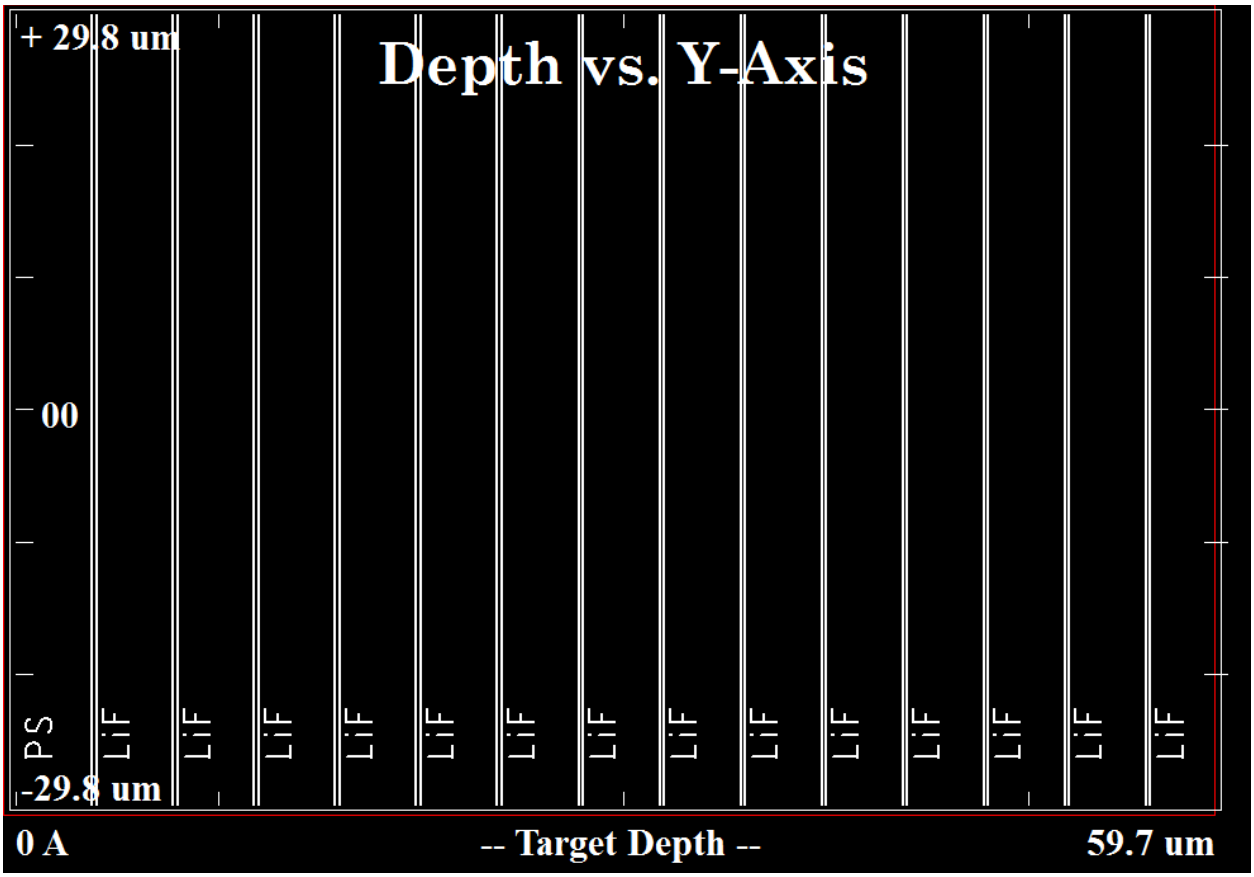


Figure 14. Simulated Geometry of PS Containing 10% ^{6}LiF Using the TRIM Code.

The detection criteria set forth in Chapter 1 state that the intrinsic efficiency for gamma-rays must be less than 10^{-6} while the absolute neutron detection efficiency is maintained at a minimum of 1.2×10^{-3} (or 2.5 cps/ng ^{252}Cf in the specified test configuration). To perform the calculations required to test a detector against these detection criteria, it is necessary to define a quantity called the mathematical lower level discriminator (MLLD). The MLLD is similar to the LLD in that all points occurring at channel numbers below the MLLD are discarded; however, the purpose of the MLLD is to discard real data rather than noise as with the LLD. Because it is sought to eliminate gamma-ray responses and preserve the thermal neutron responses, the value for the MLLD is obtained from the gamma-ray response spectrum according to Equation 27

$$\varepsilon_{int,\gamma} = \frac{\int_{MLLD}^{\infty} \gamma(x)\,dx}{N_{i,\gamma}} \tag{27}$$

where $\varepsilon_{int,\gamma}$ is the gamma-ray intrinsic efficiency, $\gamma(x)$ is the gamma-ray count rate spectrum, and $N_{i,\gamma}$ is the number of gamma-rays incident on the detector surface per unit time. The MLLD at which the value of $\varepsilon_{int,\gamma}$ reaches 10^{-6} can be determined by analysis of a plot of $\varepsilon_{int,\gamma}$ against MLLD. The MLLD determined from Equation 27 is then used to determine the remaining neutron count rate above the MLLD (Equation 28) and the neutron detection efficiencies. The remaining neutron count rate above the MLLD ($CR_{n>MLLD}$) is calculated using Equation 28

$$CR_{n>MLLD} = \int_{MLLD}^{\infty} n(x)\,dx \tag{28}$$

where $n(x)$ is the neutron count rate spectrum. The remaining intrinsic neutron detection efficiency ($\varepsilon_{int,n>MLLD}$) is calculated by using Equation 29

$$\varepsilon_{int,n>MLLD} = \frac{\int_{MLLD}^{\infty} n(x)\,dx}{N_{i,n}} \tag{29}$$

where $\varepsilon_{int,n>MLLD}$ is the intrinsic neutron detection efficiency above the MLLD and $N_{i,n}$ is the number of thermal neutrons incident on the detector per unit time. The absolute neutron detection efficiency above the MLLD ($\varepsilon_{abs,n>MLLD}$) is determined in a similar manner and the relationship is shown in Equation 30 where A_n is the rate of neutron emission from the source.

$$\varepsilon_{abs,n>MLLD} = \frac{\int_{MLLD}^{\infty} n(x)\,dx}{A_n} \tag{30}$$

Calculation of GARRn values requires the measurement of two quantities: the thermal neutron count rate in the presence of a 10 mR/hr gamma-ray field and the thermal neutron count rate in the absence of a 10 mR/hr gamma-ray field. Due to concerns associated with the personnel dose that would be obtained by placing both the ^{252}Cf and the 95.79 μCi ^{60}Co sources in one of the available irradiators to obtain the neutron count rate in the presence of both sources, values for GARRn were not measured.

Chapter 5: Results and Discussion

5.1. Analysis and Purification of ^{6}LiOH

The spectrogram from a QSTAR LC/MS analysis of the enriched lithium hydroxide showed two peaks. The peak corresponding to $^{6}LiOH \cdot H_2O$ (H^+) was shown at M/Z = 42.0361 g/mol with an integral value of 6100 and that corresponding to $^{6}LiOH \cdot H_2O$ (H^+) was shown at M/Z = 43.0203 g/mol with an integral value of 149. The degree of enrichment was determined to be 97.6% ^{6}Li and 2.4% ^{7}Li. Appropriate weighting of the masses of ^{6}Li and ^{7}Li gives an average molar mass of Li in the stock material to be 6.037 g/mol.

The stock LiOH was purified by dissolving in methanol at 13 g/L and filtering with a 1 μm filter. The LiOH is appreciably soluble in methanol whereas the impurities Li_2CO_3 and Li_2SiO_3 are negligibly soluble. The hydrating water molecules in the hydrated LiOH undergo exchange with the methanol molecules. Thus, evaporation of the methanol from the material results in anhydrous ^{6}LiOH. P-XRD diffractograms over the 2θ range 15° – 40° illustrating the

differences among LiOH, LiOH · H_2O, and Li_2CO_3 are shown in Figure 15. The distinctly different diffraction patterns among the three compounds illustrate that the atmospheric stability of LiOH can be monitored using this technique. ICP-OES analysis supports the data obtained from p-XRD regarding the material purity.

5.2. Justification of Experimental Design

5.2.1. Comparison of Lithium Salts

As described in section 4.2., it was determined that ^6LiF, $^6Li_3PO_4$, and ^6LiSal were the most appropriate salts for use in this application. ^6LiSal is hygroscopic and incorporation of it into many organic polymers results in opaque and very brittle films. To determine whether ^6LiF or $^6Li_3PO_4$ was better for use in the composite approach, scintillation films were fabricated containing each of the salts. The films were fabricated to contain the same total mass of ^6Li to ensure that the thermal neutron count rate remained constant. The first sample was PS containing 10% ^6LiF and 5% PPO/POPOP and was 50 μm thick. The second sample was PS containing 14.6% $^6Li_3PO_4$ and 5% PPO/POPOP and was 50 μm thick. Both samples contained a total of 2.73 mg ^6Li. The film containing ^6LiF had a light yield approximately 5% higher than that corresponding to the film containing $^6Li_3PO_4$. This difference is very small, so ^6LiF was chosen based on its higher transparency to photons in the ultraviolet region.[108]

5.2.2. Repeatability of Fabrication and Scintillation Measurement Protocols

In order to estimate the repeatability of the fabrication and measurement protocols, three compositions were fabricated three times each and the thermal neutron count rates were measured. The films were PS films containing 10%, 20%, and 30% ^6LiF with 5% PPO/POPOP,

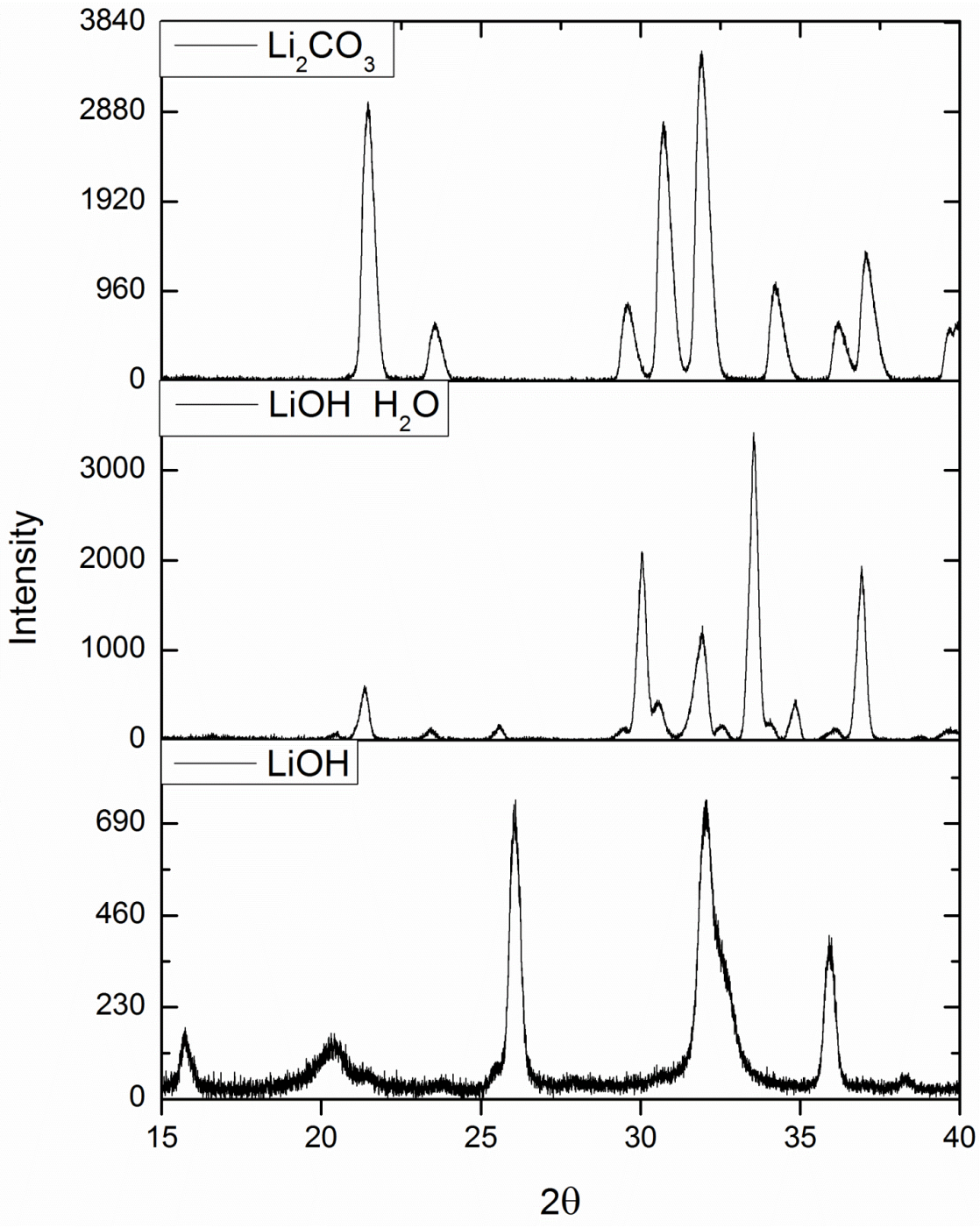


Figure 15. Powder X-Ray Diffraction Patterns of LiOH, LiOH · H_2O, and Li_2CO_3.

Acknowledgement: John D. Auxier II for sample preparation and conducting the p-XRD experiment.

each 50 μm thick. The results are shown in Table 9 and the error values indicate that the fabrication and measurement protocols are repeatable. The small differences in the net neutron count rates are attributed to inherent error in measuring submilligram quantities during sample fabrication, small irregularities in the films, and small changes in geometry among multiple measurements.[109]

To determine the effect of using different casting substrates on the scintillation responses, the 50 μm films were characterized by alpha, beta, and gamma-ray irradiation. Three different substrates were investigated: 1 mm thick PMMA, 3 mm thick UVT, and 6 mm thick UVT. The resulting data are listed in Table 10 where $CR_{n,th}$ is the total thermal neutron count rate. The spectral averages for the three films cast on 3 mm UVT are consistent enough such that the counting statistics are the greatest source of error. The two films cast on PMMA are also consistent; however, the light output is slightly reduced for alpha particles and markedly reduced for neutrons relative to the films cast on 3 mm UVT. It is also interesting to note that the neutron count rate (CR_n) is much greater for the films cast on UVT as compared to those cast on PMMA. The film on 6 mm UVT showed a significant reduction in the neutron count rate relative to the films cast on 3 mm UVT. It was thus determined that of the substrates investigated, the 3 mm UVT substrate was the best substrate for this application.

It was first hypothesized that the differences in the results between the PMMA and UVT disks was due to reduced optical transmission of the PMMA relative to the UVT. Mounting the samples onto the face of the PMT with the film side opposite to the PMT requires that every emitted photon must travel through the disk before reaching the PMT. By coupling the film side of the samples to the face of the PMT, the fraction of the emitted photons that must travel through the disk before reaching the PMT is decreased. If the observed effect is due to a reduced

Table 9. Repeatability of Neutron Count Rate Measurements

Film Thickness	*wt% ^{6}LiF*	*Mass of Li (97.6% ^{6}Li)*	*$CR_{n,th}$*
50 μm	10	2.54 mg	25.2 ± 0.5
	20	5.83 mg	52.2 ± 2.6
	30	9.36 mg	91.4 ± 2.7

Table 10. Effects of Substrate on Scintillation Responses

Substrate	*α Peak*	*β Avg*	*Thermal Neutron Avg*	*γ Avg*	*$CR_{n,th}$*
GS20	-----†	-----†	3441	745	353.2
1 mm PMMA	2040	227	235	212	7.3
1 mm PMMA	1910	211	289	215	6.0
3 mm UVT Acrylic	2220	262	1000	222	25.2
3 mm UVT Acrylic	2220	250	1055	224	25.7
3 mm UVT Acrylic	2220	256	1023	218	24.7
6 mm UVT Acrylic	1940	252	777	226	18.2

The amplifier was set at a gain of 25 during this experiment.

†These values were not measured during this experiment.

transmission, then changing the mounting orientation in this manner would reduce the difference in the scintillation response. However, the differences in the responses were nearly identical in both orientations. The fundamental reason for this issue remains unresolved.

5.3. Polystyrene-Based Detectors

A series of polystyrene-based films containing ^{6}LiF and PPO/POPOP blend were fabricated by solution casting, as described in section 4.3. The optical and scintillation properties were investigated for films over a range of compositions and thicknesses. It should be noted that I published some of the work presented in this section.[109] This discussion includes a more detailed discussion of photoluminescence and neutron/gamma-ray discrimination than that which is included in the previously published material.

5.3.1. Effects of ^{6}LiF on Optical Clarity

An image demonstrating the relative optical clarities of films over the thickness range 15 – 150 μm containing various amounts of ^{6}LiF is shown in Figure 16. At a constant concentration of ^{6}LiF, thicker samples are less transparent than thinner samples. Increasing the concentration of ^{6}LiF decreases the optical clarity as would be expected due to the difference in refractive indices between the ^{6}LiF and the PS. This decrease in optical clarity is more highly dependent on the concentration of ^{6}LiF in thicker samples than in thinner samples. The 15 μm thick samples do not show much change in transmission among films cast with 10 – 30% ^{6}LiF. The morphology and size distribution of the ^{6}LiF particles in the composites were examined confocal laser-scanning microscopy (CLSM) and a representative image is shown in Figure 17. Cubic ^{6}LiF particles with a mean size of 3.2 μm are clearly visible in the image. Several images in different

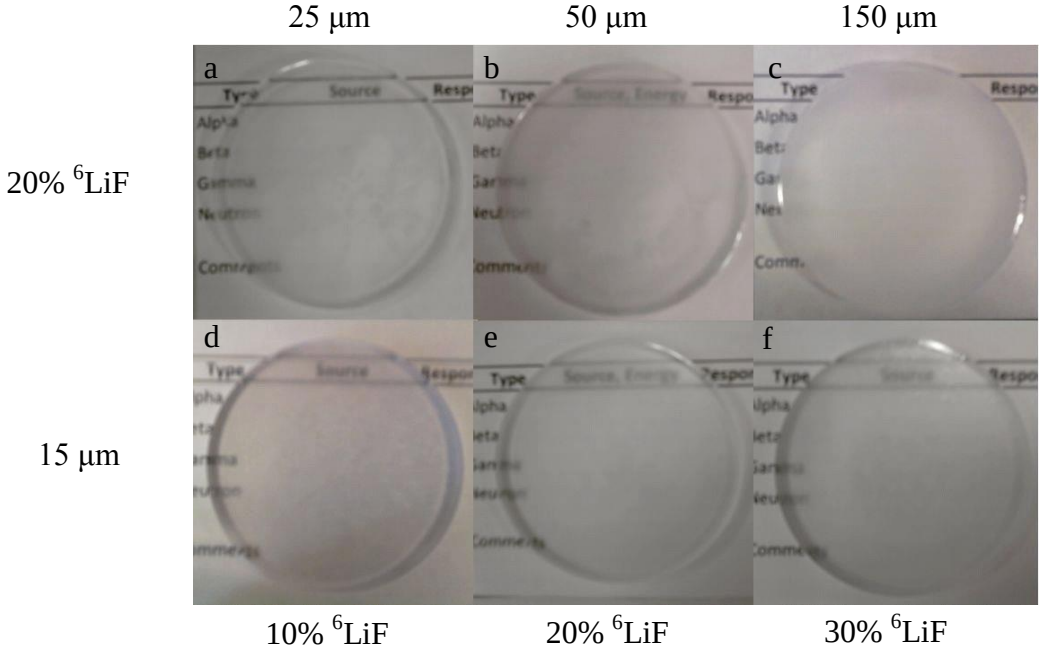


Figure 16. Representative Images of PS Composite Films Containing ^{6}LiF and PPO/POPOP. All films contain 5% PPO/POPOP; the amounts of ^{6}LiF and the thicknesses were varied. The films are placed on cards containing text to demonstrate the relative optical clarity. Film compositions are a) 20% ^{6}LiF at 25 µm, b) 20% ^{6}LiF at 50 µm, c) 20% ^{6}LiF at 150 µm, d) 10% ^{6}LiF at 15 µm, e) 20% ^{6}LiF at 15 µm, and f) 30% ^{6}LiF at 15 µm.

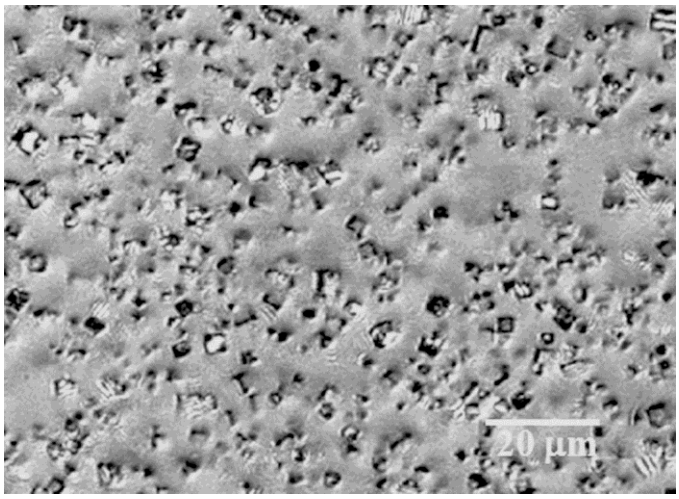


Figure 17. Bright-Field CLSM Image of ^{6}LiF Particles Distributed in a PS Matrix.

The mean particle size is 3.2 µm and the range in particle size is 1.6 – 5.3 µm. The scale bar is 20 µm. Acknowledgement: Stephen A. Young for conducting the experiment.

places of the sample were obtained and provide evidence that the particles are randomly distributed in the matrix and not agglomerated.

5.3.2. Fluorescence

A typical photophysical mechanism for the possible routes of excitation energy transport in a PS matrix containing PPO as the primary fluor and POPOP as the wavelength shifter is shown in Scheme 1 where φ_f is quantum efficiency of fluorescence,[41] λ_i represents a photon with a wavelength characteristic of the process, and * indicates an electronically excited state. It has been demonstrated that the energy transfer from PS to PPO is more efficient for the S_1 state than for either the S_2 or the S_3 states; thus, the photoluminescence experiment was designed to irradiate a solid PS film with photons at 278 nm to generate the S_1 excited state.[110] After the S_1 state is generated, there are three primary competing processes that determine the fate of the excitation energy: The excited monomer unit can 1) quench the excitation either by a nonradiative process to the S_0 state or by transferring the energy to a nonfluorescent impurity, 2) emit a photon at λ_2, or 3) nonradiatively transfer the energy to PPO. Transfer of excitation energy between PS and PPO occurs primarily by a nonradiative mechanism in which the energy is transferred without emission of a photon; however, a small fraction of the energy transferred from PS to PPO is photon-mediated.[111] The transfer of the excitation energy generates the PPO S_1 state which fluoresces with a 100% quantum yield.[41] This photon is reabsorbed by POPOP which then reemits the photon at a longer wavelength with a quantum yield of 93%.[41] A typical normalized fluorescence spectrum of a sample containing PS and PPO/POPOP is shown in Figure 18. The excitation and emission spectra of pure PS are also shown on the plot to demonstrate that the styrene subunits are the entities that are excited.

Scheme 1. Mechanisms of Excitation Energy Transport in PS films Containing PPO/POPOP

1.) Excitation of Matrix

$$PS + \lambda_1 \rightarrow PS^*$$

2.) Matrix Relaxation

$$PS^* \rightarrow PS$$

$$PS^* \rightarrow PS + \lambda_2 \qquad (\varphi_f = 0.16)$$

$$PS^* + PPO \rightarrow PS + PPO^*$$

3.) PPO Excitation

$$PS^* + PPO \rightarrow PS + PPO^*$$

$$PPO + \lambda_2 \rightarrow PPO^*$$

4.) PPO Relaxation

$$PPO^* \rightarrow PPO + \lambda_3 \qquad (\varphi_f = 1.00)$$

5.) POPOP Excitation

$$\lambda_3 + POPOP \rightarrow POPOP^*$$

6.) POPOP Relaxation

$$POPOP^* \rightarrow POPOP$$

$$POPOP^* \rightarrow POPOP + \lambda_4 \qquad (\varphi_f = 0.93)$$

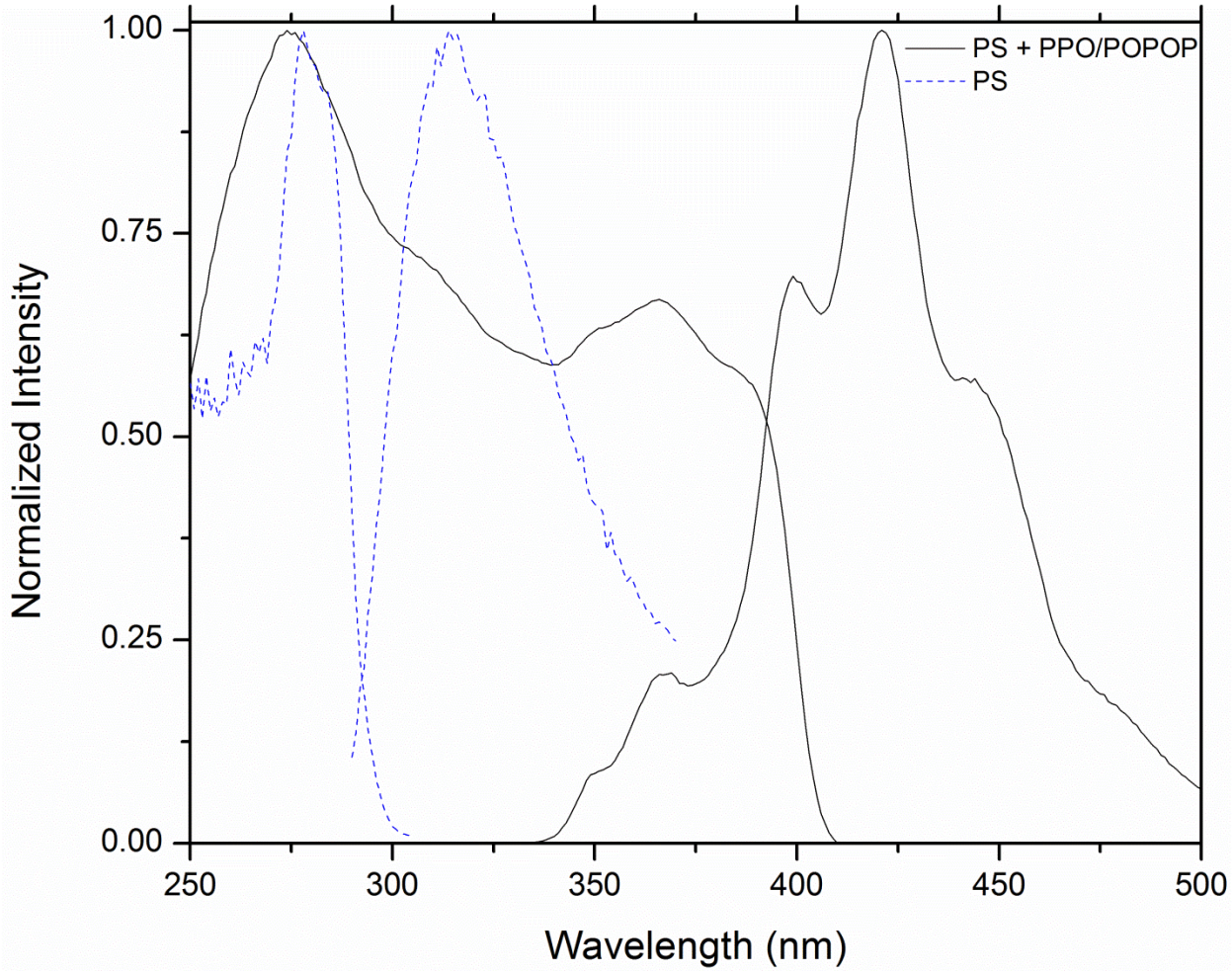


Figure 18. Normalized Fluorescence Spectra of PS and of PS Containing PPO/POPOP.

The blue dotted lines are the fluorescence spectra of pure PS and are shown to illustrate that the styrene subunits are the initially excited entities in the experiment.

Before incorporation of ^{6}LiF in the matrix, it was first necessary to optimize the concentration of PPO/POPOP in order to maximize the light yield. The fluorescence responses of PS containing varying concentrations of PPO/POPOP were analyzed to determine the most suitable concentrations for use in these samples and are shown in Figure 19. To maximize the light yield, it was first necessary to ensure that the maximum amount of excitation energy is collected from the PS matrix. By measuring the excitation intensity that results in emission from PS (290 – 330 nm) as a function of PPO/POPOP concentration, the concentration at which the observable PS emission becomes negligible can be determined. This should be the concentration at which transfer to PPO is optimum and no light is lost as emission from PS. The fluorescence emission in response to excitation at 278 nm for PPO/POPOP concentrations over the concentration range 0.55 – 5.00% are shown in Figure 19. It can be seen from this plot that the maximum intensity is achieved at 5.00%. The emission spectra for samples containing more than 5.00% PPO/POPOP are not shown to improve the clarity of the figure. The inset plot is an expanded view of the region 290 – 330 nm and is included to demonstrate the reduction in PS emission.

The data in Figure 20 show that the emission from PS decreases rapidly with the addition of low concentrations of PPO/POPOP. At 1.49% PPO/POPOP the emission from PS is reduced by approximately 96%. The concentration at which sufficient fluor molecules are present to collect the excitation energy from PS such that no emission from PS is observed should be the optimized composition. However, considering that quantum efficiency of a pure PS film is approximately 16%, it is possible that more excitation energy can be collected by further increasing the fluor concentration. It can be seen in Figure 20 that although 96% of the PS emission is quenched at 1.49% PPO/POPOP, only about 55% of the maximum integrated

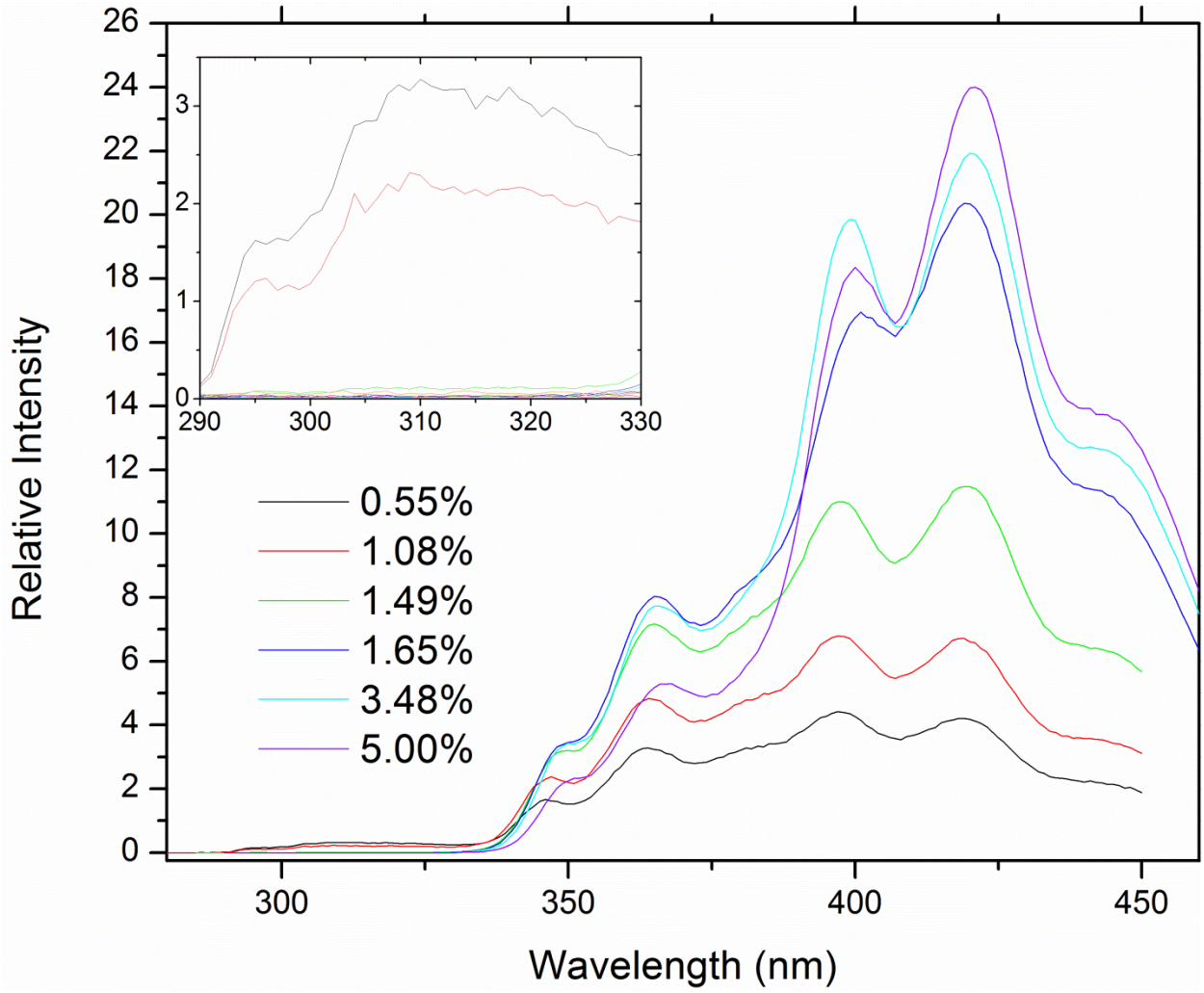


Figure 19. Fluorescence Emission Spectra of PS Films Containing Various Concentrations of PPO/POPOP.

The inset plot is an expanded view of the region 290 – 330 nm to demonstrate the reduction in emission intensity from PS.

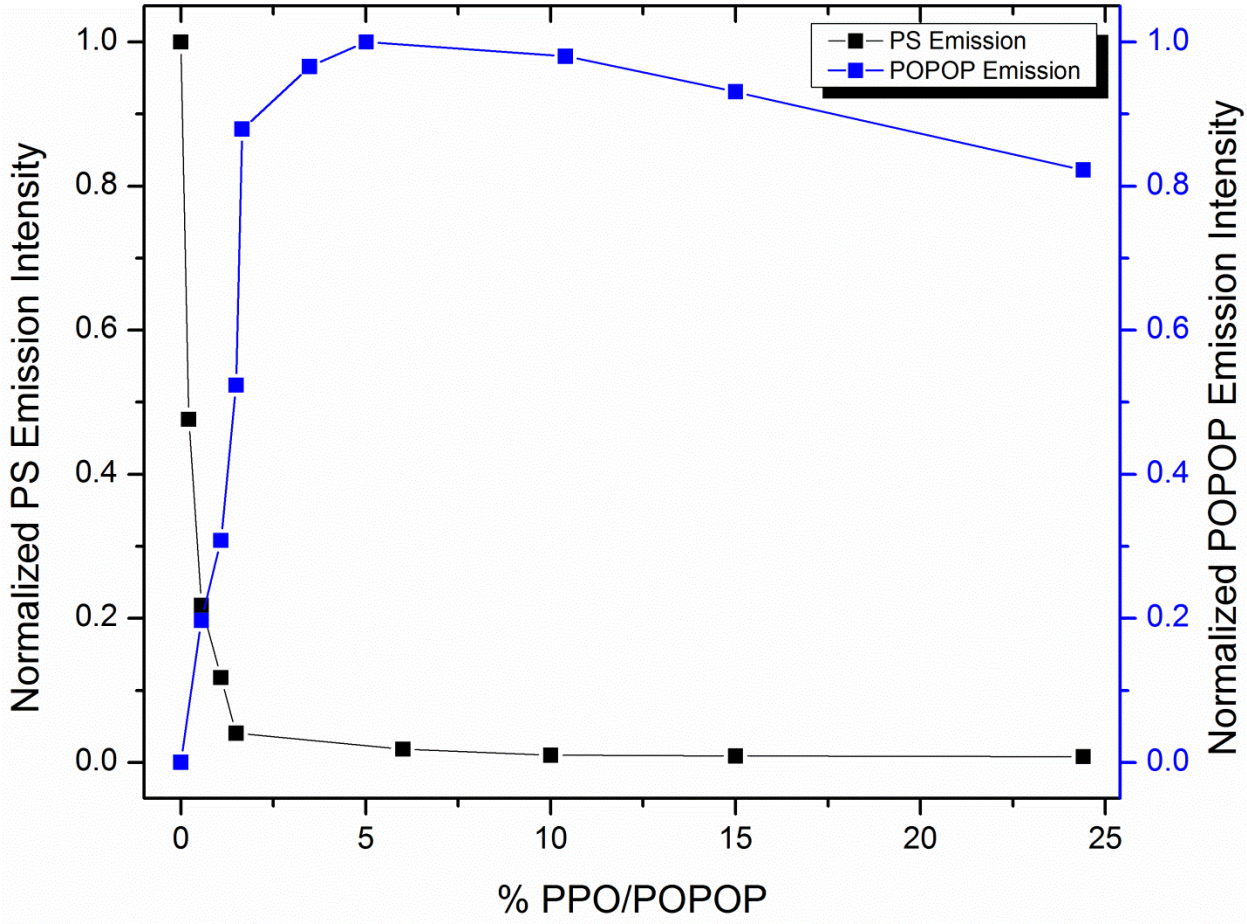


Figure 20. PS and POPOP Emission for 150 μm PS Samples as a Function of Wt% PPO/POPOP. PS emission was obtained by measuring the excitation spectrum that yielded emission at 314 nm, then integrating each spectrum over the region 250 nm – 300 nm. POPOP emission intensity was obtained by measuring the emission spectrum resulting from excitation at 278 nm, then integrating over the region 390 nm – 440 nm. Both curves are normalized to the maximum intensity point in each set. Lines connecting the points are drawn to improve the clarity of the overall trends and do not represent assumptions of unmeasured data.

emission intensity from POPOP is achieved at this concentration. Further addition of PPO/POPOP up to 5.00% results in an increase in emission intensity. The emission intensity levels off until 10% PPO/POPOP, then decreases at higher concentrations due to self-absorption. This demonstrates that the optimum concentration of PPO/POPOP in PS films is approximately 5.00%. It is interesting to note that the concentration at which nearly all PS emission is quenched, addition of more fluor molecules significantly increases the amount of excitation energy that can be collected from PS by PPO. This effectively increases the overall quantum efficiency of the system. PPO does absorb photons at 278 nm, but a comparison of the relative absorbances of PS and PPO at 278 nm for a film containing 5% PPO/POPOP using the relationship shown in Equation 30

$$\frac{Absorbance_{PS,\ \lambda=278\,nm}}{Absorbance_{PPO,\ \lambda=278\,nm}} = \frac{(\epsilon_{PS,\lambda} l[PS])_{\lambda=278\,nm}}{(\epsilon_{PPO,\lambda} l[PPO])_{\lambda=278\,nm}} \tag{30}$$

where $\varepsilon_{i,\lambda}$ is the extinction coefficient at 278 nm,[112,113] l is the path length, and [*PS*] and [*PPO*] are the concentrations of PS and PPO, respectively, gives a ratio of the absorbances of PS to PPO of 148. This indicates that only about 0.7% of the absorbed photons are absorbed by PPO whereas the remaining 99.3% are absorbed by PS. Thus, absorption of the incident photons by PPO is inadequate to explain the increase in the integrated emission intensity by a factor of 2 between the concentrations of 1.49% and 5.00%. The increase must therefore be attributed to an increased number of excitations transferred from PS to PPO. It is thus determined that even though the overall quantum efficiency of the pure matrix is low, the quantum efficiency of the

overall emission can be improved by utilization of a fluor to which the matrix efficiently transfers excitations before vibrational relaxation occurs.

It is also evident from the data in Figure 19 that emission in the region 340 – 390 nm, corresponding to PPO fluorescence, increases until 1.65% PPO/POPOP, but the emission in this region is reduced for films containing higher concentrations. At concentrations of 10%, 15%, and 24.4% PPO/POPOP, emissions in this region is further decreased, but the integrated intensities in the region 390 – 440 nm do not demonstrate the same trend. It is suspected that the relative emission intensities of the films could possibly be improved by adding more POPOP to collect the photons emitted from PPO. However, the preblended fluor mixture was used throughout the remaining course of experimentation in order to reduce the error in measuring submilligram quantities, thereby reducing any variations in the ratio of PPO to POPOP among different films.

It is generally agreed upon that effective scintillators must be transparent to their own scintillation light. To determine the effect of reduced optical transmission on fluorescence, the emission spectra were measured for samples containing 10% PPO/POPOP with varying concentrations of ^{6}LiF in response to excitation at 278 nm and are shown in Figure 21. Comparison of the relative emission intensities demonstrates that increasing the amount of ^{6}LiF in the sample increases the emission intensity. This can be rationalized by considering that the PS/^{6}LiF composite is a mechanical mixture with 3.2 μm cubic ^{6}LiF particles trapped inside the PS matrix. Because the refractive indices of lithium fluoride and polystyrene are different and the particles are sufficiently larger than the wavelength of incident light, each particle acts as a scattering site for the incident excitation photons. A greater the number of scattering sites in the matrix increases the overall path length of any given photon in the film. The Beer-Lambert law indicates that absorption of a photon by a material is dependent on both concentration and path

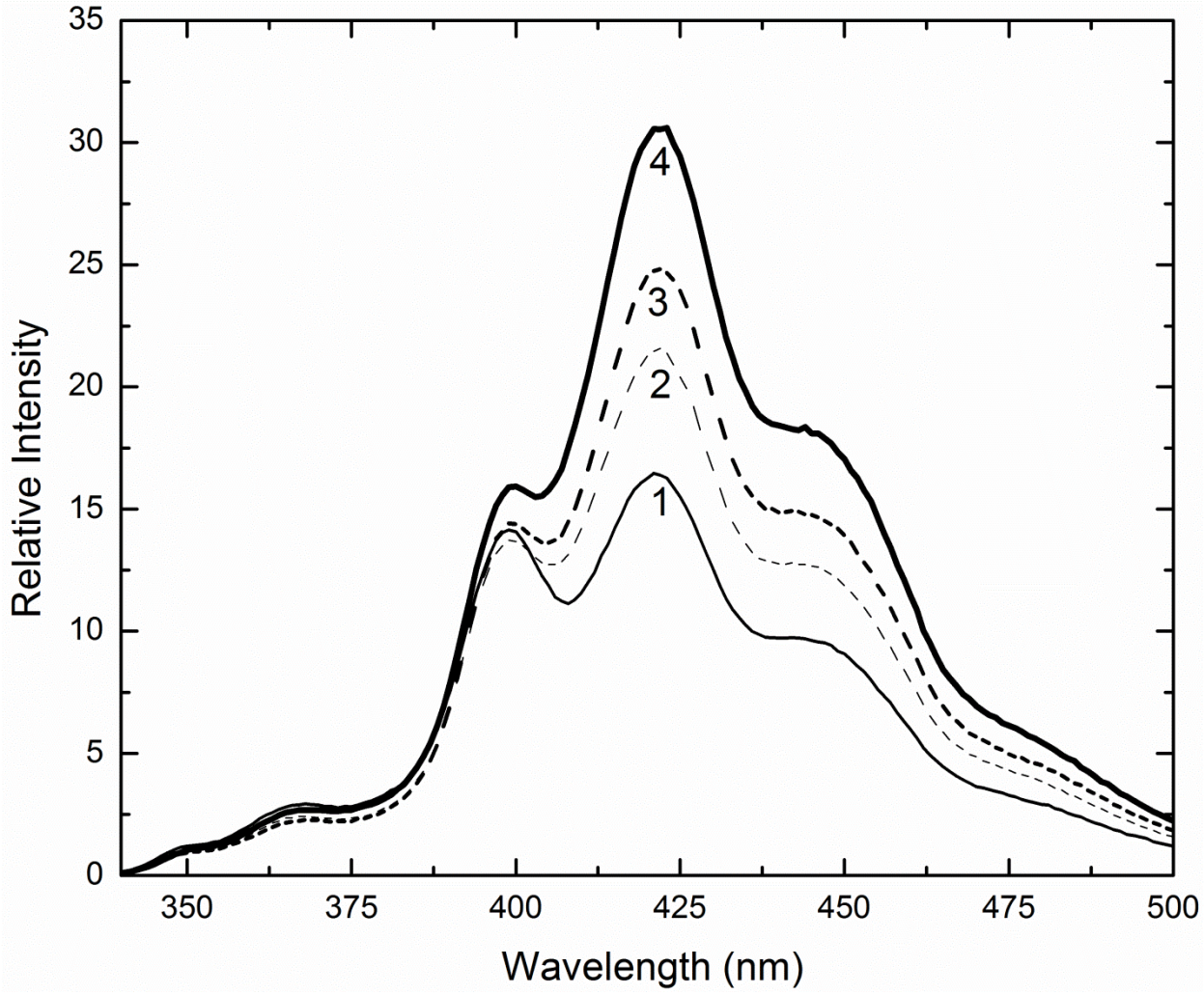


Figure 21. Emission Spectra of 150 μm Thick PS Films Containing 10% PPO/POPOP at Various Loadings of ^{6}LiF.

Spectra were obtained by excitation at 278 nm. Spectra are numbered according to the following percentages of ^{6}LiF: (1) 0%, (2) 10%, (3) 15%, (4) 20%.

length of the absorbing medium. It was shown in Figure 19 and Figure 20 that increasing the concentration of PPO/POPOP above 10% results in a decrease in the observed emission, so the observed phenomenon in Figure 21 cannot be due to a higher probability of scattered photons emitted from PPO being captured by POPOP. This also cannot be attributed to the energy transfer between PS and PPO because this mechanism occurs primarily without emission of a photon and should be independent of the presence of the ^{6}LiF. Thus, the most probable explanation for this phenomenon is that the greater number of scattering sites increases the average path length of the incident excitation photons through the film, resulting in a greater probability that an incident photon will be absorbed by the PS. The increased number of S_1 states on the polymer results in an increase in the number of photons that are transferred to PPO and ultimately emitted by POPOP.

5.3.3. Scintillation

The films were characterized by responses to alpha particles from ^{241}Am. Alpha responses of films with different percentages of fluor (0.1 – 15%) were measured for 50 μm and 150 μm samples. Peak positions indicated that the optimum concentration of PPO/POPOP was 5%, which is in agreement with the fluorescence data. This weight percentage was used throughout the rest of the experimentation. Alpha responses of samples containing 10% ^{6}LiF and 5% PPO/POPOP over the thickness range 15 μm – 150 μm are shown in Figure 22 and the corresponding peak positions, spectral averages, and light yields in photons/alpha are shown in Table 11. It is observed thinner samples have a decreased resolution and therefore a decreased average light output as characterized by the broad peaks whereas the thicker samples show a sharper peak and therefore a greater average light output. This is attributed to the fact that the

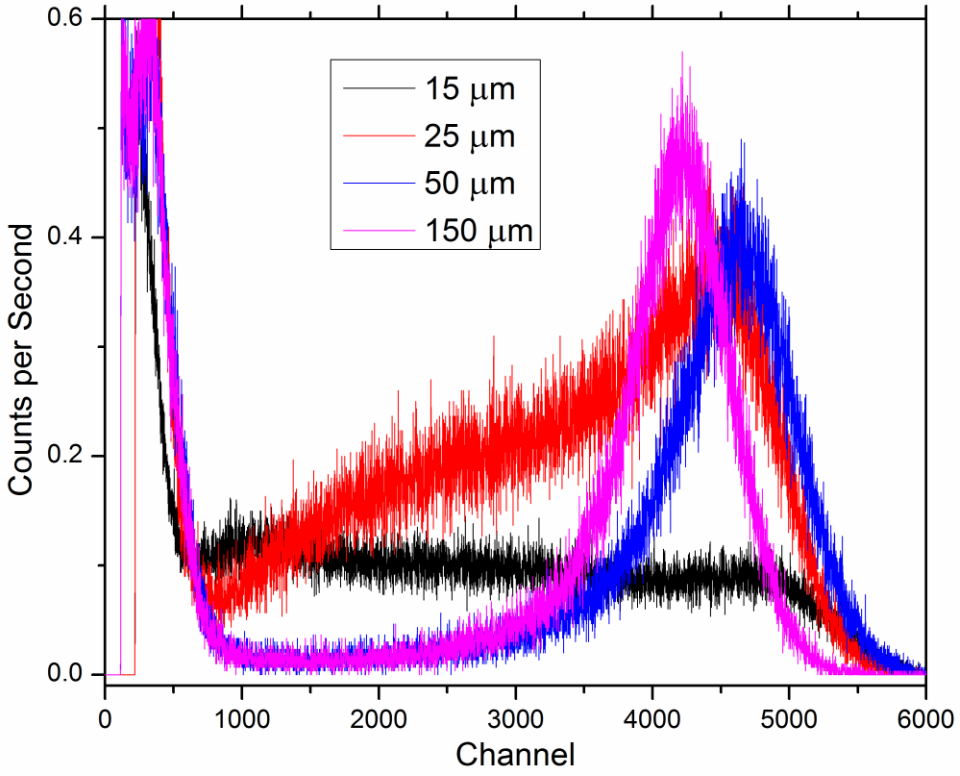


Figure 22. Alpha Responses for PS Samples Containing 10% ^{6}LiF and 5% PPO/POPOP over the Thickness Range 15 – 150 μm.

Table 11. ^{241}Am Alpha Spectral Features of 15 - 150 μm PS-Based Films

Film Thickness	*Peak*	*<x>*	*LY (photons/alpha)**
15 μm	No Peak	2398	4406
25 μm	4536	2774	5097
50 μm	4645	3068	5637
150 μm	4228	2835	5209

The amplifier was set at a gain of 20 for these measurements.

*Calculated based on GS20 emitting 6,250 photons per thermal neutron.

range of the incident 5.484 MeV alpha particle is approximately 37.3 μm in the composite, as shown in Table 12, which exceeds the thicknesses of the 15 and 25 μm thick films. This indicates that a large fraction of the incident alpha particles are not completely stopped in the 15 and 25 μm films, whereas they are completely stopped in the 50 and 150 μm films. Thus, it is expected that the resolution should be poorer in the 15 and 25 μm films and improved in the 50 and 150 μm films. It can also be seen that the light output is reduced in the 150 μm film relative to the 50 μm film. This is attributed to greater self-absorption and greater scattering probability of the scintillation light in the 150 μm sample. The active volume is only about 37.3 μm deep as evidenced by the calculated range of the alpha particle; thus, the scintillation light must travel a greater distance in the 150 μm film to reach the PMT as compared to the 50 μm film which increases the probability that self-absorption or scattering will occur. This demonstrates that increasing the thickness of the film beyond what is required to stop the charged particles results in a decrease in the light yield.

Several PS films were fabricated containing 10% ^{6}LiF and 5% PPO/POPOP over the thickness range 15 – 601 μm and each was characterized by neutrons and gamma-rays for light

Table 12. Ranges of Heavy Ions in PS and ^{6}LiF

Material	α^{2+} *(5.484 MeV)*	α^{2+} *(2.05 MeV)*	t^{+} *(2.73 MeV)*
PS	38.7 μm	9.85 μm	57.1 μm
^{6}LiF	21.1 μm	6.05 μm	33.8 μm
PS + 10% ^{6}LiF	37.3 μm	9.80 μm	55.9 μm

These values are the results from simulating 5000 incident ions using the TRIM code. The compound data file for LiF was modified to account for the isotopic enrichment of ^{6}Li.

yield and neutron and gamma-ray detection efficiency. The spectral averages for neutrons of all energies in the Pb tube and thermal neutrons obtained by the Pb – Cd subtraction as well as for gamma-rays were determined for each film using Equation 19. The light yields were then calculated from the spectral averages using Equation 20 and are shown in Table 13.

The gamma-ray intrinsic efficiency as a function of MLLD was determined using Equation 27 for each film and the corresponding plots are shown in Figure 23. The plots clearly demonstrate the MLLD value at which the gamma-ray intrinsic efficiency of each film reaches 10^{-6}. It is also evident from the plots that the light yield due to gamma-rays increases with increasing film thickness and that gamma-ray rejection is more easily achieved with thinner films than with thicker films.

Figure 24 shows the thermal neutron count rate spectrum superimposed on the gamma-ray intrinsic efficiency plot for the 50 μm film. The line representing the gamma-ray intrinsic efficiency falls to 10^{-6} at channel 1894. The neutron count rate spectrum can be integrated from channel 1894 to infinity, as described in Equation 28, to calculate the neutron count rate above the MLLD. This calculation was performed for each of the films both for thermal neutrons

Table 13. Light Yields of PS-Based Films for Gamma-Rays and Neutrons

Thickness (μm)	*Gamma-Rays*	*Pb – Cd*	*Pb*
15	246	1147	328
25	280	1561	457
50	312	1864	648
151	451	1868	988
292	643	2249	1486
601	973	1942	1578

Calculated based on GS20 emitting 6,250 photons/thermal neutron. Values are reported as photons/particle. Pb – Cd is the thermal neutron spectrum obtained by subtracting the response in the cadmium tube from that in the lead tube. Pb is the response in the lead tube.

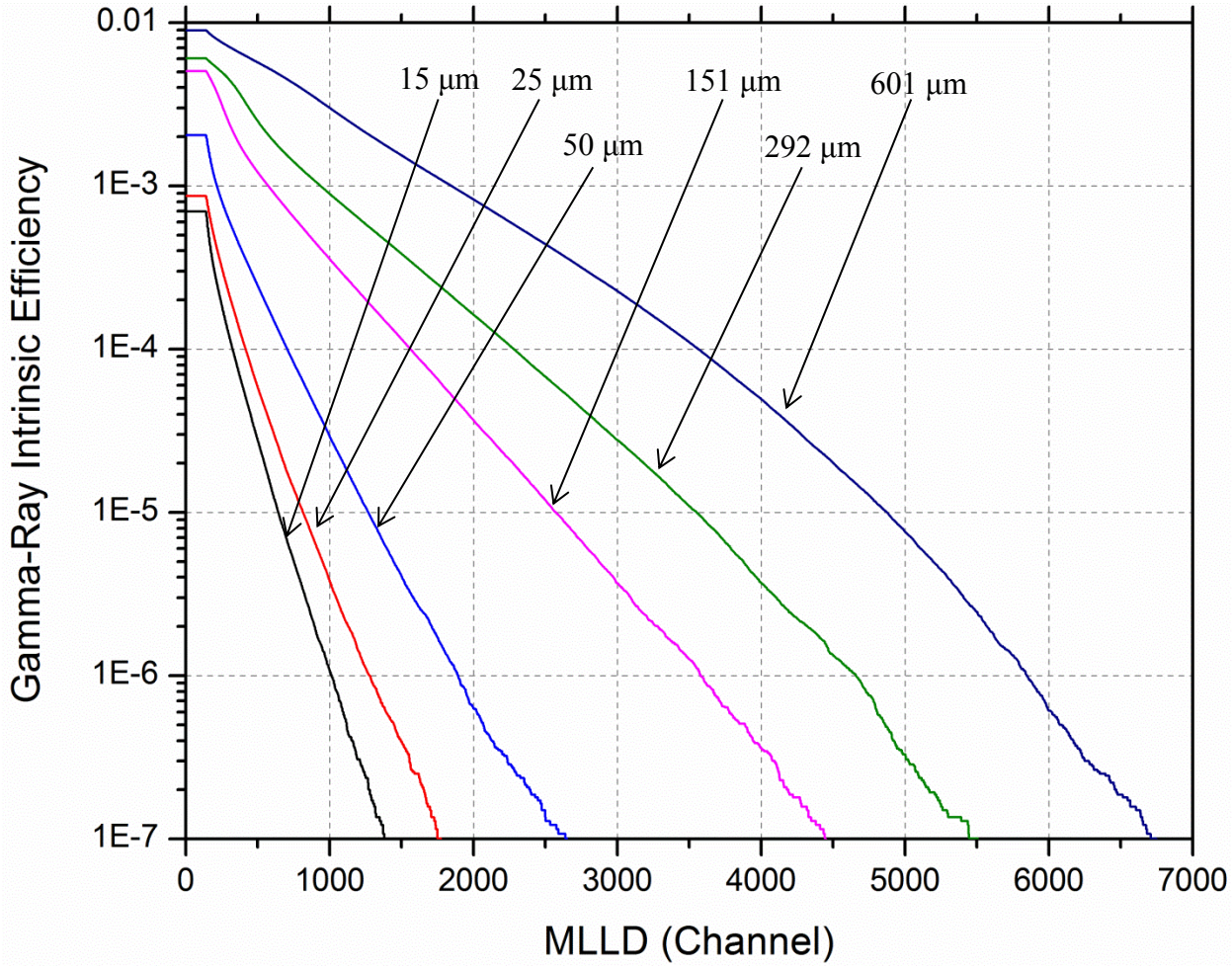


Figure 23. Gamma-Ray Intrinsic Efficiency as a Function of MLLD for Film Thicknesses over the Range 15 – 601 µm.

The MLLD at which each film has a gamma-ray intrinsic efficiency of 10^{-6} can be clearly seen in each plot. The amplifier was set to a gain of 25 for these measurements.

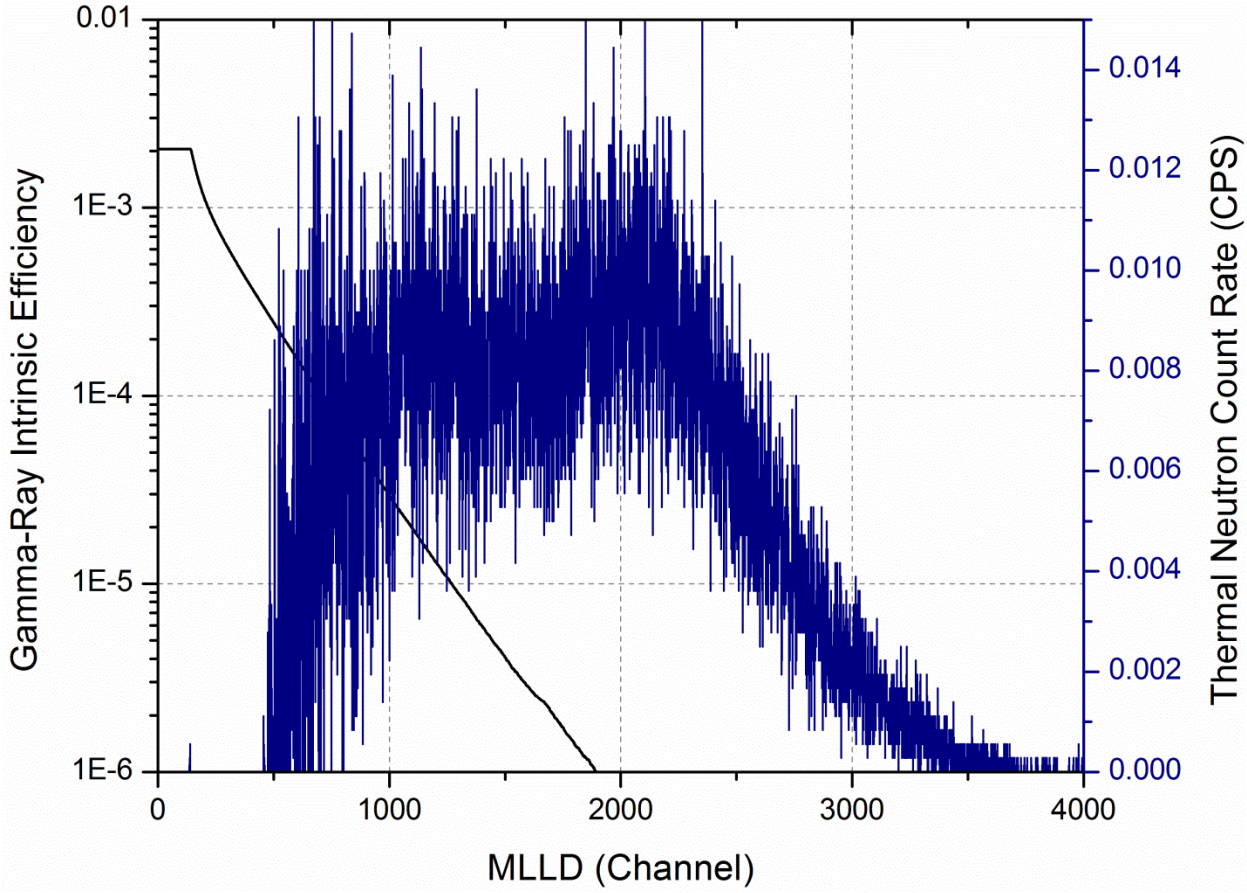


Figure 24. Gamma-Ray Intrinsic Efficiency and Thermal Neutron Count Rate Spectrum for a PS Film 50 μm Thick Containing 10% ^{6}LiF and 5% PPO/POPOP.

The gamma-ray intrinsic efficiency is shown in black and the neutron count rate spectrum is shown in blue. The amplifier was set to a gain of 25 for these measurements.

(Pb – Cd) and for neutrons of all energies (Pb). The results of these calculations are shown in Table 14. The data in Table 14 indicate that the 50 μm thick film has the highest total neutron count rate above the MLLD and is thus the best sample for discrimination between neutron and gamma-ray events using pulse height discrimination.

Thermal neutron capture by ^{6}Li produces an alpha particle (2.05 MeV) and a triton (2.73 MeV). As stated in Chapter 2, energy deposition by heavy ions results in the liberation of many low-energy secondary electrons in the ionization column. If elastic scattering is assumed, the maximum kinetic energy that can be imparted to a secondary electron by the alpha particle is 1.097 keV and by the triton is 1.986 keV. Compton-scattered electrons generated by gamma-rays produces are higher in energy, the maximum value of which can be calculated using Equation 8. ^{60}Co emits two gamma-rays per disintegration with energies of 1.173 MeV and 1.332 MeV. These gamma-rays produce Compton-scattered electrons with maximum energies of 0.96 MeV and 1.12 MeV and median energies of 860 keV and 1.07 MeV, respectively. Standard data tables can be used to estimate the ranges of these secondary electrons in PS, of which the estimated values are for heavy ions on the order of 10^{-1} μm and those for gamma-rays are on the order of 10^{4} μm. Thus, it is much more probable that the secondary electrons generated by heavy ions will deposit more energy in a thin film as compared to that deposited by secondary electrons generated by Compton scattering.[91] The fraction of energy deposited in the films by thermal neutron capture and from Compton-scattered electrons was simulated using GEANT4 (Geometry and Tracking Code). The results from the simulations are shown numerically in Table 15 and graphically in Figure 25. The values listed for Compton-scattered electrons are calculated from the average of the energies of the two gamma-rays emitted from ^{60}Co. Figure 25 illustrates that the fraction of energy deposited by the ^{6}Li fission products increases substantially until the film

Table 14. Neutron Count Rates Above Gamma-Ray MLLD for PS Films

Thickness (μm)	*MLLD ($\varepsilon_{int,\gamma} = 10^{-6}$)*	$CR_{n,th>MLLD}$	$CR_{n>MLLD}$
15	1016	1.61	1.85
25	1283	1.77	1.94
50	1894	7.77	8.34
151	3579	0.18	0.25
292	4661	0.34	0.47
601	5846	0.48	0.91

Table 15. Average Fraction of Energy Deposited in PS-Based Films of Various Thicknesses

Thickness (μm)	*Neutrons (^{6}Li fission products)*	*Gamma-Rays (Compton Electrons)*
15	0.53	0.010
25	0.63	0.013
50	0.78	0.022
150	0.93	0.037
300	0.97	0.064
600	0.98	0.104

These values are results from simulations using GEANT4. Acknowledgement: Matthew J. Urffer.

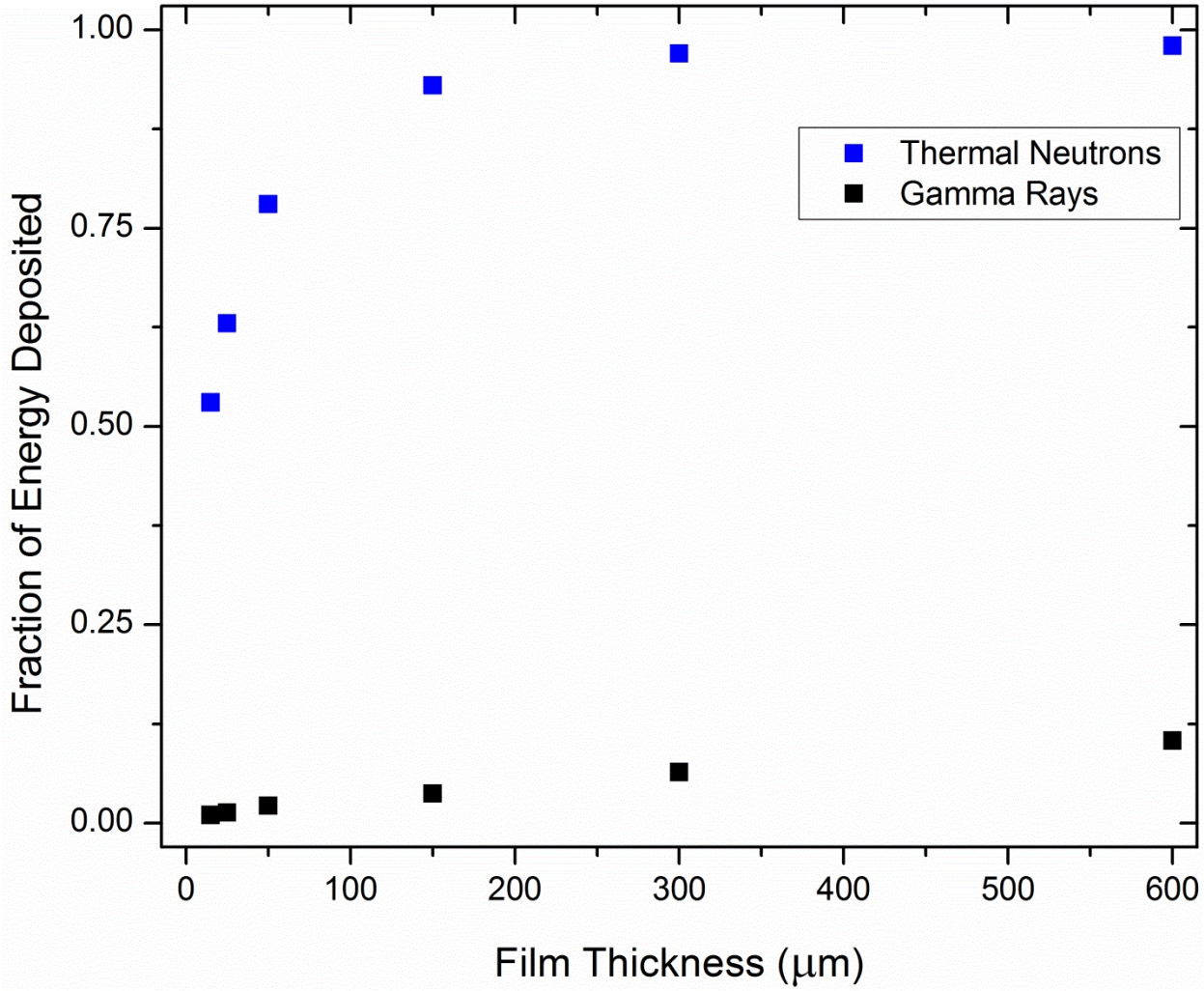


Figure 25. Fraction of Energy Deposited in PS-Based Films by Thermal Neutron Capture and Compton-Scattered Electrons from Gamma-Rays.

thickness becomes approximately 150 μm, then increases only very slowly thereafter, whereas the fraction of energy deposited by gamma-rays increases steadily over the entire range. It is thus not reasonable to increase the film thickness above 150 μm if the principle application is discrimination between thermal neutron and gamma-ray events.

The DHS configuration differs from the irradiator used for the neutron measurements in that the detector is to be placed 2 m from a ^{252}Cf neutron source encased in 0.5 cm of lead and moderated by 2.5 cm of HDPE as tabulated in Table 1. Thus, a more precise measurement permitting comparison of detector performance to the DHS criterion regarding neutron absolute efficiency is the measurement in the Pb tube rather than the response obtained from the Pb – Cd subtraction. The absolute neutron detection efficiency in the Pb tube is thus not subject to the errors discussed in section 4.5.6. regarding the subtraction procedure. The lead tube contains thermal neutrons, fast neutrons, and gamma-rays. The previous analysis permitted quantitative disentanglement and elimination of the pulses generated by gamma-rays from the detector responses such that only 1 in 10^{-6} gamma-rays that are incident on a detector surface generates a pulse that is incorrectly classified a neutron. The ^{252}Cf source emits gamma-rays at a rate of 4.9×10^{6} γ/μg·s. Using Equations 23 and 24, it can be determined that the total gamma-ray fluence across the surface of a 50 μm thick detector in the Pb tube in the irradiator is 2.3×10^{4} γ/s (calculated for January 1, 2013), which is significantly less than the value of 10^{-6}. The number of gamma-rays from ^{252}Cf that are misclassified as neutrons per second in the Pb tube can then be estimated according to Equation 31,

$$\#\frac{misclassifications}{s} = \frac{A_{\gamma}\Omega_{50\mu m,Pb}}{\varepsilon_{int\,\gamma}} = 2.3\times10^{-2}\,\frac{misclassifications}{second}, \tag{31}$$

which corresponds to a count rate of 0.023 counts per second. A significant portion of the gamma-rays are shielded by the Pb around the source and the Pb around the measurement tube, but many of the daughter nuclei produced from spontaneous fission of ^{252}Cf are also gamma-ray emitters which would increase the gamma-ray fluence in the Pb tube. Thus, this calculation provides an estimation of the upper limit of the error due to gamma-ray misclassifications in the Pb tube by setting the MLLD to the values listed in Table 14. It should be noted that the measurements have not been corrected for responses due to background, for spurious pulses generated by the high gamma-ray flux on the PMT dynodes, or for electronic noise other than by implementing the LLD. These corrections were omitted for two reasons. First, a deployed detector would be subject to background radiation, spurious pulses due to radiation interactions with the PMT, and electronic noise, all of which produce pulses that must be appropriately separated and eliminated from the pulses due to the radiation of interest by taking only a single measurement comprising all the signals. Second, the errors generated by these sources at the MLLDs in the gamma-ray intrinsic efficiencies were very small false positives, yielding values of intrinsic efficiencies that were slightly higher than the actual values which would result in an increased value for each calculated MLLD. As a result, more gamma-rays would be eliminated from the measurement and the actual values for $\varepsilon_{int\,\gamma}$ at the MLLD are actually lower than 10^{-6}. The response due to background, electronic noise, and spurious pulses due to the intense gamma-ray field on the PMT dynodes was measured and the total error in the gamma-ray intrinsic efficiency at the MLLD was calculated to be +0.048% for the 15 μm film and much smaller for all other films. This relative contribution to the overall response was so small that it did not produce a change in the calculated value of the MLLD of even one channel. It was thus determined that routine measurement of background was not a productive use of time and the

procedures by which the measurements were processed satisfactorily eliminated all adventitious pulses.

In addition to gamma-rays and background, the radiation in the Pb tube comprises neutrons of energies up to approximately 6 MeV, 67.8% of which have energies below 1 eV as described in section 4.5.6. The DHS neutron detection criterion $\varepsilon_{abs\,n}$ discussed in Chapter 1 does not specify that the detected neutrons must be in the thermal energy range. It only requires that a specific fraction of the total number of neutrons emitted by the source are detected. The ^{6}Li neutron capture cross section decreases with increasing neutron energy, with the exception of an absorption resonance at approximately 250 keV.[11] Incorporating neutrons of higher energies into the neutron fluence reduces the probability that detection of the neutrons will occur as a result of capture by ^{6}Li. Rather, fast neutrons are primarily detected in scintillators as a result of elastic collisions with hydrogen atoms which generate recoil protons that deposit energy in the surrounding matrix by the mechanisms described for heavy ions in sections 2.1. and 3.4.3. By setting the MLLD to the predetermined value, the total neutron count rate recorded in the Pb tube is not appreciably affected by the rate of misclassification of gamma-rays, background, or electronic noise because the combined error from these sources is much smaller than the inherent error due to counting statistics. The additional counts in the Pb tube relative to the Pb – Cd subtraction are thus primarily due to pulses generated as a result of proton recoil by fast neutrons and by eliminating the negative error in the neutron count rate associated with the subtraction procedure.

Values for the neutron count rates above the MLLD ($CR_{n>MLLD}$) in the Pb tube for films over the thickness rage 15 – 601 μm are listed in Table 16. These values were used to calculate the absolute neutron detection efficiencies, $\varepsilon_{abs\,n}$, using Equation 30. The error in the values of

$CR_{n>MLLD}$ due to electronic noise and background are $+2.0 \times 10^{-3}$ cps for the 15 μm film and $+4.0 \times 10^{-4}$ for the 25 μm film, corresponding to errors in the values of $\varepsilon_{abs\,n}$ of $+3.34 \times 10^{-9}$ and $+6.69 \times 10^{-10}$, respectively, and decreasing thereafter for thicker films. It is evident from the data shown in Table 16 that the values reported for $\varepsilon_{abs\,n}$ for all the films are below what is specified by the DHS criterion, $\varepsilon_{abs\,n} = 1.2 \times 10^{-3}$. The absolute neutron detection efficiency is dependent on the cross sectional area of the detector whereas the fraction of neutrons passing through the detector that are detected is independent of the cross sectional area of the detector. It was thus thought that the cross sectional area of the detectors could be increased in order to increase the absolute neutron detection efficiencies. To determine if it was possible for any of the films to meet the absolute neutron detection criterion by increasing the cross sectional area, a simplified scaling calculation was performed as shown in Equation 32,

$$\frac{\Omega(DHS)}{\Omega(Lab)} = \frac{\varepsilon_{abs\,n}(DHS)}{\varepsilon_{abs\,n}(Lab)}, \tag{32}$$

where $\varepsilon_{abs\,n}(Lab)$ and $\varepsilon_{abs\,n}(DHS)$ are the absolute neutron detection efficiencies obtained in the irradiator and that required by DHS, respectively, and $\Omega(Lab)$ and $\Omega(DHS)$ are the fraction of neutrons emitted from the source that are intercepted by the detector in the lab and the fraction that must be intercepted at 2 m in order to satisfy the DHS absolute neutron detection efficiency criterion, respectively. These values are listed in Table 16. All the resulting values listed for $\Omega(DHS)$ are greater than 1, indicating that it is not possible to use any of the films to simultaneously satisfy both the absolute neutron detection efficiency and the gamma-ray intrinsic

Table 16. Scaling up PS Films to Simultaneously Satisfy DHS $\varepsilon_{int\,\gamma}$ and $\varepsilon_{abs\,n}$ Criteria

Thickness (μm)	$CR_{n>MLLD}$	$\varepsilon_{abs\,n}$ *(Lab)*	*Ω (Lab)*	$\varepsilon_{abs\,n}$ *(DHS)*	*Ω (DHS)*
15	1.85	3.094×10^{-6}	0.0193826	0.0012	7.518
25	1.94	3.245×10^{-6}	0.0193826	0.0012	7.168
50	8.34	1.395×10^{-5}	0.0199469	0.0012	1.716
150	0.25	4.181×10^{-7}	0.0198313	0.0012	56.924
292	0.47	7.860×10^{-7}	0.0197319	0.0012	30.127
601	0.91	1.522×10^{-6}	0.0195817	0.0012	15.442

efficiency criteria by using a single film layer. The 50 μm thick film gives the smallest value for *Ω(DHS),* indicating that it outperforms all the other films. It should be noted that this calculation oversimplifies the change in geometry. First, the DHS source is moderated by 2.5 cm of HDPE whereas the source in the neutron irradiator is moderated by 5 cm HDPE. This results in a higher average energy for the neutrons in the DHS setup for which the films have a lower detection efficiency. It is also assumed in the calculation that the detector extends across the surface of a sphere 2 m away from the source rather than extending as a flat panel and that the light collection efficiency is unaffected by increasing the detector size, neither of which are completely practical assumptions. However, a more accurate incorporation of any of these factors would further increase the value of *Ω(DHS)*; thus, neglecting these details at this point greatly simplifies the calculation and does not change the overall qualitative conclusions.

By considering that for the 50 μm thick film the value of $\varepsilon_{int,n}$ is 7.13×10^{-4}, scaling up the size of the detector to fit inside the current RPM8 SAIC footprint and implementing a multilayer format this material can satisfy the quantitative RPM detection criteria.[101]

5.4. Poly(styrene-*co*-lithium maleate)

5.4.1. Motivation

As stated in section 3.4.4., a polymer scintillator designed to detect thermal neutrons requires the presence of three components:

- a thermal neutron capture nuclide,
- a mechanically robust polymer that contains aromatic groups to facilitate scintillation, and
- one or more fluors to collect the electronic excitations from the polymer and emit photons in the wavelength region of spectral sensitivity of the light collection device.

Opacity in composites comprising an organic polymer and an inorganic salt is a result of phase-separation of the components. If two components in a composite do not have identical indices of refraction, then fluctuations in homogeneity on the order of tens of nanometers cause visible light to undergo scattering. If the material is optically anisotropic and the inhomogeneities are sufficiently large, then the resulting composite is not transparent and appears white. Due to the difficulty associated with collecting photons emitted from scintillators that are not completely transparent, it was determined that it would be a logical contribution to synthesize a transparent polymer scintillator containing lithium.

To design such a material, it is necessary to prevent phase-separation and agglomeration of the components. If the phases are restricted to molecular size then scattering is negligible and the resulting composite should be transparent to UV and visible light. Immobilization of Li^+ ions

in a polymer matrix can be accomplished by providing chemical bonds between the Li and the polymer chains. Of the available organic functional groups that are capable of bonding with lithium ions, it was determined that the carboxylate-lithium bond is the most stable and possibly the easiest to implement. Several independent reports indicate that poly(styrene-*co*-maleic anhydride) forms an alternating copolymer when synthesized by solution free radical polymerization.[93,114,115] The anhydride groups can be hydrolyzed to form a diacid which can then be titrated with ^{6}LiOH to result in two $^{6}Li^{+}$ ions per repeat unit. The alternating nature of the copolymer should ensure that the size of the styrene regions and ^{6}Li-containing regions are of molecular scale and the bonds provided between the polymer and the ^{6}Li should restrict agglomeration. It should be noted that there is some discrepancy in the literature regarding whether this is truly an alternating copolymer;[116] however, it is assumed in this discussion that the copolymer is primarily alternating in nature. I have previously published much of the work presented in this section.[94] As compared to the previously published work, this dissertation contains a more comprehensive discussion of the synthesis and fluor selection as well as results from powder X-ray diffraction experiments and thermogravimetric analysis.

5.4.2. Synthesis and Chemical Characterizations

The protocols used to synthesize PS-*co*-PMAn and PS-*co*-PLiMAn were described in section 4.4.1. and a detailed discussion of each is presented here. It has been reported that the copolymerization of styrene and maleic anhydride can be conducted by solution polymerization using DMF as the solvent in the presence of a free radical initiator.[93,115] However, all attempts to conduct the polymerization in DMF were unsuccessful and did not produce any polymer of significant molecular weight. After much trial and error, it was determined that a solution of toluene and diethyl ether dissolved both the monomers and the initiator. After removal of a

significant portion of the diethyl ether, the polymerization was conducted by heating the resulting monomer solution to 60°C. After approximately 5 minutes, the solution began to turn cloudy and after approximately 1 hour, the polymerization was at approximately 50% conversion. The copolymer was collected by vacuum filtration and washed with toluene and diethyl ether. The crude product was then dissolved in THF and reprecipitated into diethyl ether to remove residual monomer, then dried to constant weight at 100 Torr, 95°C, over P_2O_5 in a nitrogen atmosphere. Gel permeation chromatography gave molecular weights of the polymer synthesized by this method of M_n = 96,800 g/mol and M_w = 303,700 g/mol. These molecular weights were sufficient to impart adequate mechanical integrity such that thin films could be fabricated without mechanical failure during the film casting and drying procedure.

^{1}H NMR was the initial choice for determination of the composition of the obtained copolymer. The only solvents available that are used for ^{1}H NMR analysis that dissolved the neat copolymer were THF and dimethylsulfoxide (DMSO). Deuterated THF (THF-d_4) is relatively expensive, so the copolymer was dissolved in deuterated DMSO (DMSO-d_6) for ^{1}H NMR analysis. The ^{1}H NMR analysis indicated that both styrene and maleic anhydride were present; however, a quantitative determination of the relative quantities each was not possible due to strong overlap of the DMSO resonances with the maleic anhydride resonances. Attempts at deconvoluting the resonances using the Global Spectral Deconvolution algorithm in MestreNova did not yield satisfactory results. Casting the copolymer from solution and evaporating the solvent resulted in an optically transparent film, so it was inferred that long blocks of either of the monomer units were likely not present. Independent reports in the literature consistently indicate that a copolymer with a 1:1 ratio of styrene to maleic anhydride is produced over a wide range of feed compositions and in a variety of solvents, [93,114-116] so it was assumed that the

composition of the copolymer that was synthesized was a 1:1 ratio of styrene to maleic anhydride.

Synthesis of PS-*co*-PLiMAn from PS-*co*-PMAn initially proved to be somewhat elusive because it was difficult to find a common solvent for both the neat copolymer and the ^{6}LiOH. Of the solvents investigated, the neat copolymer was appreciably soluble only in organic solvents such as DMF, THF, acetone, and DMSO whereas the LiOH was only appreciably soluble in water and methanol. Elucidation of an effective synthetic strategy was also hindered by attempts to duplicate procedures that have been reported in the literature, the results for any of which could not be replicated.[115,117,118]

It was experimentally determined that an aqueous solution if LiOH can tolerate a small amount of THF and a solution of the copolymer dissolved in THF can tolerate a small amount of water, and that greater tolerances for the nonsolvents in both solutions could be achieved at elevated temperatures. It was guessed that the resulting lithiated copolymer would be soluble in water and further assumed that hydrolysis of the maleic anhydride units was likely faster at higher concentrations of LiOH. This indicated that it could be possible to synthesize the lithiated copolymer by dropwise addition of a solution of the copolymer dissolved in THF to an aqueous solution of LiOH at an elevated temperature. This permitted the elucidation of an effective synthetic strategy. An appropriate mass of the polymer was dissolved in THF and in a separate container an appropriate mass of LiOH was dissolved in a volume of water equal to the volume of THF that was used to dissolve the LiOH. The LiOH solution was ultrasonicated to increase the dissolution rate, then heated to 90°C and stirred with a magnetic stir bar. After dissolution, the polymer solution was combined with the LiOH solution by dropwise addition. After adding a few drops of polymer solution, the LiOH/polymer solution lost transparency and became

translucent and slightly white. At this point, the solvent comprised mostly water. Because each component can tolerate only a small quantity of nonsolvent, it was assumed that the loss of transparency was due to precipitated polymer. After a few minutes, the solution became transparent again which indicated that the maleic anhydride units were being hydrolyzed and that the resulting polymer was indeed soluble in water. Further addition of the polymer/THF solution resulted in a similar appearance of cloudiness with each addition requiring a longer time to become transparent. After adding approximately half of the polymer/THF solution, the LiOH-containing solution again lost transparency but it appeared different as compared to the initial change. At this point, the solution was approximately 2/3 water and 1/3 THF. The solubility of the lithiated copolymer in THF was not known at this point. Addition of a small volume of water caused the solution to turn transparent again, so this loss in transparency could be due to nonsolvent-induced precipitation of either the lithiated copolymer or the remaining LiOH. Larger volumes of water require more time to evaporate, so it was reasoned that it would be more efficient to add approximately 25% of the neat copolymer solution dropwise then allow the THF to evaporate from the solution rather than to use large quantities of water to keep the components in solution. This was conducted until all the copolymer solution was added, then the residual copolymer remaining in the beaker was transferred to the solution containing the lithiated polymer by three successive rinses with THF. The resulting solution was dried at 60°C overnight, then placed in a vacuum oven at 100 Torr, 90°C, and in the presence of a sufficient quantity of P_2O_5 to remove additional residual solvents. As predicted, the resulting lithiated copolymer dried as a transparent film.

It was first of interest to determine the degree of lithiation that the copolymer could withstand while still retaining optical transparency. A series of films containing 25%, 50%, 75%,

82.5%, 85%, 90%, and 100% lithiation of the maleic anhydride units was cast from water. After drying, the films at 85%, 90%, and 100% lithiation were cloudy, so the composition of 82.5% lithiation was used throughout all further experiments. On drying, 82.5% lithiation yields a total ^{6}Li loading of 4.36% by mass, assuming all the maleic anhydride units are hydrolyzed. The notation PS-*co*-PLiMAn hereafter refers to the copolymer at 82.5% lithiation with enriched ^{6}Li unless otherwise noted. There are two possible justifications regarding why the copolymer could only withstand 82.5% lithiation. The first is charge repulsion. The Coulomb force between two ions of the same charge is a repulsive interaction. It is possible that at this relative concentration the total magnitude of energy from repulsive Coulomb interactions becomes equal to the reaction energy of deprotonation of the hydrolyzed units and subsequent complexation of the lithium ions. It was thus reasoned that incorporation of lithium beyond this point did not result in the formation of lithium-polymer bonds and the resulting cloudiness was due to large phases of LiOH in the polymer matrix. The other possibility is that the ratio of maleic anhydride to styrene in the copolymer was less than 1:1; however, it is hypothesized that charge repulsion is the dominant mechanism rather than inaccurate copolymer composition. This apparent ambiguity was not resolved during the course of this work.

At this point, the copolymer could be cast from solution to form a rigid film, it contained a neutron capture nuclide, and it contained aromatic groups on the polymer chain. The final component that was required for this copolymer to function as a thermal neutron scintillation detector was a fluor. The requirements for an appropriate fluor are that it must form a transparent solid composite when it is incorporated into the polymer matrix, its absorption spectrum must overlap the emission spectrum of the polymer, and it must emit photons with adequate quantum yield in the wavelength region of PMT spectral sensitivity. In order for the fluor to form a

transparent solid composite with the polymer matrix, solution casting requires the use of a common solvent for both the fluor and the polymer. The dissolution of PS-*co*-PLiMAn in a wide variety of solvents over a range of temperatures was experimentally investigated and the only solvent that resulted in sufficient dissolution was water. This generated an issue because most of the common fluors used in polymer scintillators are insoluble in water. Some water-based large-volume Cerenkov detectors, which are traditionally used in neutrino experiments, require the use of wavelength-shifting fluors such as those desired in this application. Published information regarding the development and implementation of the fluors that are used in Cerenkov detectors is sparse and many of the fluors that are reported are unreasonably expensive.[119] Literature review indicated that 7-amino-4-methyl-2-hydroxyquinoline (trade name carbostyril 124) would be the best choice for use as a water-soluble scintillation fluor in the lithiated copolymer; however, this fluor did not produce a transparent composite with PS-*co*-PLiMAn. It was possible to codissolve PS-*co*-PLiMAn and PPO in some mixed solvents. Water/isopropanol solutions codissolved the lithiated copolymer and PPO over mixed solvent compositions of 7:1 to 5:1. However, on drying the isopropanol evaporated before the water and the PPO precipitated from solution before all the solvent evaporated and the resulting film was opaque. It was then attempted to use an azeotrope such that the composition of the mixed solvent would not change over the course of solvent evaporation. The only appropriate azeotrope that was discovered was a 71.7% solution of *n*-propanol in water. This solution initially dissolved the components but during the course of evaporation the copolymer precipitated from the solution and the resulting film was brittle and opaque. It was then discovered that salicylic acid and its corresponding alkali salts, which are soluble in water, have been reported to function as fluor in some scintillators.[36,120,121] The low quantum yield of salicylic acid for emission from the S_1 state

indicates that its use would likely not result in a material with a high light yield.[122] Incorporation of salicylic acid into the copolymer film resulted in a transparent film so it was selected as the fluor.

The transparency of the film is a result of a negligible degree of optical photon scattering. There are two possible reasons that would manifest in negligible scattering: Either there are crystalline regions in the polymer that have the same refractive index as the polymer or the size of the phases is very small compared to the wavelength of visible light. P-XRD was implemented to determine the presence or absence of crystalline regions in the matrices at 82.5% lithiation (transparent) and 90% lithiation (cloudy) and the resulting diffractograms are shown in Figure 26 and Figure 27, respectively. Crystalline regions are characterized by sharp peaks in p-XRD. The diffractogram of the transparent film shows very broad peaks. The peaks are sharper in the cloudy film, though they are low in intensity. The low intensity of the peaks is likely due to the low relative concentration of the crystalline regions as compared to a crystalline powder for which the experiment was designed to measure. The absence of defined peaks indicates that the transparent film is likely amorphous whereas the presence of defined peaks indicates that the cloudy film possibly contains phase-separated regions with some degree of crystallinity which are likely the source of the cloudiness. It is probable that there is a difference in lithium content between the phases in the cloudy film; however, the diffraction pattern of the opaque film does not exactly match the p-XRD pattern obtained for LiOH, $LiOH \cdot H_2O$, or Li_2CO_3, so it is not expected that the peaks are due to phase separation and crystallization of these pure compounds. Further investigations of the exact composition and degree of crystallinity of the phases in the cloudy film were not performed in this work.

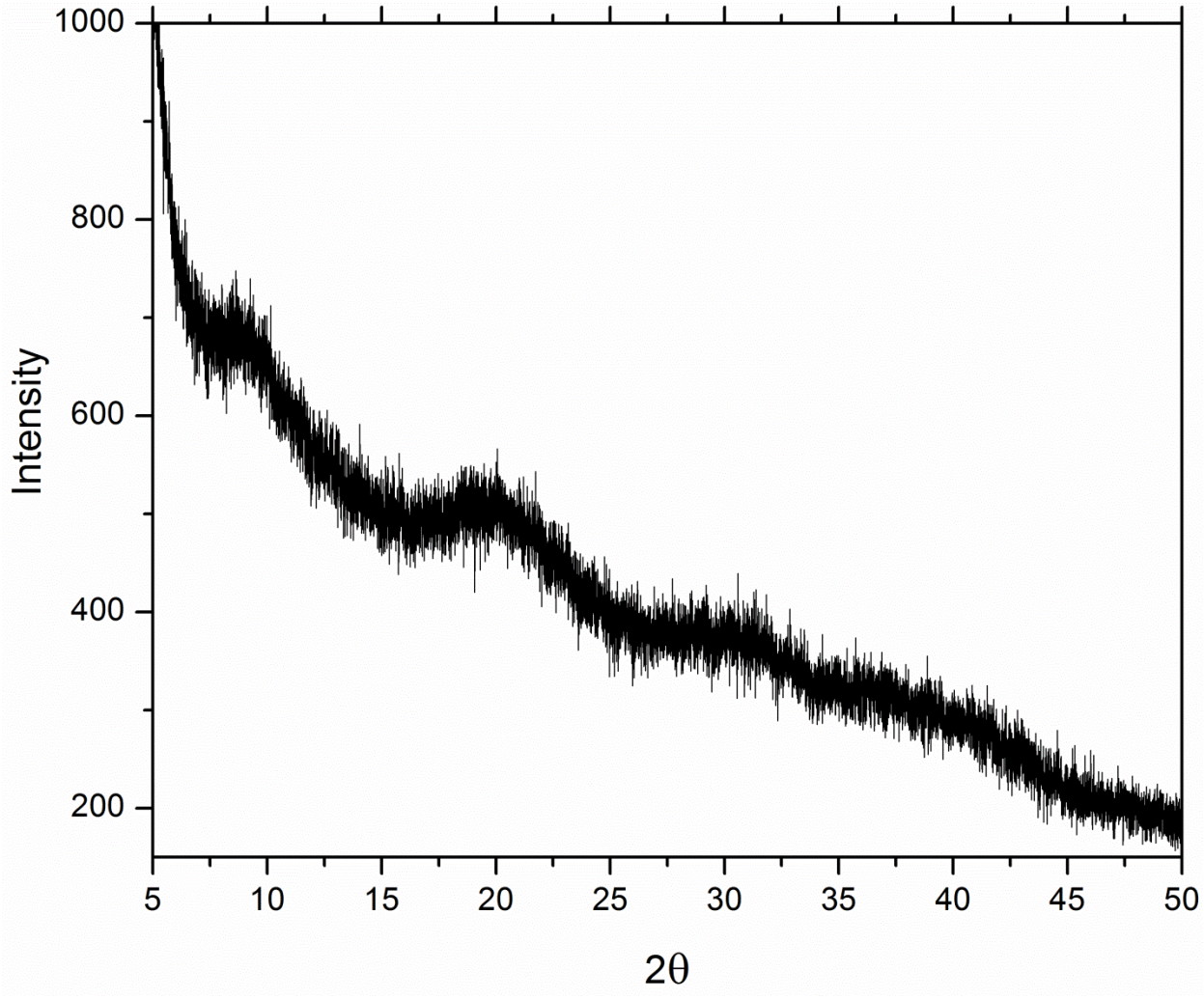


Figure 26. P-XRD Pattern of Transparent PS-*co*-PLiMAn (82.5% Lithiation).

The absence of clear peaks evidences that this material is amorphous. The presence of broad peaks does indicate that some long-range order is present in the material. Acknowledgement: John D. Auxier II for collecting the spectrum.

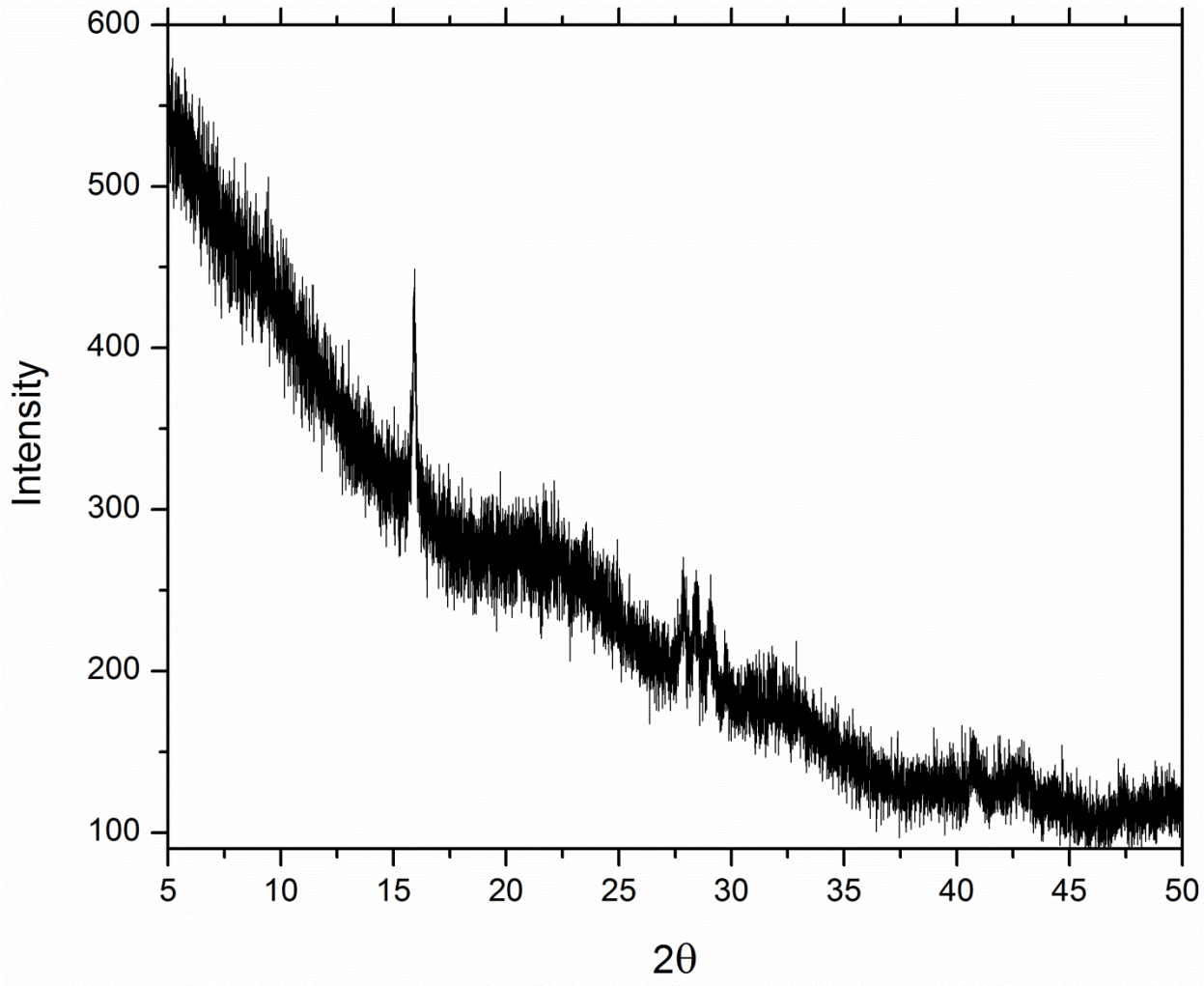


Figure 27. P-XRD Pattern of Cloudy PS-*co*-PLiMAn (90% Lithiation).

Peaks at 2θ values of 15.9, 27.9, 28.4, and 29.0 indicate that partially crystalline regions are possibly present in the sample. Acknowledgement: John D. Auxier II for collecting the spectrum.

Thermogravimetric analysis was performed on a 10.2220 mg sample of PS-*co*-PLiMAn containing 11.6 wt% HSal that was cast from water and dried overnight in ambient conditions in order to determine the maximum temperature at which the solvent could be removed from solvent-cast films without decomposing any of the vital components. The sample was heated in a platinum crucible at a rate of 10°C/min in air. The resulting thermogram, shown in Figure 28, is very similar that of hydrolyzed PS-*co*-PMAn.[123] Three points of interest are labeled on the thermogram which divide the spectrum into four distinct regions, labeled $R_{1–4}$. Region 1 (R_1) is characterized by a change in mass of –2.2110 mg. This is attributed to liberation of residual water and dehydration of untitrated maleic acid subunits. Region 2 (R_2) is characterized by a change in mass of –0.8944 mg. By considering that both salicylic acid and maleic acid are weak acids, it can be expected that acid/base equilibrium exists between them. It has been reported that LiSal (natural isotopic abundance) loses approximately 68.8% of its mass in the temperature range characterized by R_2.[124] The sample contains 11.6% HSal, which corresponds to a total mass of 1.1858 mg, as calculated from the mass of material remaining at the onset of R_2. If all the HSal were converted to ^{6}LiSal, it would result in a total of 1.089 mg ^{6}LiSal in the sample. The change in mass in R_2 is –0.8944 mg, which is 82.1% the projected mass of ^{6}LiSal in the sample. The change in mass in R_2 is thus attributed to the partial decomposition of ^{6}LiSal and partial decomposition of untitrated MAn groups.[123] Region 3 (R_3) is characterized by a change in mass of –4.0428 mg. This is attributed to decomposition of the polymer and of the fluor. Region 4 (R_4) is characterized by a stable mass of 3.0738 mg which comprises the polymer and fluor residue remaining from the decomposition. Due to the presence of carboxylate groups in the material and carbon dioxide in the air, it is expected that a significant portion of the ^{6}Li in R_4 is in the form of $^6Li_2CO_3$.

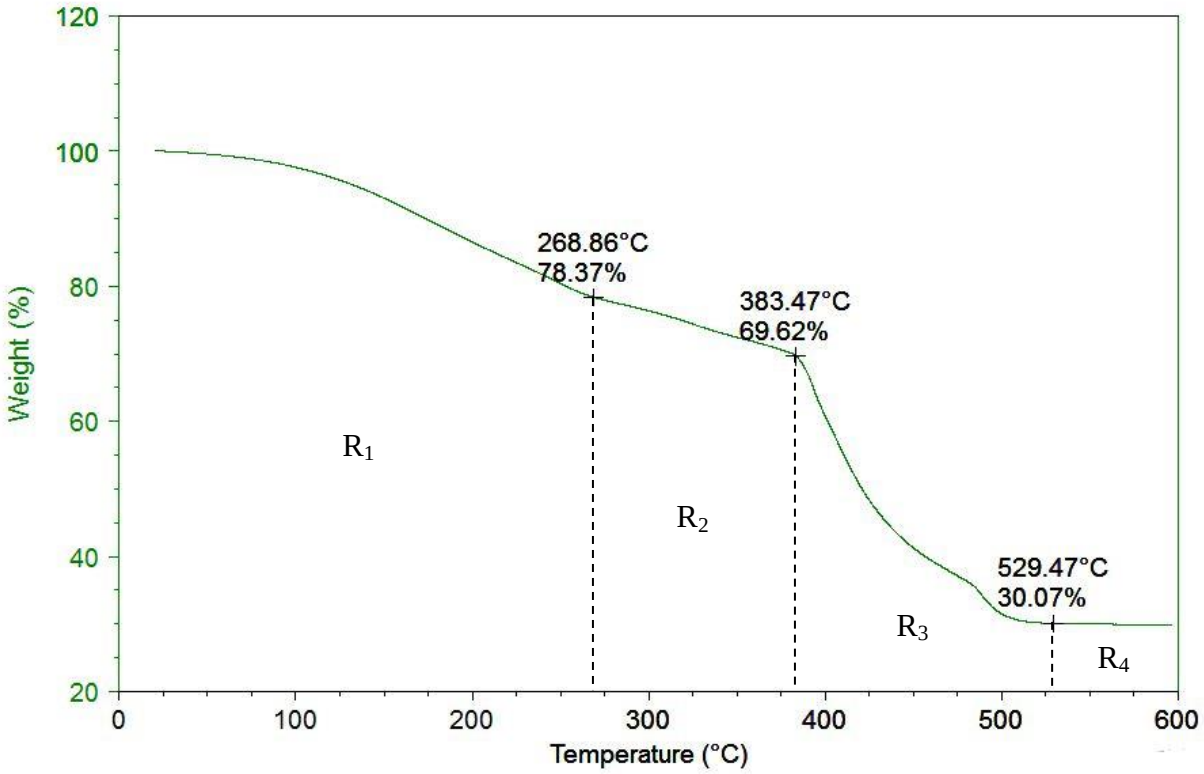


Figure 28. Thermogravimetric Analysis of PS-*co*-PLiMAn Containing 11.6% HSal.

The sample was heated at 10°C/min in air. The initial mass of sample was 10.2220 mg. The four regions are labeled as R_1, R_2, R_3, and R_4.

5.4.3. Optical Transmission and Fluorescence

An image of a PS-*co*-PLiMAn film containing 11.6% HSal 183 μm thick is shown in Figure 29. This image demonstrates that the film is optically transparent in the visible wavelength range. To quantify the transparency in the visible region and to determine the extent of transparency into the UV region, the transmission spectrum was measured using an optical absorbance spectrometer over the wavelength region 200 – 600 nm. The resulting transmission spectrum is shown in Figure 30. The cutoff wavelength at 360 nm is marked on the spectrum with a blue star. The average percent transmission between 360 and 600 nm was 78.5%. It was difficult to mount the film in an ideal manner in the apparatus using the available equipment and the measurement was taken such that the photons were not exactly normal to the film surface. Though the refractive index of the film was not measured, it is suspected that it is much different than air. This implies that refraction can occur when the photons enter and leave the film. Because the photons were not exactly normal to the surface of the film, this refraction could result in a reduction in the number of transmitted photons that are detected by the photon detector in the instrument. Thus, it is suspected that the actual transmission of the film is higher than what is shown in the transmission spectrum.

Photoluminescence spectra are shown in Figure 31. The wavelength of maximum excitation for neat PS is at 278 nm and the wavelength of maximum emission is at 314 nm with a quantum yield for fluorescence (φ_f) of about 16%.[41] HSal has an emission wavelength at 450 nm (φ_f = 2%) whereas the salicylate ion (Sal^-) has an emission wavelength at 408 nm (φ_f = 36%).[122] The photoluminescence experiment was designed to excite the styrene subunits and record emissions at 314 nm, 408 nm, and 450 nm in order to determine the relative amounts of light emitted from styrene, Sal^-, and HSal, respectively. The photoluminescence spectra demonstrate

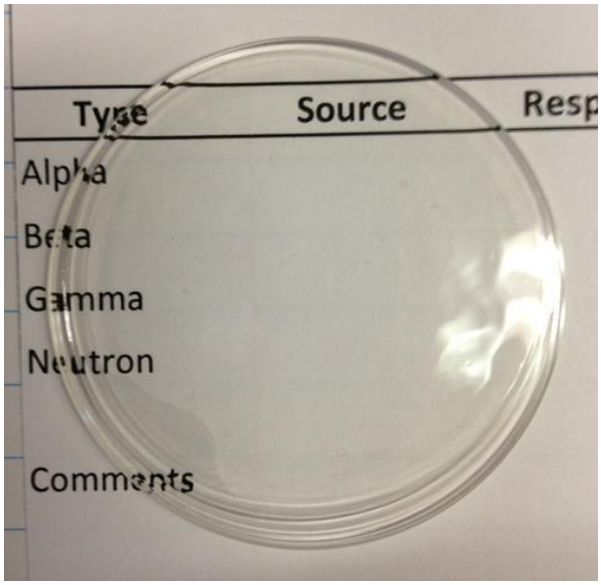


Figure 29. Transparent PS-*co*-PLiMAn Film Containing 11.6% HSal by Mass.

The film thickness is 183 μm. The film is placed on a card containing text to illustrate the optical clarity.

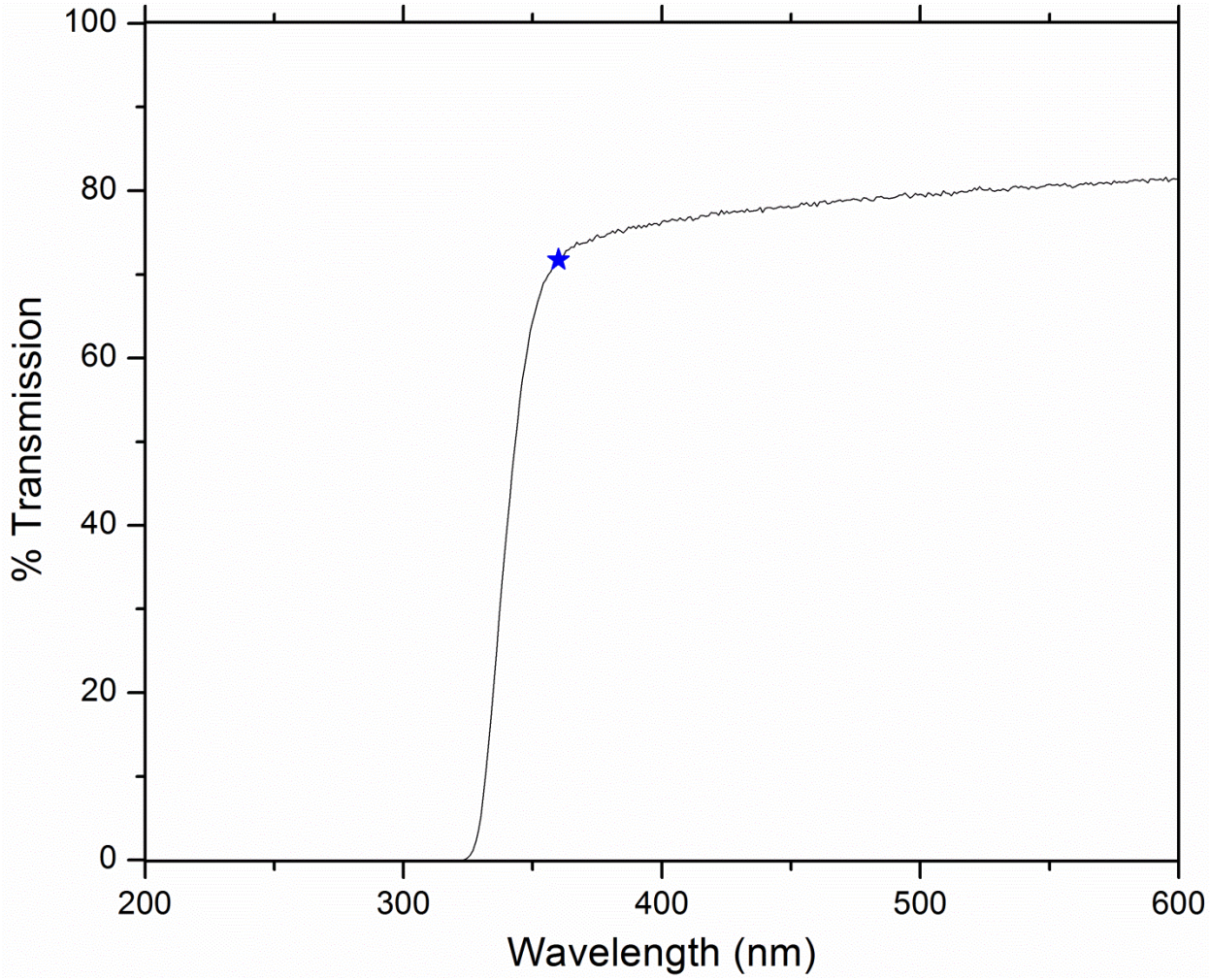


Figure 30. Transmission Spectrum of a PS-*co*-PLiMAn Film Containing 11.6% HSal.

The film is 183 μm thick. The blue star indicates the cutoff wavelength at 360 nm.

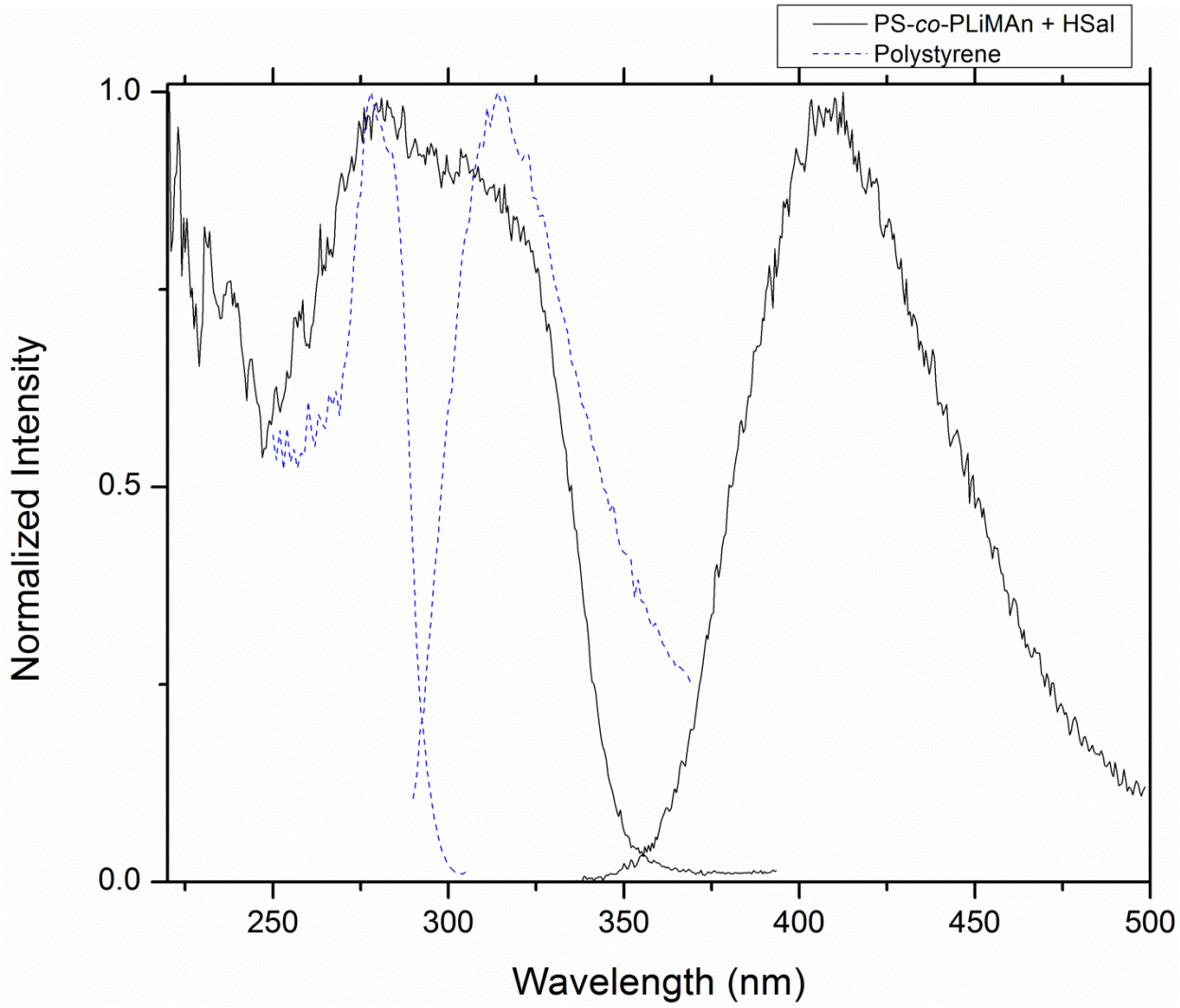


Figure 31. Photoluminescence Spectra of PS and PS-*co*-PLiMAn Containing 11.6 wt% HSal. The black lines are the excitation and emission spectra of PS-*co*-PLiMAn containing 11.6 wt% HSal. The blue dotted lines are the excitation and emission spectra of PS which are shown to demonstrate that the styrene subunits in the copolymer are the excited entities.

that the wavelength of maximum excitation intensity is at 278 nm, indicative of styrene excitation. When excited at 278 nm, the primary emission wavelength is at 408 nm and emissions at 314 nm (styrene) and 450 nm (HSal) are essentially absent. The absence of emission at 314 nm and the increased level of the excitation spectrum in this region relative to PS indicates that the excitations on the styrene subunits are completely collected by the fluor. The emission peak at 408 nm and the absence of an emission peak at 450 nm indicates that Sal^- is the primary emitter rather than HSal. Previous experiments indicated that the emission characteristics of Sal^- and LiSal are nearly identical. By considering that the acid form of the polymer and HSal are both weak acids that are subject to acid-base equilibrium, the emission results indicate that some of the lithium ions have been removed from the maleate groups by HSal resulting in maleic acid and LiSal. This supports the conclusion derived from the TGA analysis. At 82.5% lithiation and 11.6% salicylic acid, the molar ratio of Li^+ ions to salicylic acid is approximately 8.6; thus, even if the HSal were to be completely converted to LiSal, the majority of the Li^+ ions would still be associated with the polymer chain.

To determine the concentration of HSal required to obtain the maximum fluorescence yield, a series of PS-*co*-PLiMAn films containing 2% – 26% HSal was fabricated and the fluorescence emission of each film was measured. Each film was excited at 278 nm and the resulting emission spectrum was integrated from 390 – 450 nm to obtain a value proportional to the number of photons emitted from each film by the fluor in the region of spectral sensitivity of the PMT, then normalized to the emission area of the film giving the largest integrated emission intensity. The shape of the emission curves were nearly identical for all concentrations of HSal. The integrated emission intensities for the concentrations of HSal measured are shown in Figure 32 and indicate that increasing the amount of HSal initially increases the fluorescence response

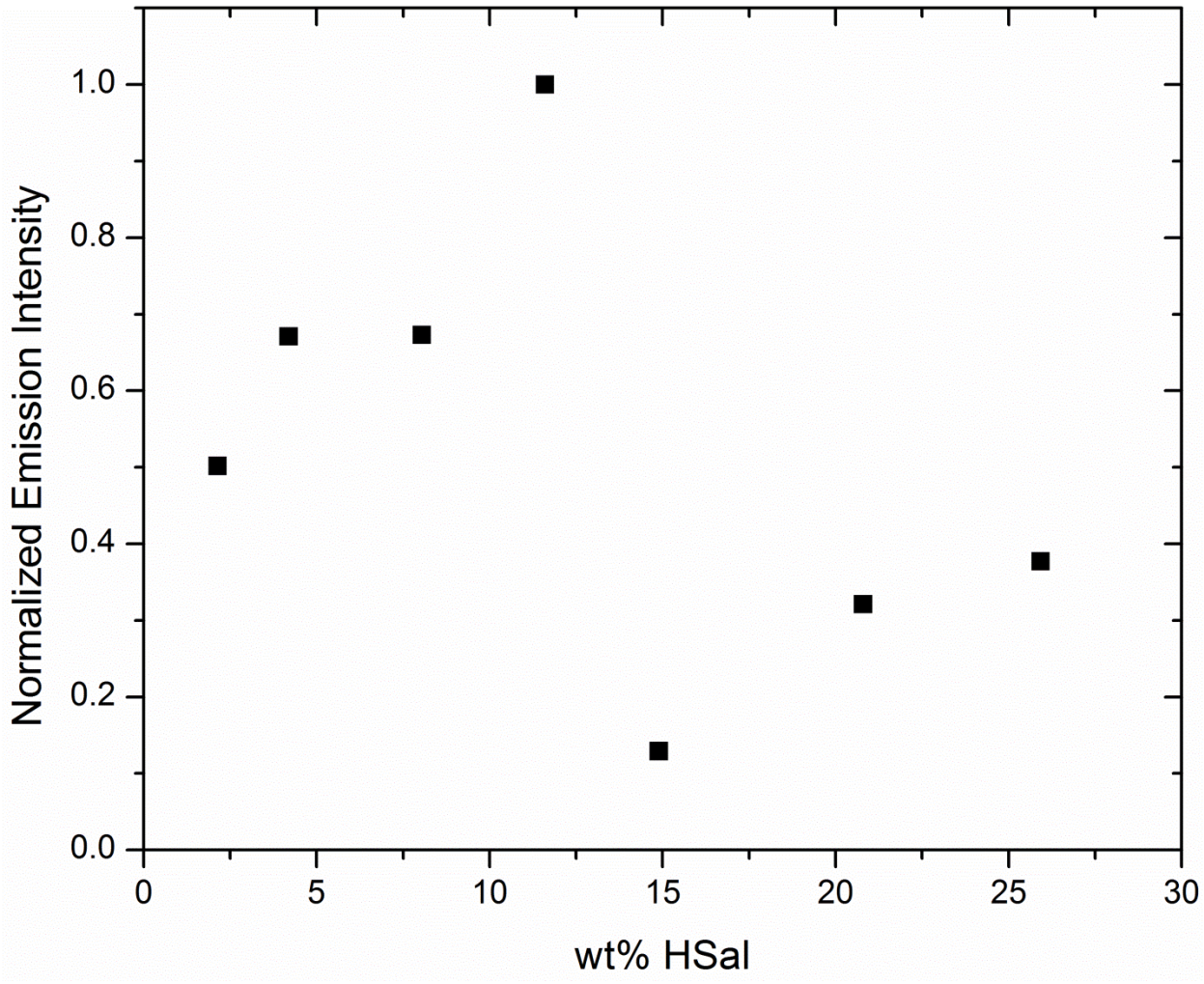


Figure 32. Integrated Fluorescence Emission Intensity as a Function of Wt% HSal.

The excitation wavelength was at 278 nm and the emission intensities were integrated from 390 – 450 nm. Spectra were obtained from free-standing films without any substrate.

up to 11.6%, after which the emission intensity is significantly reduced. This can be reasoned by considering that the primary emission is from Sal^-. It is presumed that at and below 11.6%, the primary fluorescent component is the Sal^- ion, most likely in the form of LiSal. Above 11.6%, acid/base equilibrium between the HSal and the maleic acid becomes important and some of the LiSal is converted to HSal. The quantum yield for fluorescence of HSal is much lower than that of Sal^-, resulting in a reduction in the overall emission intensity. Incorporation of 11.6% HSal into the PS-*co*-PLiMAn film results in a material that is 3.91% ^{6}Li by mass. This analysis also supports the previously determined conclusion from the initial photoluminescence experiment and from TGA that the primary fluorescence emitter is LiSal.

5.4.4. Scintillation

The discussion in section 5.3.3. indicated that the optimum film thickness for neutron/gamma-ray discrimination in PS-based films was 50 μm. However, films of PS-*co*-PLiMAn containing 11.6% HSal in the thickness range of 50 – 150 μm cracked and were thus not useful for this application. A film with thickness 183 μm dried as a single piece so this thickness was used for scintillation measurements.

The alpha response from ^{241}Am is shown in Figure 33. The peak is at channel 441. Multiplying this value by 0.846 photons/channel gives 373 photons, indicating that an average of 373 photons are collected from each alpha event. The beta response from ^{36}Cl is shown in Figure 34. The spectral average is at channel 165 and the endpoint is at channel 310, indicating that an average of 139 photons are collected per beta event and a maximum of 262 photons are collected per beta event. It is difficult to estimate a pulse height deficit for this material from this data because the film of interest was fabricated to be 183 μm thick which is thick enough to stop the

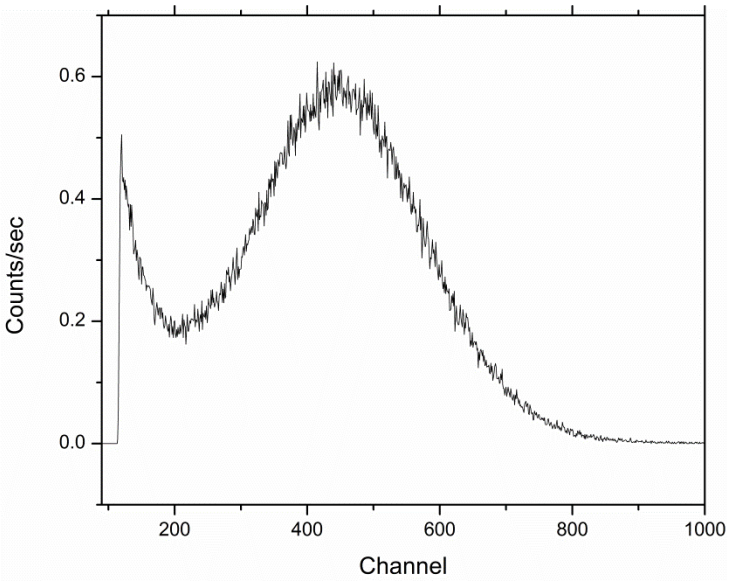


Figure 33. ^{241}Am Alpha Response for PS-*co*-PLiMAn Containing 11.6 Wt% HSal.

The peak is at channel 441, indicating that the material emits an average of 373 photons per incident alpha particle. The count time was 600 seconds.

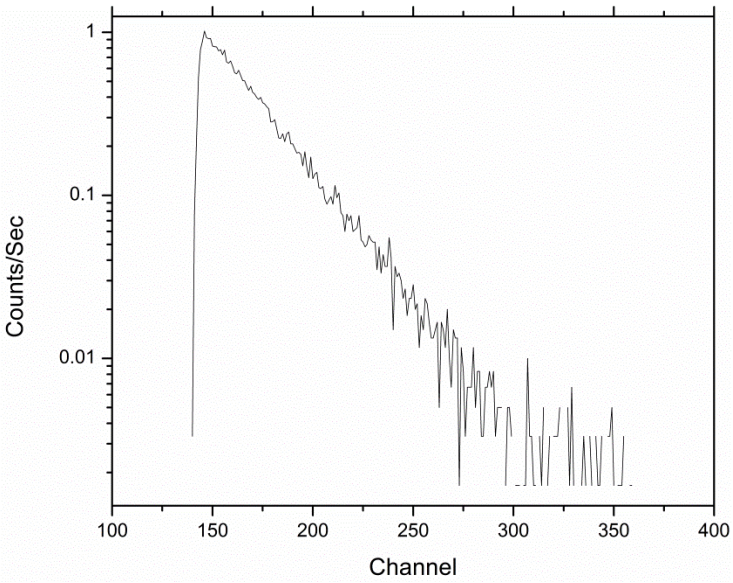


Figure 34. ^{36}Cl Beta Response for PS-*co*-PLiMAn Containing 11.6 wt% HSal.

The y-axis is on a log scale to improve the visibility of the endpoint. The spectral average is at channel 165 and the endpoint is at channel 310, indicating that the material emits an average of 139 photons and a maximum 262 of photons per incident beta particle. The count time was 600 seconds.

alpha particles but not thick enough to permit complete energy deposition from the ^{36}Cl beta particles.

The intrinsic gamma-ray efficiency and the thermal neutron count rate spectrum against MLLD are shown in Figure 35. The average of the thermal neutron spectrum indicates that the material emits approximately 250 photons per neutron capture event. The intrinsic efficiency for gamma-rays reaches 10^{-6} at channel 466. Above this discriminator setting, the film gives 10.8 counts per second for thermal neutrons. A summary of the light yields and discrimination data for this material and for a PS film is listed in Table 17. It should be noted that the PS-*co*-PLiMAn film is 183 μm thick whereas the PS film is 50 μm thick; thus, a direct comparison of material properties is not shown in Table 17. The thinnest film that could be fabricated from PS-*co*-PLiMAn that did not result in mechanical failure was the 183 μm thick film. It was demonstrated in section 5.3.3. that a 50 μm thick film demonstrates the optimum performance for neutron/gamma-ray discrimination and that increasing the thickness above this value results in markedly poorer discrimination characteristics. Thus, the data in Table 17 illustrate a comparison of the best performing films of PS and PS-*co*-PLiMAn in terms of neutron/gamma-ray discrimination. By considering that the value of $\varepsilon_{int,n>MLLD}$ for this material is 9.32×10^{-4}, this material can be scaled up to fit inside the current RPM8 SAIC footprint and by implementing multilayer format will satisfy the detection criteria.[101]

5.5. Poly[styrene-*co*-lithium maleate-*co*-2-phenyl-5-(4-vinylphenyl)oxazole]

5.5.1. Synthesis and Chemical Characterizations

The syntheses of the polymerizable fluor VPPO, the terpolymer PS-*co*-PMAn-*co*-PVPPO, and the corresponding lithiated terpolymer PS-*co*-PLiMAn-*co*-PVPPO were described

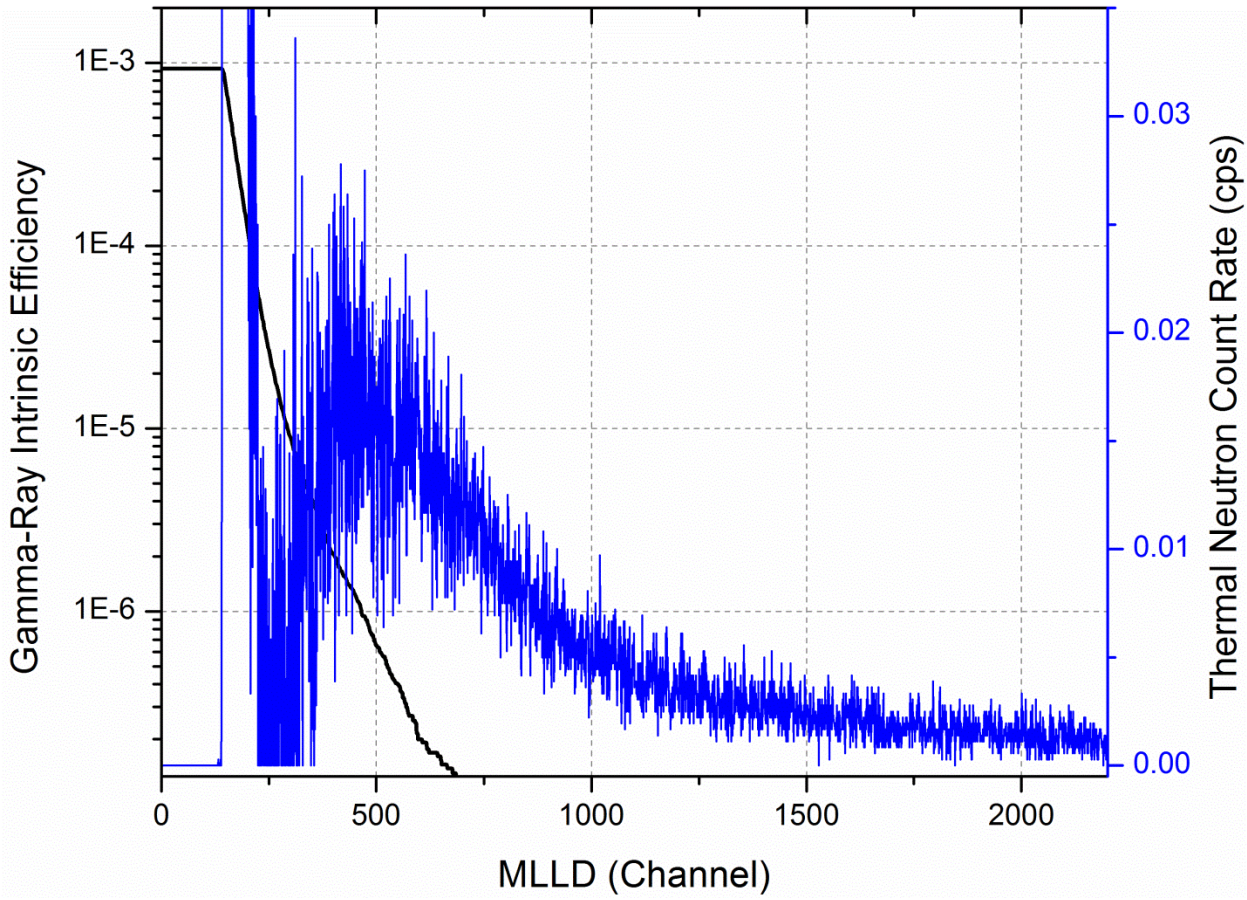


Figure 35. ^{252}Cf Thermal Neutron Count Rate Spectrum and Gamma-Ray Intrinsic Efficiency versus MLLD for PS-*co*-PLiMAn Containing 11.6 Wt% HSal.

The MLLD is at channel 466, above which the thermal neutron count rate is 10.8 cps.

Table 17. Light Yields and Neutron/Gamma-Ray Discrimination of PS and PS-*co*-PLiMAn Films

Polymer	PS	PS-co-PLiMAn
wt% ^{6}Li	10% ^{6}LiF	3.91% ^{6}Li
Fluor(s), wt%	PPO/POPOP, 5.0%	HSal, 11.6%
Thickness	50 μm	183 μm
^{241}Am LY	5637	373
^{36}Cl LY	2310	139
Pb LY	647	115
Pb – Cd LY	1864	250
^{60}Co LY	312	165
$\varepsilon_{int\ n,th}$*	0.03%	0.04%
MLLD	1894	466
$CR_{n,th>MLLD}$	7.77 cps	10.8
$CR_{n>MLLD}$†	8.34 cps	10.9
$\varepsilon_{abs\ n}$†	1.395×10^{-5}	2.1×10^{-5}
$<LY_{n>MLLD}>$†	2358	295

Light yields are listed as photons per particle and were calculated from spectral averages based on GS20 emitting 6,250 photons/neutron.

*Intrinsic thermal neutron detection efficiency for all thermal neutron pulses.

†Listed values are for responses in the Pb tube ignoring all pulses below the MLLD.

in section 4.4.2 and additional details regarding the lithiation procedure are given in this section. Because the exact values for the reactivity ratios of VPPO with styrene and MAn were not known, it was assumed that VPPO would react preferentially with styrene over MAn. Thus, an excess of MAn was added to the feed solution to give a total of 10.8 mmol MAn and a combined amount of 7.62 mmol styrene and VPPO. The molecular weights of the resulting terpolymer, as determined by gel permeation chromatography (GPC) against PS standards in THF, were M_N = 88,400 g/mol; M_W = 492,400 g/mol; and PDI = 5.57.

The presence of styrene, MAn, and VPPO could be detected in the ^{1}H NMR spectrum of the terpolymer dissolved in DMSO-d_6; however, quantitative determination of the composition by was not possible due to significant overlap of the MAn resonances with the solvent resonances as well as overlap of styrene resonances with VPPO resonances. After drying the terpolymer under high vacuum at 90°C over P_2O_5, a small sample was sent to Atlantic Microlab, Inc. in Norcross, GA for elemental analysis, the results from which are shown in Table 18. The reported values are mass percentages for carbon, hydrogen, and nitrogen and are averages of duplicate analyses. It was known from the ^{1}H NMR analysis that the polymer contains maleic anhydride which imparts the presence of oxygen. The analytical solution for the values reported in the elemental analysis indicates that the polymer contains 65.6% styrene, 16.6% maleic anhydride, and 7.42% VPPO. Incorporating the corresponding amount of oxygen from 16.6% MAn and 7.42% VPPO and solving indicated that 8.59% of the mass is oxygen. Adding the relative weight fractions of carbon, hydrogen, nitrogen, and oxygen gives a total of 89.38% which indicates that the remaining 10.62% comprises atoms other than carbon, hydrogen, nitrogen, or oxygen. It was suspected that the synthesized terpolymer did not contain that many

Table 18. Elemental Analysis of PS-*co*-PMAn-*co*-PVPPO

Element	*wt%*
Carbon	74.78%
Hydrogen	5.59%
Nitrogen	0.42%
Oxygen	Not Measured

impurities, especially because the terpolymer could be cast from solution to result in a transparent film and if 10.62% of the mass were due to atoms other than carbon, hydrogen, nitrogen, and oxygen, then it is likely that this amount of impurities would result in a cloudy film. It is known that polymers containing maleic anhydride readily absorb water from the atmosphere. By assuming that the only components in the sample were styrene, MAn, VPPO, and water, the composition was recalculated for various mass percentages of oxygen, of which the minimum was 8.59% and the maximum was 19.21%. There existed a unique solution for all 4 components at each oxygen concentration and the calculated values are listed in Table 19.

The elemental analysis shows a large variation in the possible weight fractions of each component in the terpolymer and in order to use the polymer in the most effective manner, a more precise solution was desired. In order to determine the concentration of water in the material, TGA was implemented. The material was heated from room temperature to 600°C at a rate of 20°C per minute under a nitrogen atmosphere and the resulting thermogram is shown in Figure 36. Thermogravimetric analysis of pure PPO indicated that at the onset of decomposition, 1% of the mass was lost at a temperature of 131.1°C. It is expected that the thermal stability of polymerized PPO is somewhat better than that of pure PPO, so it is reasonable to assume that below this temperature the only compound liberated from the terpolymer was water. An

Table 19. Possible Compositions of PS-*co*-PMAn-*co*-PVPPO Containing Water over the Range of Possible Oxygen Content (wt%)

Oxygen	*H_2O*	*Styrene*	*MAn*	*VPPO*
8.59%	0.00%	65.6%	16.6%	7.42%
10.00%	0.37%	64.4%	18.8%	7.42%
15.00%	1.68%	60.3%	26.6%	7.42%
17.41%	2.31%	58.27%	30.4%	7.42%
19.21%	2.78%	56.8%	33.2%	7.42%

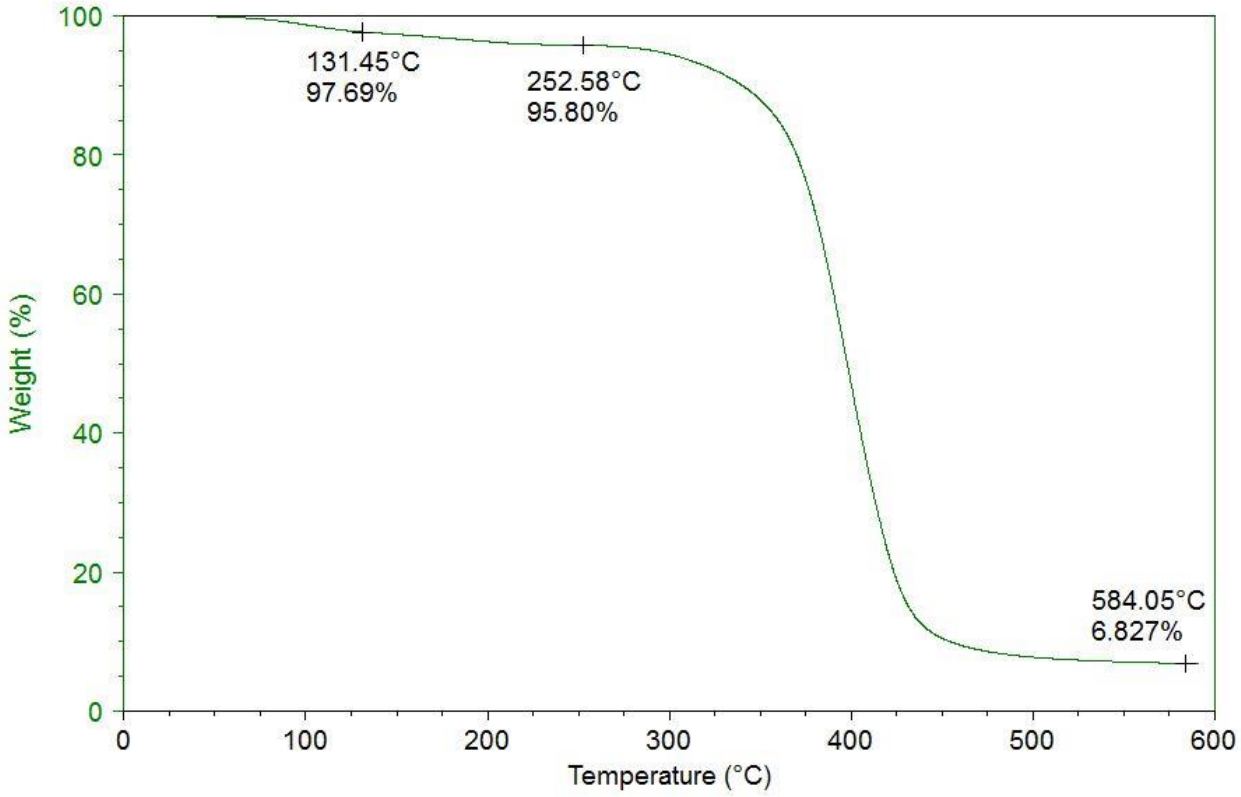


Figure 36. Thermogravimetric Analysis of PS-*co*-PLiMAn-*co*-PVPPO.

The sample was heated from room temperature to 600°C at 20°C per minute under nitrogen. The initial sample mass was 5.6630 mg.

expanded view of the thermogram of the terpolymer between the temperatures of 35°C and 290°C is shown in Figure 37. At a temperature of 131.45°C, the material has lost 2.31% of its mass. The presence of somewhat of a local maximum in the slope at this point and a decrease in slope thereafter indicates that the assumption to use this point as a reference is probably valid and that at temperatures above 131.45°C it is possible that some of the VPPO is decomposing. This permits an upper limit on the mass of water liberated from the film to be 2.31%. Using this value, the resulting calculated values for the sample sent for elemental analysis are that the sample was 2.31% water, 58.27% styrene, 30.40% MAn, and 7.42% VPPO and the total oxygen content was 17.41%. There is not a clear plateau in the thermogram so this is a lower limit to the amount of water in the sample. Thus, eliminating water from the calculation, the composition of the terpolymer that was synthesized in mass percentages and in mole percentages is shown in Table 20. Though the proportion of maleic anhydride in the terpolymer was not as high as desired, the amount of VPPO in the terpolymer was in the linear range of corresponding to the maximum obtainable fluorescence yield as determined in section 5.3.2.

After the composition of the neat terpolymer was determined, it was necessary to incorporate lithium into the material. It was first attempted to lithiate the terpolymer following the same procedure as that for PS-*co*-PLiMAn in which a solution of the polymer in THF was added dropwise to an aqueous solution of LiOH. This solution turned clear after time, indicating that the hydrolysis and titration of the MAn groups had occurred. However, after the THF evaporated a precipitate formed and the addition of more THF did not result in dissolution. The cloudy solution was cast onto a substrate and the solvent was evaporated which resulted in a cloudy film. In order to fabricate a transparent composite, all components must be solvated during the casting procedure. It was determined experimentally that the resulting film was

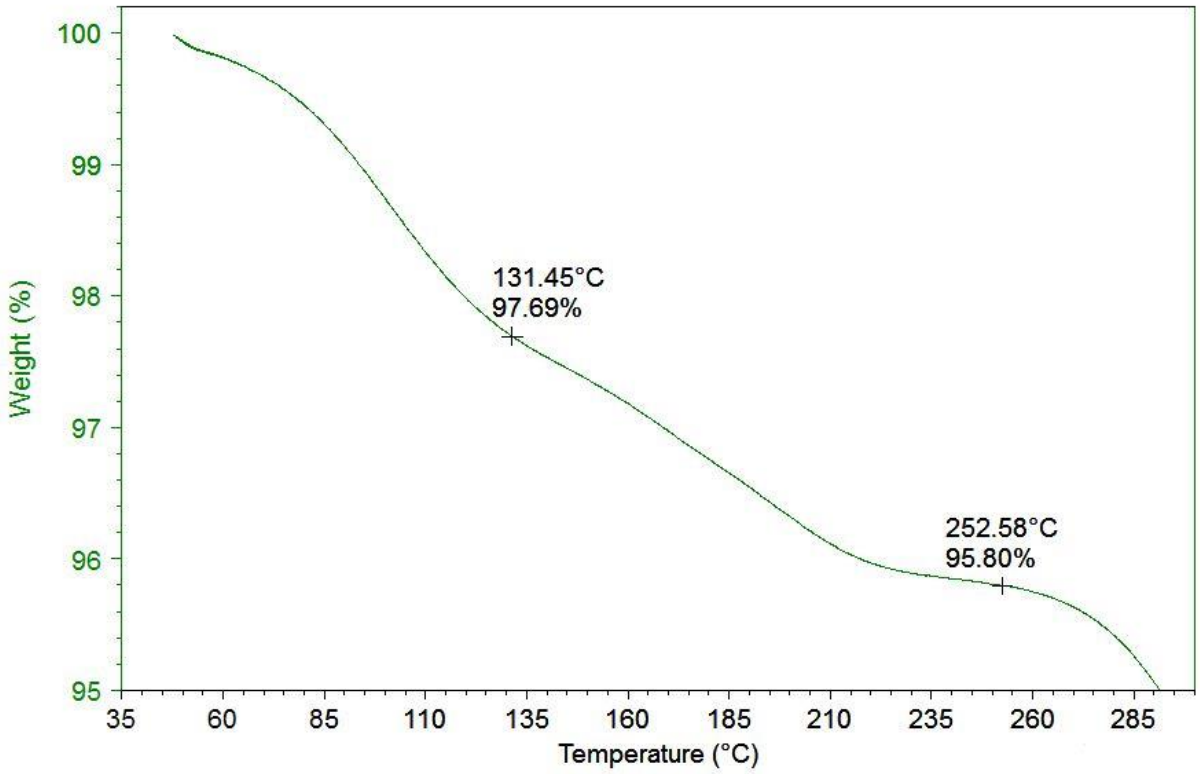


Figure 37. Thermogravimetric Analysis of PS-*co*-PLiMAn-*co*-PVPPO Expanded over the Temperature Range 35 – 290°C.

Table 20. Composition of PS-*co*-PMAn-*co*-PVPPO

Component	*wt%*	*mol%*
Styrene	60.64%	62.18%
MAn	31.64%	34.47%
VPPO	7.72%	3.34%

soluble in DMF, DMSO, and methanol and insoluble in acetone, THF, water, ethanol, *n*-propanol, and isopropanol. It was decided that methanol was not the best option due to the possibility of condensation of the methanol with the maleic acid. DMF was selected over DMSO because DMF has a lower boiling point which indicates that it evaporates more quickly. The synthetic strategy implemented was thus to dissolve the terpolymer in DMSO, then add an aqueous solution of ^{6}LiOH dropwise to the polymer solution. The volume ratio of water to DMF was 1:4 and the ^{6}LiOH solution was added dropwise to the polymer solution in order to prevent precipitation of the polymer. The solution remained clear during the entire course of this procedure. After stirring at 90°C for one hour, the solution was pipetted onto an acrylic disk, covered with a beaker, and heated to 75°C to evaporate the solvent. The film was then placed in a vacuum oven at 65°C over P_2O_5 with flowing nitrogen overnight to evaporate the remaining solvent. An image of the resulting film mounted on an acrylic disk is shown in Figure 38.

5.5.2. Transmission and Fluorescence

The percent transmission spectrum of PS-*co*-PLiMAn-*co*-PVPPO mounted on an acrylic disk is shown in Figure 39. The cutoff wavelength is at 380 nm and is shown as a blue star. The average percent transmission over the wavelength range 380 – 800 nm is 72.2%.

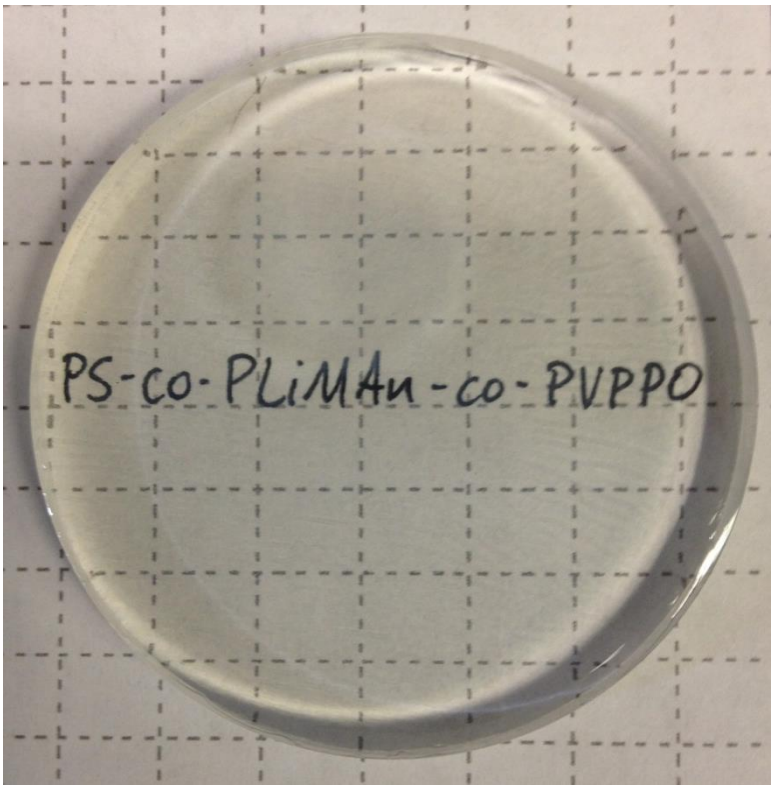


Figure 38. Image of PS-*co*-PLiMAn-*co*-PVPPO Film Mounted on an Acrylic Disk.

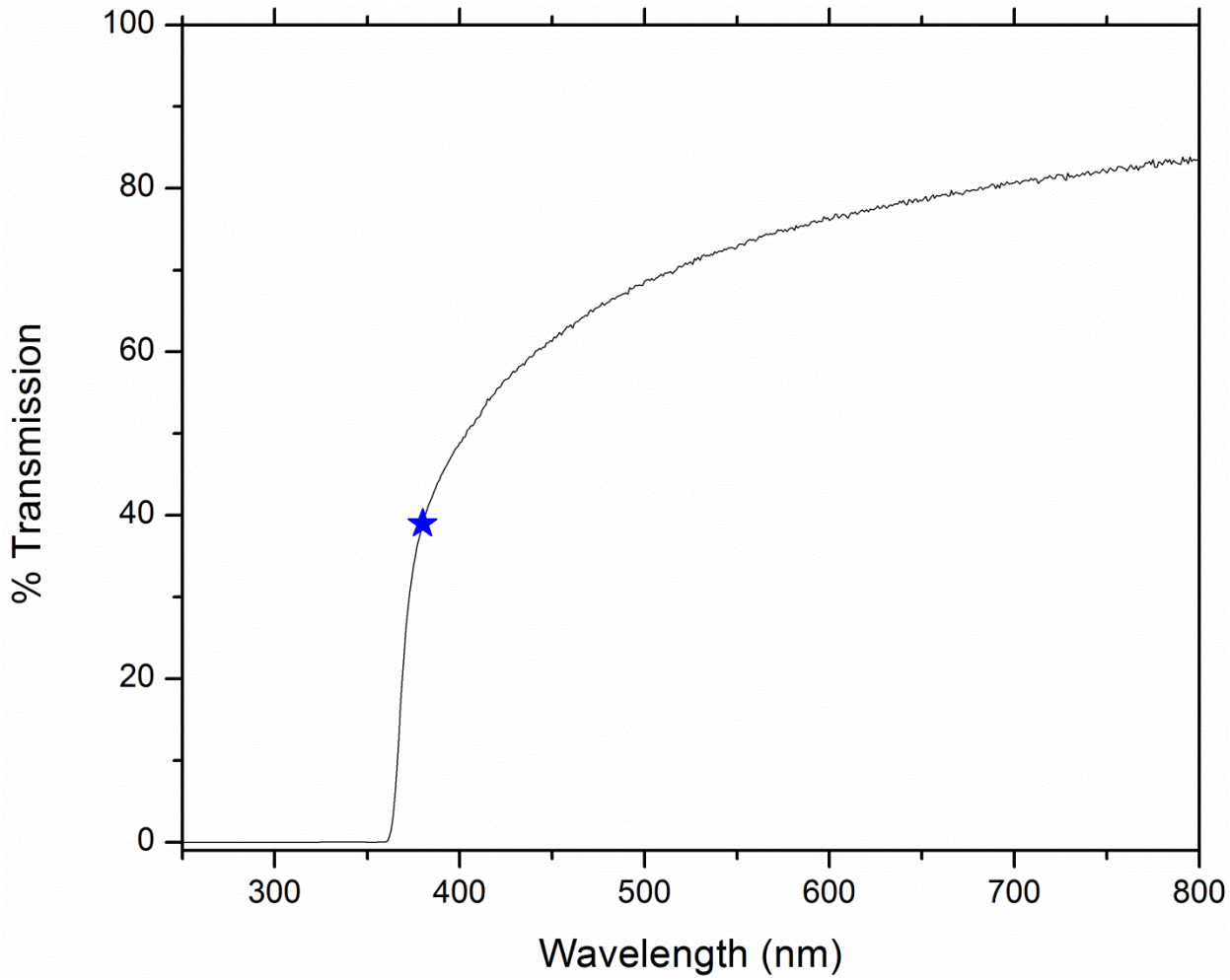


Figure 39. Percent Transmission Spectrum of PS-*co*-PLiMAn-*co*-PVPPO Mounted on an Acrylic Disk.

Photoluminescence spectra of a film of PS-*co*-PLiMAn-*co*-PVPPO and of PS are shown in Figure 40. The wavelength of maximum emission is at 399 nm which, by comparison to PPO, is what should be expected from VPPO. There are two peaks in the excitation spectrum, one at 278 nm and one at 352 nm. The peak at 352 nm is attributed to excitation of VPPO, which is what was expected by comparison to PPO. The peak at 278 nm is attributed to styrene excitation, which is supported by the presence of the same peak in the excitation spectrum of styrene. As expected from the discussion regarding the photoluminescence spectra of PS containing PPO/POPOP, the amount of VPPO in the terpolymer is adequate to reduce the integrated emission intensity in the region 290 – 330 nm due to styrene down to a negligible value which indicates that the excitations from the styrene subunits are collected by the VPPO subunits.

5.5.3. Scintillation

By synthesizing this terpolymer, it was intended to improve the light yields and discrimination characteristics as compared to PS-*co*-PLiMAn containing HSal. Plots of gamma-ray intrinsic efficiency and thermal neutron count rate against MLLD for a 50 μm thick film of the terpolymer are shown in Figure 41. The MLLD is at channel 469, giving a value of $CR_{n>MLLD}$ of 10.8 cps, corresponding to a value for $\varepsilon_{abs\ n}$ of 2.28×10^{-5}. Relevant values for light yields and discrimination characteristics of PS, PS-*co*-PLiMAn + 11.6% HSal, and PS-*co*-PLiMAn-*co*-PVPPO are listed in Table 21. The data indicate that although the light yields of the terpolymer are better than that of PS-*co*-PLiMAn, the discrimination characteristics are diminished. By considering that the value of $\varepsilon_{int,n>MLLD}$ is 1.14×10^{-3} for this material, scaling up to fit inside the RPM8 SAIC footprint will satisfy the quantitative RPM requirements by implementing a multilayer format.[101]

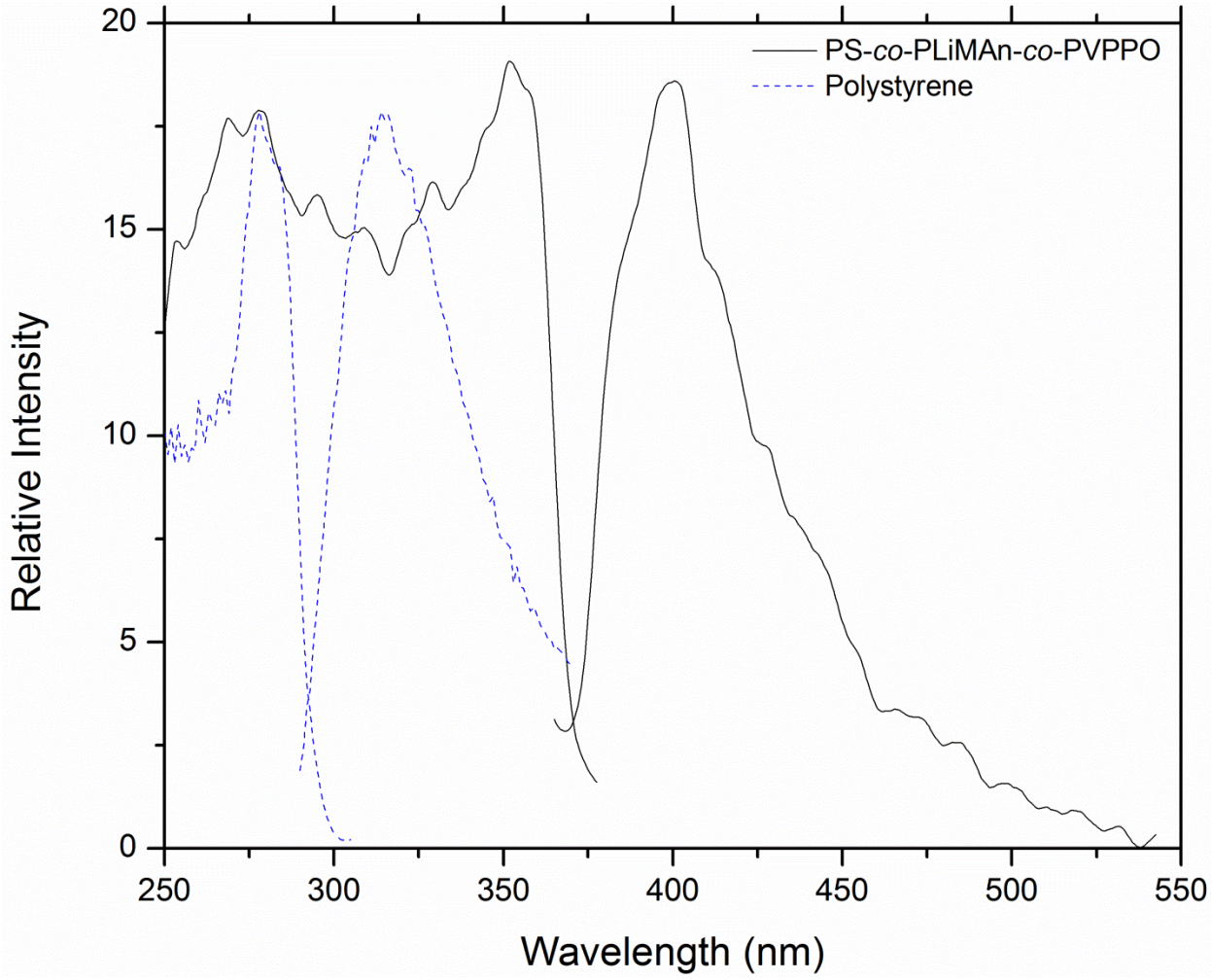


Figure 40. Photoluminescence Spectra of PS and PS-*co*-PLiMAn-*co*-PVPPO.

The PS spectra are shown to illustrate that excitation of the styrene subunits in the terpolymer result in emission from VPPO.

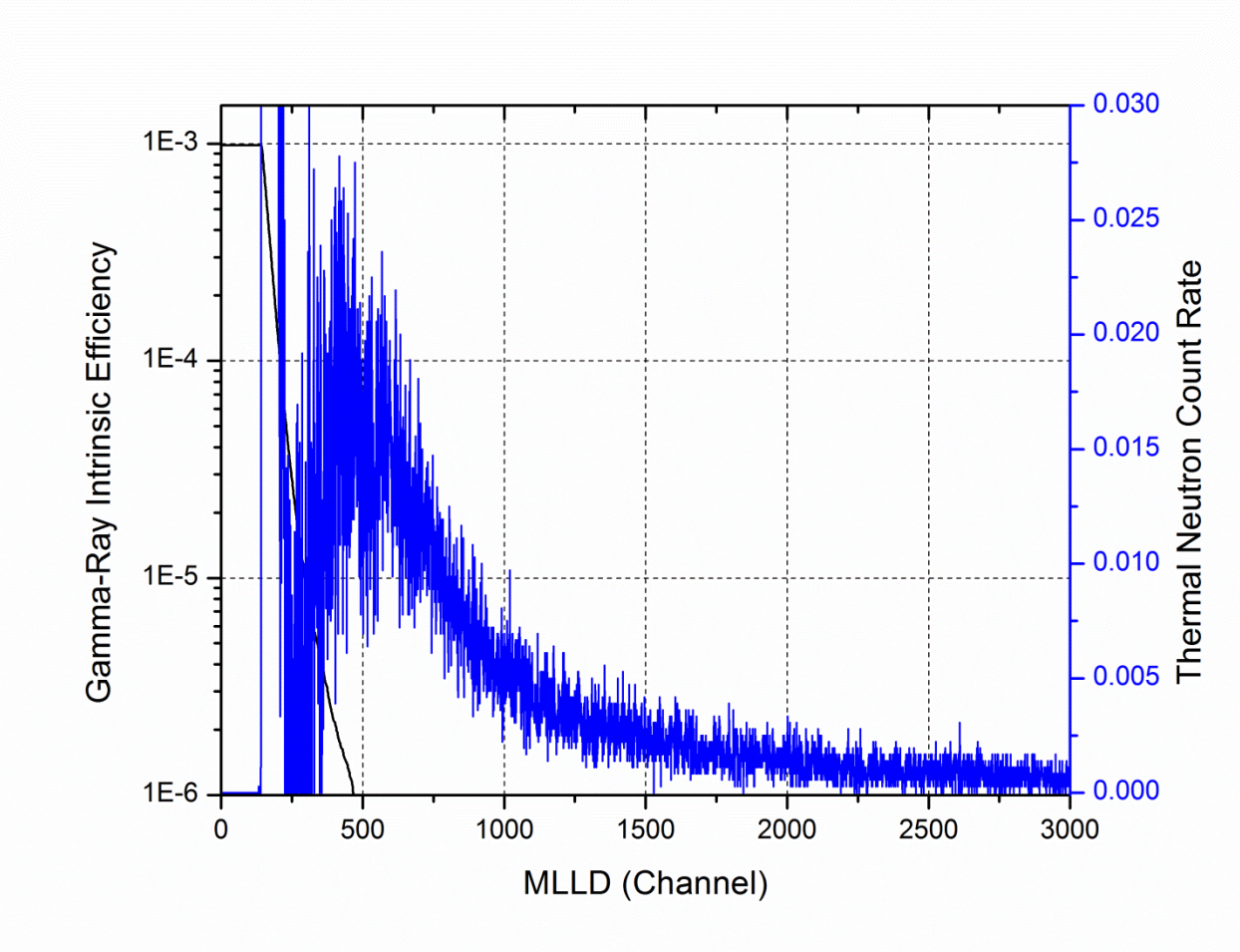


Figure 41. Gamma-Ray Intrinsic Efficiency and Thermal Neutron Count Rate versus MLLD of PS-*co*-PLiMAn-*co*-PVPPO.

Table 21. Light Yields and Neutron/Gamma-Ray Discrimination of Films Based on PS, PS-*co*-PLiMAn, and PS-*co*-PLiMAn-*co*-PVPPO

Polymer	PS	PS-*co*-PLiMAn	PS-*co*-PLiMAn-*co*-PVPPO
wt% ^{6}Li	2.41% ^{6}LiF	3.91% ^{6}Li	2.96% ^{6}Li
Fluor(s), wt%	PPO/POPOP, 5.0%	HSal, 11.6%	VPPO, 7.72%
Thickness	50 μm	183 μm	50 μm
^{241}Am LY	5637	373	242
^{36}Cl LY	2310	139	144
Pb LY	647	115	275
Pb – Cd LY	1864	250	235
^{60}Co LY	312	165	124
$\varepsilon_{int\ n,th}$**	0.03%	0.04%	0.05%
$\varepsilon_{int\ n>MLLD}$†	7.13×10^{-4}	9.32×10^{-4}	1.14×10^{-3}
MLLD	1894	466	469
$CR_{n,th>MLLD}$	7.77 cps	10.8 cps	10.8 cps
$CR_{n>MLLD}$†	8.34 cps	10.9 cps	10.8 cps
$\varepsilon_{abs\ n}$†	1.40×10^{-5}	2.10×10^{-5}	2.28×10^{-5}
$<LY_{n>MLLD}>$†	2358	295	276

Light yields are listed as photons per particle and were calculated from spectral averages based on GS20 emitting 6,250 photons/neutron.

**Intrinsic thermal neutron detection efficiency for all thermal neutron pulses.

†Listed values are for responses in the Pb tube, 67.6% of which have energies below 1 eV.

5.7. Poly(styrene-*co*-lithium 4-vinylbenzoate)

5.7.1. Synthesis and Chemical Characterizations

It was suspected that the low light yields of PS-*co*-PLiMAn + 11.6% HSal and PS-*co*-PLiMAn-*co*-PVPPO was due to the lack of long blocks of consecutive aromatic groups. In aryl vinyl polymers excitation energy migrates through the aromatic pendant groups across a polymer chain until it reaches an adequate proximity to a fluor molecule, at which point the excitation is nonradiatively transferred from the polymer to the fluor. It was thus thought to synthesize a transparent lithium-containing polymer scintillator with long consecutive blocks of aromatic groups. The polymer selected was PS-*co*-PLi4VB. The protocol used to synthesize PS-*co*-PLi4VB was described in section 4.4.3. and in this section the polymer is discussed in greater detail. Several different opinions regarding the best method by which 4VBA should be purified have been reported. The melting point of the as-received material was 138°C (lit. 144°C), which was attributed to the presence of inhibitors and possible impurities. After several attempts, it was determined that the best purification protocol was recrystallization from water.

Synthesis of Li4VB from 4VBA proceeded by direct titration of 4VBA with LiOH. The initial mass of the round bottom flask was measured, then the titrated solution was rotavapped at 35°C until the mass of material inside the flask reduced to that of the expected value for Li4VB which indicated that nearly all the water was removed. Li4VB is not expected to undergo bulk self-initiated thermal polymerization even at temperatures beyond the boiling point of water;[125] however, this low temperature was implemented in order to impose a slightly elevated temperature in the solvent relative to that of the condenser and to reduce the occurrence of side reactions such as oxidation.

The solubility of Li4VB in a variety of organic solvents was investigated to determine the solvents that could be used for solution polymerization. It was determined that Li4VB was soluble only in methanol, ethanol, DMF, and DMSO. Interestingly, the material was insoluble in water even though it remained in solution during the titration procedure. The material was insoluble in isopropanol and *n*-propanol; however, addition of a few drops of water to these solutions mixtures resulted in complete dissolution of the monomer. Also, the monomer did not precipitate when solutions were added to nonsolvents, even at volume ratios of 1:20 of solvent to nonsolvent. Methanol, ethanol, and solutions containing water are not ideal for conducting free radical solution polymerization. DMSO has a higher boiling point than DMF, making it more difficult to remove. Thus, DMF was selected as the polymerization solvent.

In a flame-dried round bottom flask, appropriate masses of Li4VB, styrene, and AIBN were dissolved in DMF, then the flask was sealed with a rubber stopper. The solution was degassed by three freeze-pump-thaw cycles, refilled to ambient pressure with argon, then the flask was suspended in an oil bath at 80°C to polymerize. After 8 hours, the precipitated product was collected. The resulting polymer was insoluble in all solvents and solvent mixtures investigated and was thus considered not usable for this application.

Chapter 6: Conclusions and Future Work

6.1. Summary and Important Conclusions

The work described in this dissertation involved the syntheses and characterizations of four main types lithium-containing polymer films: PS containing ^{6}LiF and PPO/POPOP, PS-*co*-PLiMAn containing HSal, PS-*co*-PLiMAn-*co*-PVPPO, and PS-*co*-PLi4VB. The PS-based composites were previously known in the neutron detection community but the remaining three polymers were previously unreported in the literature. A protocol for fabricating scintillator films that was previously unreported for polymer scintillators was devised, optimized, and implemented. Film fabrication was accomplished by solution casting methods onto 50.8 mm diameter UVT acrylic disks. A variety of chemical and physical characterizations as well as optical and scintillation characterizations were performed to guide the development of optimized compositions of each type of polymer film. The scintillation performances of optimized compositions of each type of polymer film were calibrated using GS20 lithium glass and

evaluated against neutron detection and neutron/gamma-ray discrimination criteria, though our neutron characterization facility contains additional moderation relative to that set forth for quantitative evaluation of detectors for RPM applications. A summary of chemical, physical, and scintillation data for noteworthy materials investigated in this work is shown in Table 21.

The first polymer evaluated was PS synthesized by bulk free-radical polymerization. The quantum yield for fluorescence emission was optimized by varying the concentration of PPO/POPOP and measuring the resulting photoluminescence and scintillation responses, both of which indicated that the optimum concentration of PPO/POPOP was 5.0%. Films of varying thicknesses containing 10% ^{6}LiF and 5% PPO/POPOP were fabricated and tested against the detection and discrimination criteria. In light of the criteria, the best performing film in was 50 μm thick which at the threshold for gamma-ray intrinsic efficiency of $\varepsilon_{int,\gamma} = 10^{-6}$ the neutron count rate was $CR_{n>MLLD} = 8.34$ cps, corresponding to $\varepsilon_{abs\ n} = 1.40 \times 10^{-5}$ in the Pb tube in our characterization facility (67.6% of the neutrons have energies below 1 eV). The value of $\varepsilon_{int,n>MLLD}$ is 7.13×10^{-4}, indicating that in the RPM8 SAIC footprint this material can be made to satisfy the quantitative criteria by implementing a multilayer format.

The second polymer evaluated was PS-*co*-PLiMAn containing HSal. This polymer was synthesized by solution free-radical polymerization of styrene and maleic anhydride to form an alternating copolymer, then the maleic anhydride groups were hydrolyzed and the corresponding acid groups were titrated with LiOH. The polymer formed transparent films for up to 82.5% titration of the acid groups. This polymer was insoluble in organic solvents but was soluble in water, so water-soluble HSal was implemented as the fluor. The resulting film was transparent and p-XRD experiments indicate that it is amorphous. The quantum yield for fluorescence emission from the fluor was optimized by varying the concentration of HSal and it was

determined that the optimum mass fraction was 11.6%, resulting in a total ^{6}Li concentration of 3.91 wt%. Due to acid/base equilibrium between the maleic acid and the HSal, the HSal is converted to LiSal. Both photoluminescence and thermogravimetric analysis indicated the presence of LiSal rather than HSal in the film. This material is thermally stable up to approximately 260°C. At a gamma-ray intrinsic efficiency of $\varepsilon_{int,\gamma} = 10^{-6}$, the neutron count rate was $CR_{n>MLLD}$ = 10.9 cps, corresponding to $\varepsilon_{abs\ n} = 2.10 \times 10^{-5}$ in the Pb tube in our characterization facility. The value of $\varepsilon_{int,n>MLLD}$ is 9.32×10^{-4}, indicating that in the RPM8 SAIC footprint this material can be made to satisfy the quantitative criteria by implementing a multilayer format.

The third polymer evaluated was PS-*co*-PLiMAn-*co*-PVPPO. This polymer was synthesized by solution free-radical polymerization of styrene, MAn, and VPPO. The composition by mass was estimated from elemental analysis to be 60.64% styrene, 31.64% MAn, and 7.72% VPPO. The MAn groups were hydrolyzed and the resulting acid groups were titrated with LiOH. Photoluminescence experiments indicated that the amount of VPPO in the polymer was to collect excitations from styrene such that emission from styrene was negligible. At a gamma-ray intrinsic efficiency of $\varepsilon_{int,\gamma} = 10^{-6}$, the neutron count rate was $CR_{n>MLLD}$ = 10.8 cps, corresponding to $\varepsilon_{abs\ n} = 2.28 \times 10^{-5}$ in the Pb tube in our characterization facility. The value of $\varepsilon_{int,n>MLLD}$ is 1.14×10^{-3}, indicating that in the RPM8 SAIC footprint this material can be made to satisfy the quantitative criteria by implementing a multilayer format.

The final polymer evaluated was PS-*co*-PLi4VB. This polymer was synthesized by solution free-radical polymerization of styrene and Li4VB. This polymer was insoluble in all organic solvents and solvent mixtures investigated and was thus not considered useful for this application.

6.2. Recommendations for Future Work

None of the investigated polymers in the format of a single film layer 2 inches in diameter simultaneously satisfied both the neutron detection and neutron/gamma-ray discrimination criteria set forth for radiation portal monitors, even with the 2.5 cm of additional moderation present in our neutron characterization facility relative to that proscribed for evaluation of radiation portal monitors. It was necessary to use a layered format for the films in order to meet the detection criteria. Using the pulse-height discrimination techniques described herein, it appears that if the light yield for neutrons relative to photons of any of the polymers was improved by a factor of 2 then it would be possible for the material to meet the detection criteria for a full-scale detector. A significant problem for large-scale scintillation detectors is efficiently collecting and transporting scintillation light from the scintillator to the light collection device. For polymer composites, suboptimal optical transmission makes this problem worse. A simple, robust, repeatable strategy by which transparent lithium-containing polymer scintillators can be synthesized was devised during the course of the work described herein which reduces the magnitude of the problem associated with light collection from lithium-containing polymer composite scintillators. This strategy of providing bonds between the lithium and the polymer was successfully implemented in two representative cases and it is expected that many other modifications are possible, some of which could possibly result in materials with improved light yields. In particular, it is suspected that implementing an aromatic monomer that has a reduced probability of losing electronic excitation energy by vibrations as compared to styrene, such as vinyl derivatives of toluene, xylene, pseudocumene, naphthalene, or anthracene, would result in an increase in light yield. It is also suspected that further investigations of the effects of disrupting the continuity in the aromatic pendant groups by copolymerization of

nonaromatic monomers such as maleic anhydride on the light yield could provide some insight as to which polymer structures to avoid and which to pursue for the development of transparent lithium-containing scintillators. It is my opinion that the investigation of aryl vinyl polymers with backbone-grafted lithium-complexing functional groups would not be subject to interference of energy migration and would result in higher light yields.

Other future work should involve the investigation of different film geometries. Some preliminary investigations by myself and coworkers have indicated that as compared to a single film, stacking a series of thin films with each separated by nonscintillating regions of sufficient thicknesses results in an increase in the neutron count rate above the MLLD whereas the gamma-ray intrinsic efficiency remains largely unaffected. At this time, this phenomenon and its exploitation is still being investigated by our group. The technical details, experimentation, simulations, and data analysis required for a proper discussion of this project constitute the bulk of an entirely separate dissertation and were considered outside the scope of a dissertation submitted for a chemistry degree and only relevant conclusions have been given here with proper referencing.

As stated in section 3.4.3., an accurate theory permitting the quantitative prediction of light yields in organic scintillators from first principles has yet to be developed. The author spent some time investigating this issue in light of the theories of Birks, Sangster, and Gunder. Birks' quantitative theories rely on fitting equations from empirical data and do not incorporate information regarding molecular structure. Sangster provided only qualitative descriptions. Gunder's theory relies on the variation in electron density on the elementary chain to describe scintillation light yields and fails for some of the polymers investigated by our group such as poly(2,4,6-trimethylstyrene-*co*-2,3,4,5,6-pentafluorostyrene) and poly(2-vinyl naphthalene).

Preliminary *ab initio* calculations implementing 6-31G* basis sets using HyperChem v7.5 demonstrated that there is a single-exponential positive correlation between electronic polarizability and scintillation efficiency that satisfactorily describes polymers studied by Gunder as well as those studied in our group. Preliminary data supporting this idea was presented by the author to the radiation detection community where it was well-received and unchallenged.[126] To date, no information in the literature relating electronic polarizability to either energy deposition by ionizing radiation or scintillation efficiency was located. Due to limitations in my knowledge of computational chemistry, this idea was not thoroughly investigated. It is thus my opinion that future research on the quantitative relationship of between molecular structure with scintillation efficiency in organic scintillators include electronic polarizability.

List of References

(1) Chadwick, J. *Nature* **1932**, *129*, 312.

(2) Kouzes, R. T. *The ^{3}He Supply Problem*, Pacific Northwest National Laboratory Report PNNL-18388, 2009.

(3) Pantaleo, J. Supply and demand of helium-3 (3He), the need for 3He in the United States is outpacing production. http://www.ornl.gov/sci/isotopes/he3_fact_sheet.pdf (accessed October 18, 2011).

(4) Hall, H. Keynote Speech, Second Annual James E. Turner Symposium, Oak Ridge, TN, May 22-23, 2013.

(5) United States Government Accountability Office. *Combating Nuclear Smuggling: DHS's Cost-Benefit Analysis to Support the Purchase of New Radiation Detection Portal Monitors Was Not Based on Available Performance Data and Did Not Fully Evaluate All the Monitors' Costs and Benefits*, GAO-07-113R, October 17, 2006.

(6) Bondarenko, L. N.; Kurguzov, V. V.; Prokof'ev, Y. A.; Rogov, E. V.; Spivak, P. E. *Pis'ma Zh. Eksp. Teor. Fiz.* **1978**, *28*, 328.

(7) Kouzes, R. T.; Ely, J. R.; Lintereur, A. T.; Stephens, D. L. *Neutron Detector Gamma Insensitivity Criteria*, Pacific Northwest National Laboratory Report PNNL-18903, 2009.

(8) ANSI. *American National Standard for Evaluation and Performance of Radiation Detection Portal Monitors for Use in Homeland Security*, Technical Report. ANSI 42.35, American Nuclear Standards Institute, Washington, DC, 2004.

(9) Anderson, D. W. *Absorption of Ionizing Radiation*; University Park Press: Baltimore, 1984.

(10) Turner, J. E. *Atoms, Radiation, and Radiation Protection*; 3rd ed.; Wiley-VHC: Darmstadt, 2007.

(11) Knoll, G. F. *Radiation Detection and Measurement*; 4th ed.; John Wiley & Sons, Inc.: New York, 2010.

(12) Loveland, W.; Morrissey, D. J.; Seaborg, G. T. *Modern Nuclear Chemistry*; John Wiley & Sons, Inc.: Hoboken, 2006.

(13) Sabin, J. R.; Oddershede, J. *Nucl. Instrum. Meth.* **1987**, *B27*, 280.

(14) Evans, R. D. *The Atomic Nucleus*; McGraw-Hill, Inc.: New York, 1955.

(15) Bell, Z. W.; Boatner, L. A. *IEEE Trans. Nucl. Sci.* **2010**, *57*, 3800.

(16) Sears, V. F. *Neutron News* **1992**, *3*, 29.

(17) Bäcklin, A.; Holmberg, N. E.; Bäckström, G. *Nucl. Phys.* **1966**, *80*, 154.

(18) Sakurai, Y.; Tanaka, H.; Suzuki, M.; Kashino, G.; Kinashi, Y.; Masunaga, S.; Ono, K.; Maruhashi, A. *IFMBE Proc.* **2009**, *25*, 470.

(19) Allen, W. D. *Neutron Detection*; George Newnes, Ltd.: London, 1960.

(20) Price, W. J. *Nuclear Radiation Detection*; 2nd ed.; McGraw-Hill: New York, 1964.

(21) Grosshoeg, G. *Neutron Ionization Chambers* North Holland, Amsterdam, 1979.

(22) van Ginhoven, R. M.; Kouzes, R. T.; Stephens, D. L. *Alternative Neutron Detector Technologies for Homeland Security*, Pacific Northwest National Laboratory Report PNNL-18471, 2009.

(23) Lintereur, A. T.; Kouzes, R. T.; Ely, J. H.; Erikson, L. E.; Siciliano, E. R. *Boron-Lined Neutron Detector Measurements*, Pacific Northwest National Laboratory Report PNNL-18938, 2009.

(24) Kouzes, R. T.; Ely, J. H.; Erikson, L. E.; Kernan, W. J.; Stromswold, D. C.; Woodring, M. L. *Full Scale Coated Fiber Neutron Detector Measurements*, Pacific Northwest National Laboratory Report PNNL-19264, 2010.

(25) Kouzes, R. T.; Ely, J. H.; Erikson, L. E.; Kernan, W. J.; Lintereur, A. T.; Siciliano, E. R.; Stromswold, D. C.; Woodring, M. L. *Alternative Neutron Detection Testing Summary*, Pacific Northwest National Laboratory Report PNNL-19311, 2010.

(26) Kouzes, R. T.; Ely, J. H. *Status Summary of 3He and Neutron Detection Alternatives for Homeland Security*, Pacific Northwest National Laboratory Report PNNL-19360, 2010.

(27) Kouzes, R. T.; Ely, J. H.; Stromswold, D. C. *Boron-Lined Straw-Tube Neutron Detector Test*, Pacific Northwest National Laboratory Report PNNL-19600, 2010.

(28) Kouzes, R. T.; Ely, J. H. *Lithium and Zinc Sulfide Coated Plastic Neutron Detector Test*, Pacific Northwest National Laboratory Report PNNL-19566, 2010.

(29) Nelson, K. A.; Bellinger, S. L.; Montag, B. W.; Neihart, J. L.; Riedel, T. A.; Schmidt, A. J.; McGregor, D. S. *Nucl. Instrum. Meth. A* **2012**, *669*, 79.

(30) Nicholson, K. P.; Snelling, G. F. *B. J. Appl. Phys.* **1955**, *6*, 104.

(31) Derenzo, S.; Boswell, M.; Weber, M.; Brennan, K.; http://scintillator.lbl.gov: Lawrence Berkeley National Laboratory (accessed February 2013).

(32) Czirr, J. B.; MacGillivray, G. M.; MacGillivray, R. R.; Seddon, P. J. *Nucl. Instrum. Meth. A* **1999**, *424*, 15.

(33) Koschan, M.; Green, A.; Zhuravleva, M.; Melcher, C. In *ICCG-16* Beijing, China, 2010.

(34) Glodo, J.; Brys, W.; Entine, G.; Higgins, W. M.; Loef, E. v.; Squillante, M. R.; Shah, K. S. In *IEEE Nuclear Science Symposium* Honolulu, HI, 2007.

(35) Glodo, J.; Lingertat, H.; Brecher, C.; Shah, K. S.; Lempicki, A. In *IEEE Nuclear Science Symposium* Wyndham El Conquistador, Puerto Rico, 2005.

(36) Zaitseva, N.; Newby, J.; Hull, G.; Saw, C.; Carman, L.; Cherepy, N.; Payne, S. *Cryst. Growth Des.* **2009**, *9*, 3799.

(37) Spowart, A. R. *Nucl. Instrum. Meth.* **1976**, *135*, 441.

(38) Smith, M. B.; Achtzehn, T.; Andrews, H. R.; Clifford, E.; Ing, H.; Kovaltchouk, V. D. *IEEE Trans. Nucl. Sci.* **2013**, *60*, 855.

(39) Howell, S. C., Brigham Young University, *Lithium Gadolinium Borate Crystal Scintillator for Low Flux Neutron Detection*, B.S. Thesis, 2009.

(40) Trojan-Piegza, J.; Glodo, J.; Sarin, V. K. *Radiat. Meas.* **2010**, *48*, 163.

(41) Berlman, I. B. *Handbook of Fluorescence Spectra of Aromatic Molecules*; 2nd ed.; Academic Press: New York, 1971.

(42) Dawson, W. R.; Windsor, M. W. *J. Phys. Chem.* **1968**, *72*, 3251.

(43) Im, H.; Saengkerdsub, S.; Stephan, A. C.; Pawel, M. D.; Holcomb, D. E.; Dai, S. *Adv. Mater.* **2004**, *16*, 1757.

(44) Kesanli, B.; Hong, K.; Meyer, K.; Im, H.; Dai, S. *Appl. Phys. Lett.* **2006**, *89*, 214104.

(45) Quaranta, A.; Carturan, S. M.; Marchi, T.; Kravchuk, V. L.; Gramegna, F.; Maggioni, G.; Degerlier, M. *IEEE Trans. Nucl. Sci.* **2010**, *57*, 891.

(46) Swank, R. K.; Buck, W. L. *Phys. Rev.* **1953**, *91*, 927.

(47) Koski, W. S. *Phys. Rev.* **1950**, *82*, 230.

(48) Skoog, D. A.; Holler, F. J.; Nieman, T. A. *Principles of Instrumental Analysis*; 5th ed.; Brooks Cole, 1998.

(49) Klan, P.; Wirz, J. *Photochemistry of organic compounds: From concenpts to practice*; John Wiley & Sons Ltd.: West Sussex, 2009.

(50) Palszegi, T.; Rychly, J.; Melus, M. *Chem. Phys.* **1994**, *186*, 41.

(51) Semerak, S. N.; Frank, C. W. *Photophysics of Excimer Formation in Aryl Vinyl Polymers*; Springer-Verlag Berlin Heidelberg, 1983.

(52) Holden, D. A.; Guillet, J. E. *Macromolecules* **1982**, *15*, 1475.

(53) Bai, F.; Chang, C. H.; Webber, S. E. *Macromolecules* **1986**, *19*, 588.

(54) Bai, F.; Chang, C. H.; Webber, S. E. *Macromolecules* **1986**, *19*, 2484.

(55) Hargreaves, J. S.; Webber, S. E. *Macromolecules* **1982**, *15*, 424.

(56) Kim, N.; Webber, S. E. *Macromolecules* **1982**, *15*, 430.

(57) Hargreaves, J. S.; Webber, S. E. *Macromolecules* **1984**, *17*, 235.

(58) MacCallum, J. R. *Eur. Polym. J.* **1980**, *17*, 209.

(59) McInally, I.; Reid, R. F.; Rutherford, H.; Soutar, I. *Eur. Polym. J.* **1979**, *15*, 723.

(60) Förster, T. *Ann. Phys.* **1948**, *437*, 55.

(61) Skarstad, P.; Ma, R.; Lipsky, S. *Mol. Cryst.* **1968**, *4*, 3.

(62) Cooper, R.; Thomas, J. K. *J. Chem. Phys.* **1968**, *48*, 5097.

(63) *Luminescence*; Ronda, C., Ed.; Wiley-VHC: Weinheim, 2008.

(64) Platzman, R. L. *Radiation Research*; North Holland Publishing Company: Amsterdam, 1967.

(65) Horrocks, D. L. *J. Chem. Phys.* **1970**, *52*, 1566.

(66) Skerbele, A.; Lassettre, E. N. *J. Chem. Phys.* **1965**, *42*, 395.

(67) Swank, R. K. *Annu. Rev. Nucl. Sci.* **1954**, *4*, 111.

(68) Birks, J. B.; Kuchela, K. N. *Discuss. Faraday Soc.* **1959**, *27*, 57.

(69) Neilson, R. D. M.; Soutar, I.; Steedman, W. *J. Polym. Sci. A1* **1976**, *14*, 1005.

(70) Neilson, R. D. M.; Soutar, I.; Steedman, W. *J. Polym. Sci. A2* **1977**, *15*, 617.

(71) Hallam, A.; Birks, J. B. *J. Phys. B - At. Mol. Opt.* **1978**, *11*, 3273.

(72) Phillips, D.; Roberts, A. J.; Soutar, I. *Macromolecules* **1983**, *16*, 1593.

(73) Inagaki, T.; Takashima, R. *Nucl. Instrum. Meth.* **1982**, *201*, 511.

(74) Salimgareeva, V. N.; Kolesov, S. V. *Instrum. Exp. Tech+* **2005**, *48*, 5.

(75) Salimgareeva, V. N.; Kolesov, S. V. *Instrum. Exp. Tech.+* **2006**, *48*, 273.

(76) Aldongarov, A. A.; Barashkov, N. N.; Irgibaeva, I. S.; Khakhel, O. A.; Sakhno, Y. E. *Functional Mater.* **2008**, *15*, 398.

(77) Grigor'eva, V. I.; Gunder, O. A.; Krasovitskii, B. M.; Petrova, I. B. *J. Appl. Spec.+* **1968**, *8*, 884.

(78) Gunder, O. A.; Voronkina, N. I.; Kopina, I. V. *IEEE Trans. Nucl. Sci.* **1995**, *42*, 320.

(79) Sangster, R. C.; Irvine, J. W. *J. Chem. Phys.* **1956**, *24*, 670.

(80) Birks, J. B. *The Theory and Practice of Scintillation Counting*; Pergamon Press: Oxford, 1964.

(81) Hiemenz, P. C.; Lodge, T. P. *Polymer Chemistry*; 2nd ed.; CRC Press: Boca Raton, 2007.

(82) Atkins, P.; Paula, J. d. *Physical Chemistry*; 8th ed.; W. H. Freeman and Company: New York, 2006.

(83) Chang, Z., Carborane-loaded polymer scintillators for thermal neutron detection.

(84) Sen, I.; Penumadu, D.; Williamson, M.; Miller, L. F.; Green, A. D.; Mabe, A. N. *IEEE Trans. Nucl. Sci.* **2011**, *58*, 1386.

(85) Sen, I.; Mabe, A. N.; Green, A.; Penumadu, D.; Schweitzer, G.; Thomas, K.; Miller, L. In *IEEE Nuclear Science Symposium* Knoxville, TN, November 2010.

(86) Ovechkina, L.; Riley, K.; Miller, S.; Bell, Z.; Nagarkar, V. *Phys. Proc. 2* **2009**, *2*, 161.

(87) Sen, I.; Urffer, M.; Penumadu, D.; Young, S. A.; Miller, L. F.; Mabe, A. N. *IEEE Trans. Nucl. Sci.* **2012**, *59*, 1781.

(88) Young, S. A.; Sen, I.; Penumadu, D. *J. Eng. Mater. T.* **2012**, *134*, 010908.

(89) Khosravi, J., McGill University, *Production of Lithium Peroxide and Lithium Oxide in an Alcohol Medium*, Ph.D. Thesis, 2007.

(90) Personal communication with Dr. Jimmy Mays, University of Tennessee.

(91) Personal communication with Dr. Larry Miller, University of Tennessee.

(92) Henry, S. M.; El-Sayed, M. E. H.; Pirie, C. M.; Hoffman, A. S.; Stayton, P. S. *Biomacromolecules* **2006**, *7*, 2407.

(93) Baruah, S. D.; Laskar, N. C. *J. Appl. Polym. Sci.* **1996**, *60*, 649.

(94) Mabe, A. N.; Auxier II, J. D.; Urffer, M. J.; Penumadu, D.; Schweitzer, G. K.; Miller, L. F. *Nucl. Instrum. Meth. A* **2013**, *722*, 29.

(95) Kysela, G.; Staudner, E.; Slyskova, E.; Zemlicka, A. *Makromol. Chem., Rapid Communications* **1992**, *13*, 261.

(96) Chitanu, G. C.; Popescu, I.; Carpov, A. *Rev. Roum. Chim.* **2007**, *52*, 135.

(97) McInally, I.; Soutar, I.; Steedman, W. *J. Polym. Sci.* **1977**, *15*, 2511.

(98) Frangopol, P. T.; Balaban, A. T.; Barladeanu, L.; Cioranescu, E. *Tetrahedron* **1961**, *16*, 59.

(99) Lhoták, P.; Kurfürst, A. *Collect. Czech. Chem. Commun.* **1993**, *58*, 2720.

(100) Drefahl, V. G.; Winnefeld, K. *J. Prakt. Chem.* **1965**, *29*, 72.

(101) Personal Communication with Matthew Urffer, University of Tennessee.

(102) Urffer, M. J., University of Tennessee, *Design of a Neutron Detector Capable of Replacing He-3 Detectors Utilizing Thin Polymeric Films*, Master's Thesis, University of Tennessee, 2012.

(103) Oshima, Y.; Yasumune, T.; Masuda, T.; Maehata, K.; Ishibashi, K.; Umeno, T. *Prog. Nucl. Sci. Tech.* **2011**, *1*, 296.

(104) Khabaz, R. *Ann. Nucl. Energy* **2012**, *46*, 76.

(105) Valentine, T. E. *Ann. Nucl. Energy* **2001**, *28*, 191.

(106) Hubbell, J. H.; Seltzer, S. M.; National Institute of Standards and Technology: Gaithersburg, MD, 2004.

(107) Ziegler, J. F.; Ziegler, M. D.; Biersack, J. P. *SRIM-2011.08, Stopping and Range of Ions in Matter*, Pergamon, New York, 2011.

(108) Personal communication with Dr. Indraneel Sen, University of Tennessee.

(109) Mabe, A. N.; Auxier II, J. D.; Urffer, M. J.; Young, S. A.; Penumadu, D.; Schweitzer, G. K.; Miller, L. F. *J. Compos.* **2013**, *2013*, Article ID: 539060, 8 pages.

(110) Simons, J. K.; Chen, J. M.; Taylor, J. W.; Rosenberg, R. A. *Macromolecules* **1993**, *26*, 3262.

(111) Leibowitz, M.; Weinreb, A. *J. Chem. Phys.* **1967**, *46*, 4652.

(112) Du, H.; Ruh, R. A.; Li, J.; Corkan, A.; Lindsey, J. S. *PhotochemCAD: A computer-aided design and research tool in photochemistry*, Photochem. Photobiol., 68, 141., 1998.

(113) Mathad, R. D.; Kumar, H. G. H.; Sannakki, B.; Ganesh, S.; Sarma, K. S. S.; Badiger, M. V. *Radiat. Eff. Defects in S.* **2009**, *164*, 656.

(114) Spirin, Y. L.; Yatsimirskaya, T. S. *Polymer Science U.S.S.R.* **1976**, *18*, 857.

(115) Kumari, S.; Nigam, D.; Agarwal, D.; Nigam, I. *J. Appl. Polym. Sci.* **2007**, *103*, 3194.

(116) Zeng, W.; Shirota, Y. *Macromolecules* **1989**, *22*, 4204.

(117) Tiefenthal, H. E.; Pitcairn; Lee, Y. C. United States Patent Office, United States, 1962, p 7.

(118) Morawetz, H.; Kotliar, A. M.; Mark, H. *J. Phys. Chem.* **1954**, *58*, 619.

(119) Dai, X.; Rollin, E.; Bellerive, A.; Hargrove, C.; Sinclair, D.; Mifflin, C.; Zhang, F. *Nucl. Instrum. Meth. A* **2008**, *589*, 290.

(120) Gebicki, J.; Reimschussel, W.; Rudzinski, J. *Int. J. Appl. Radiat. Isot.* **1984**, *35*, 1133.

(121) Kumar, V.; Datta, A. K. *Appl. Opt.* **1979**, *18*, 1414.

(122) Pozdnyakov, I. P.; Pigliucci, A.; Tkachenko, N.; Plyusnin, V. F.; Vauthey, E.; Lemmetyinen, H. *J. Phys. Org. Chem.* **2008**, *22*, 449.

(123) Jarm, V.; Bogdanic, G. *Thermochim. Acta* **1990**, *171*, 39.

(124) Zaitseva, N.; Newby, J.; Hull, G.; Saw, C.; Carman, L.; Cherpy, N.; Payne, S. *Growth and Properties of Lithium Salicylate Single Crystals*, Lawrence Livermore National Laboratory, LLNL-JRNL-410824, 2009.

(125) Inoki, M.; Akutsu, F.; Kitayama, Y.; Kasashima, Y.; Naruchi, K. *Macromol. Chem. Physic.* **1998**, *199*, 619.

(126) Mabe, A. N. Academic Research Initiative 5th Annual Grantee's Conference. Leesburg, VA, July 23, 2012.

Vita

Andrew Mabe was born in Memphis, Tennessee on November 5, 1987. He grew up and attended school in Camden, Tennessee, then moved to Memphis, Tennessee during high school where he graduated from Bolton High School in Arlington, Tennessee in 2006. He then attended the University of Tennessee at Knoxville and received his Bachelor of Science in Chemistry degree in 2010. After completing his bachelor's degree, he accepted a graduate research assistant position at the University of Tennessee at Knoxville in the laboratory of Dr. George Schweitzer to conduct research in the design, synthesis, and fabrication of polymer scintillators for the detection of slow neutrons. He completed his Ph.D. in polymer chemistry in August 2013. During his residency as a graduate student, he married Rose Johnson and on September 2, 2011 his daughter Alina Mabe-Johnson was born.